

AD-A121 889

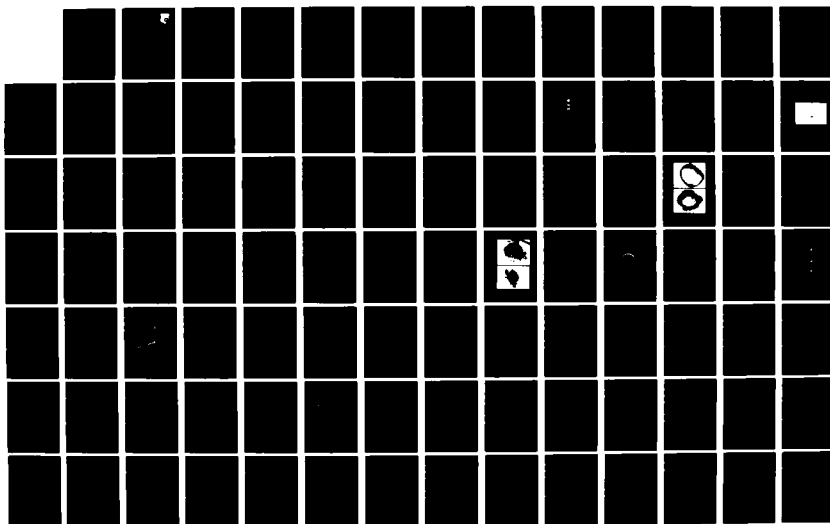
COMBUSTION OF AGGLOMERATES FORMED BY CARBON SLURRY  
FUELS(U) PENNSYLVANIA STATE UNIV UNIVERSITY PARK DEPT  
OF MECHANICAL EN. G A SZEKELY ET AL. SEP 82  
AFWAL-TR-82-2085 F33615-81-K-2039

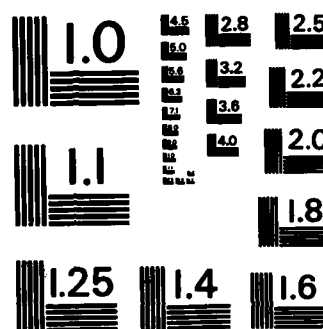
1/2

UNCLASSIFIED

F/G 21/2.

NL

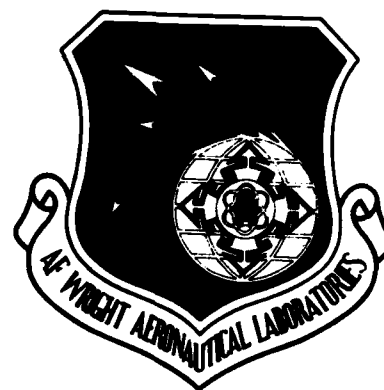




MICROCOPY RESOLUTION TEST CHART  
NATIONAL BUREAU OF STANDARDS-1963-A

12

AFWAL-TR-82-2085



COMBUSTION OF AGGLOMERATES FORMED BY CARBON SLURRY FUELS

G. A. Szekely, Jr. and G. M. Faeth

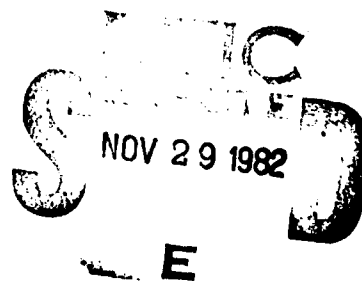
The Pennsylvania State University  
Department of Mechanical Engineering  
University Park, PA 16802

September 1982

Final Report for Period July 1981 - June 1982

Approved for public release; distribution unlimited.

AERO PROPULSION LABORATORY  
AIR FORCE WRIGHT AERONAUTICAL LABORATORIES  
AIR FORCE SYSTEMS COMMAND  
WRIGHT-PATTERSON AIR FORCE BASE, OHIO 45433



82 11 29 019

AD A 121889

DTIC FILE COPY

# NOTICE

When Government drawings, specifications, or other data are used for any purpose other than in connection with a definitely related Government procurement operation, the United States Government thereby incurs no responsibility nor any obligation whatsoever; and the fact that the government may have formulated, furnished, or in any way supplied the said drawings, specifications, or other data, is not to be regarded by implication or otherwise as in any manner licensing the holder or any other person or corporation, or conveying any rights or permission to manufacture use, or sell any patented invention that may in any way be related thereto.

This report has been reviewed by the Office of Public Affairs (ASD/PA) and is releaseable to the National Technical Information Service (NTIS). At NTIS, it will be available to the general public, including foreign nations.

This technical report has been reviewed and is approved for publication.

*Charles R. Martel*

CHARLES R. MARTEL  
Technical Area Manager, Fuels Branch  
Fuels and Lubrication Division  
Aero Propulsion Laboratory

*Arthur V. Churchill*

ARTHUR V. CHURCHILL  
Chief, Fuels Branch  
Fuels and Lubrication Division  
Aero Propulsion Laboratory

*Benito P. Botteri*

BENITO P. BOTTERI, Asst Chief  
Fuels and Lubrication Division  
Aero Propulsion Laboratory

"If your address has changed, if you wish to be removed from our mailing list, or if the addressee is no longer employed by your organization please notify AFWAL/POSF, W-PAFB OH 45433 to help us maintain a current mailing list".

Copies of this report should not be returned unless return is required by security considerations, contractual obligations, or notice on a specific document.

REPORT DOCUMENTATION PAGE		READ INSTRUCTIONS BEFORE COMPLETING FORM
1. REPORT NUMBER AFWAL-TR-82-2085	2. GOVT ACCESSION NO. AD-A121 889	3. RECIPIENT'S CATALOG NUMBER
4. TITLE (and Subtitle) Combustion of Agglomerates Formed by Carbon . Slurry Fuels		5. TYPE OF REPORT & PERIOD COVERED Final Report July 1981- June 1982
		6. PERFORMING ORG. REPORT NUMBER
7. AUTHOR(s) G.A. Szekely <sup>5</sup> and G. M. Faeth		8. CONTRACT OR GRANT NUMBER(s) F33615-81-K-2039
9. PERFORMING ORGANIZATION NAME AND ADDRESS The Pennsylvania State University Department of Mechanical Engineering University Park, PA 16802		10. PROGRAM ELEMENT, PROJECT, TASK AREA & WORK UNIT NUMBERS 30480512 62203F
11. CONTROLLING OFFICE NAME AND ADDRESS Aero Propulsion Laboratory (AFWAL/POSF) Air Force Wright Aeronautical Laboratories (AFSC) Wright-Patterson Air Force Base, OH 45433		12. REPORT DATE September 1982
		13. NUMBER OF PAGES 129
14. MONITORING AGENCY NAME & ADDRESS (if different from Controlling Office)		15. SECURITY CLASS. (of this report) Unclassified
		15a. DECLASSIFICATION/DOWNGRADING SCHEDULE
16. DISTRIBUTION STATEMENT (of this Report) Approved for Public Release; Distribution Unlimited		
17. DISTRIBUTION STATEMENT (of the abstract entered in Block 20, if different from Report)		
18. SUPPLEMENTARY NOTES		
19. KEY WORDS (Continue on reverse side if necessary and identify by block number) Carbon Slurry      Slurry Combustion High Density Fuels      Carbon Combustion Slurry Fuels microwater		
20. ABSTRACT (Continue on reverse side if necessary and identify by block number) The reaction of carbon-black agglomerates, formed during the combustion of carbon slurry fuels, is considered. A monodisperse stream of agglomerates (10-75 $\mu$ m initial diameter) was observed in the post-flame region of a flat-flame burner yielding particle size, mass, temperature and velocity as a function of time in the burner gases. Tests considered burner fuel equivalence ratios of 0.2-1.4, and gas temperatures of 1620-1960 K at atmospheric pressure. Several carbon-black formulations were considered: monodisperse blacks having ultimate carbon black particle sizes		

BLOCK 20 - ABSTRACT

of 70, 150 and 300 nm, and a blend involving 50% mass loadings (each) of carbon blacks having ultimate carbon particle sizes of 70 and 300 nm. The measurements were compared with a shrinking sphere model of the process using two alternative reaction mechanisms (carbon reaction with  $O_2^{\cdot}$  and OH or with  $O_2^{\cdot}$ ,  $CO_2^{\cdot}$  and  $H_2O$ ). Empirical transport enhancement and area/reactivity parameters were defined to allow for gas motion and reaction in agglomerate pores. These parameters were determined from the data. Both reaction mechanisms satisfactorily correlated the data using empirical parameters which were relatively independent of ambient conditions, particle size and extent of reaction--aside from an initial transient period where the pore structure of the agglomerate developed. The rate of combustion of monodisperse blacks increased slightly as the ultimate carbon-black particle size was reduced. The burning rate of the carbon-black blend was lower than the other fuels considered during the investigation yielding residence times for reaction 10-50% longer than monodisperse blacks at comparable conditions.

11  
Unclassified

# PREFACE

This research was supported by the Aero Propulsion Laboratory, Wright-Patterson Air Force Base, Ohio, under Contract No. F33615-81-K-2039 (July 6, 1981) entitled "Combustion of Agglomerates of Carbon Slurry Drops." Mr. Charles Martel, Aero Propulsion Laboratory, Air Force Wright Aeronautical Laboratories, served as technical director for the work.

The fuels used in the study were provided by R. S. Stearns and L. W. Hall, Jr., of Suntech Group, Marcus Hook, PA. The authors wish to acknowledge useful discussions with them concerning the properties of carbon-black slurries. We also wish to acknowledge the assistance of S. Riddle during the latter stages of the investigation.

Accession For	
NTIS GRA&I	<input checked="" type="checkbox"/>
DTIC TAB	<input type="checkbox"/>
Unannounced	<input type="checkbox"/>
Justification	
By	
Distribution/	
Availability Codes	
Dist	Avail and/or Special
A	



## TABLE OF CONTENTS

	<u>Page</u>
1. Introduction. . . . .	1
1.1 General Objectives . . . . .	1
1.2 Background . . . . .	2
1.3 Specific Objectives. . . . .	4
2. Experimental Methods. . . . .	5
2.1 Apparatus. . . . .	5
2.2 Particle Environment . . . . .	11
2.2.1 Velocity Measurements . . . . .	11
2.2.2 Temperature Measurements. . . . .	11
2.2.3 Concentration Measurements. . . . .	12
2.3 Particle Measurements. . . . .	13
2.3.1 Velocity Measurements . . . . .	13
2.3.2 Temperature Measurements. . . . .	13
2.3.3 Diameter Measurements . . . . .	13
2.3.4 Mass Measurements . . . . .	16
2.4 Experimental Conditions. . . . .	17
3. Theoretical Methods . . . . .	20
3.1 Description of Model . . . . .	20
3.2 Gas-Phase Transport. . . . .	25
3.3 Surface Reaction Models. . . . .	26
3.4 Particle-Life Histories. . . . .	29
4. Results and Discussion. . . . .	32
4.1 Agglomerates of Monodisperse Carbon-Blacks . . . . .	32
4.1.1 Appearance. . . . .	32
4.1.2 Empirical Parameters. . . . .	32
4.1.3 Burning Rates . . . . .	44
4.1.4 Life Histories. . . . .	51
4.2 Agglomerates of Carbon-Black Blends. . . . .	81
4.2.1 Appearance. . . . .	81
4.2.2 Empirical Parameters. . . . .	83
4.2.3 Life Histories. . . . .	89
5. Conclusions . . . . .	96
Appendix A: Summary of Data	
A.1 Particle Environment . . . . .	99
A.2 Agglomerates of Monodisperse Particles, $d_u = 300$ nm. . .	105
A.3 Agglomerates of Monodisperse Particles, $d_u = 150$ nm. . .	119
A.4 Agglomerates of Monodisperse Particles, $d_u = 70$ nm . . .	122
A.5 Agglomerates of a Particle Blend, $d_u = 70$ and 300 nm (50% each by mass) . . . . .	125
References. . . . .	128



# LIST OF ILLUSTRATIONS

<u>Figure</u>		<u>Page</u>
1	Schematic of the flat-flame-burner apparatus. . . . .	6
2	Time-exposure photograph of particles reacting above the flat-flame burner . . . . .	10
3	Sketch of the quenching probe used for particle collection. . . . .	14
4	SEM photographs of collected particles: $\phi = 1$ , $T_f = 1683$ K, $d_{po} = 73.4$ $\mu$ m. Upper and lower photographs have reacted mass fractions of 0.000 and 0.122, respectively, and $d_u = 300$ nm . . . . .	22
5	Apparent particle density as a function of reacted mass fraction for $d_u = 300$ nm . . . . .	23
6	SEM photographs of collected particles: $\phi = 1$ , $T_f = 1683$ K, $d_{po} = 73.4$ $\mu$ m. Upper and lower photographs have reacted mass fractions of 0.902 and 0.999 and $d_u = 300$ nm . . . . .	33
7	Apparent particle density as a function of reacted mass fraction for various $d_u$ . . . . .	34
8	Transport-enhancement factor as a function of reacted mass fraction for $d_u = 300$ nm . . . . .	35
9	Transport-enhancement factor as a function of reacted mass fraction for various $d_u$ . . . . .	37
10	Area/reactivity multiplication factors for the $O_2$ - $CO_2$ - $H_2O$ reaction mechanism for $d_u = 300$ nm . . . . .	38
11	Area/reactivity multiplication factors for the $O_2$ - $CO_2$ - $H_2O$ reaction mechanism for various $d_u$ . . . . .	40
12	Area/reactivity multiplication factors for the OH- $O_2$ reaction mechanism for $d_u = 300$ nm. . . . .	41
13	Area/reactivity multiplication factors for the OH- $O_2$ reaction mechanism for various $d_u$ . . . . .	42
14	Variation of burning rate with particle diameter and temperature for $\phi = 0.6$ and $d_u = 300$ nm . . . . .	45
15	Variation of burning rate with particle diameter and temperature for $\phi = 1.0$ and $d_u = 300$ nm . . . . .	46

# LIST OF ILLUSTRATIONS (Cont'd.)

<u>Figure</u>		<u>Page</u>
16	Variation of burning rate with particle diameter and equivalence ratio for $T_f = 1665$ K and $d_u = 300$ nm . .	47
17	Variation of burning rate with particle diameter and equivalence ratio for $T_f = 1815$ K and $d_u = 300$ nm . .	48
18	Variation of burning rate with particle diameter and equivalence ratio for $T_f = 1950$ K and $d_u = 300$ nm . .	49
19	Particle-life history for $\phi = 0.2$ , $T_f = 1667$ K, $d_u = 300$ nm and $d_{po} = 73.4$ $\mu$ m . . . . .	52
20	Particle-life history for $\phi = 0.6$ , $T_f = 1663$ K, $d_u = 300$ nm and $d_{po} = 73.4$ $\mu$ m . . . . .	53
21	Particle-life history for $\phi = 0.6$ , $T_f = 1814$ K, $d_u = 300$ nm and $d_{po} = 73.4$ $\mu$ m . . . . .	54
22	Particle-life history for $\phi = 0.6$ , $T_f = 1953$ K, $d_u = 300$ nm and $d_{po} = 73.4$ $\mu$ m . . . . .	55
23	Particle-life history for $\phi = 1.0$ , $T_f = 1683$ K, $d_u = 300$ nm and $d_{po} = 73.4$ $\mu$ m . . . . .	56
24	Particle-life history for $\phi = 1.0$ , $T_f = 1683$ K, $d_u = 300$ nm and $d_{po} = 52.6$ $\mu$ m . . . . .	57
25	Particle-life history for $\phi = 1.0$ , $T_f = 1683$ K, $d_u = 300$ nm and $d_{po} = 28.7$ $\mu$ m . . . . .	58
26	Particle-life history for $\phi = 1.0$ , $T_f = 1683$ K, $d_u = 300$ nm and $d_{po} = 10.5$ $\mu$ m . . . . .	59
27	Particle-life history for $\phi = 1.0$ , $T_f = 1819$ K, $d_u = 300$ nm and $d_{po} = 73.4$ $\mu$ m . . . . .	60
28	Particle-life history for $\phi = 1.0$ , $T_f = 1952$ K, $d_u = 300$ nm and $d_{po} = 73.4$ $\mu$ m . . . . .	61
29	Particle-life history for $\phi = 1.0$ , $T_f = 1952$ K, $d_u = 300$ nm and $d_{po} = 52.6$ $\mu$ m . . . . .	62
30	Particle-life history for $\phi = 1.0$ , $T_f = 1952$ K, $d_u = 300$ nm and $d_{po} = 26.3$ $\mu$ m . . . . .	63
31	Particle-life history for $\phi = 1.0$ , $T_f = 1952$ K, $d_u = 300$ nm and $d_{po} = 10.2$ $\mu$ m . . . . .	64

# LIST OF ILLUSTRATIONS (Cont'd.)

<u>Figure</u>		<u>Page</u>
32	Particle-life history for $\phi = 1.4$ , $T_f = 1624$ K, $d_u = 300$ nm and $d_{po} = 73.4$ $\mu$ m . . . . .	65
33	Particle-life history for $\phi = 0.6$ , $T_f = 1663$ K, $d_u = 150$ nm and $d_{po} = 73.4$ $\mu$ m . . . . .	68
34	Particle-life history for $\phi = 0.6$ , $T_f = 1663$ K, $d_u = 70$ nm and $d_{po} = 73.4$ $\mu$ m. . . . .	69
35	Particle-life history for $\phi = 0.6$ , $T_f = 1953$ K, $d_u = 150$ nm and $d_{po} = 73.4$ $\mu$ m . . . . .	70
36	Particle-life history for $\phi = 0.6$ , $T_f = 1953$ K, $d_u = 70$ nm and $d_{po} = 73.4$ $\mu$ m. . . . .	71
37	Particle-life history for $\phi = 1.0$ , $T_f = 1683$ K, $d_u = 150$ nm and $d_{po} = 73.4$ $\mu$ m . . . . .	72
38	Particle-life history for $\phi = 1.0$ , $T_f = 1683$ K, $d_u = 70$ nm and $d_{po} = 73.4$ $\mu$ m. . . . .	73
39	Effect of ambient temperature on the variation of reacted mass fraction with time. $\phi = 0.6$ , $d_{po} = 73.4$ $\mu$ m, $d_u = 300$ nm. . . . .	76
40	Effect of ambient temperature on the variation of reacted mass fraction with time. $\phi = 1.0$ , $d_{po} = 73.4$ $\mu$ m, $d_u = 300$ nm. . . . .	77
41	Effect of ambient equivalence ratio on the variation of reacted mass fraction with time. $T_f = 1665$ K, $d_{po} = 73.4$ $\mu$ m, $d_u = 300$ nm. . . . .	78
42	Effect of ambient equivalence ratio on the variation of reacted mass fraction with time. $T_f = 1815$ K, $d_{po} = 73.4$ $\mu$ m, $d_u = 300$ nm. . . . .	79
43	Effect of ambient equivalence ratio on the variation of reacted mass fraction with time. $T_f = 1950$ K, $d_{po} = 73.4$ $\mu$ m, $d_u = 300$ nm. . . . .	80
44	Effect of initial particle diameter on the variation of reacted mass fraction with time. $\phi = 1$ , $d_u = 300$ nm . . . . .	82
45	Apparent particle density as a function of reacted mass fraction for the bimodal agglomerate. . . . .	84

# LIST OF ILLUSTRATIONS (Concluded)

<u>Figure</u>		<u>Page</u>
46	Transport-enhancement factor as a function of reacted mass fraction for the bimodal agglomerate. . . . .	85
47	Area/reactivity multiplication factors for the $O_2$ - $CO_2$ - $H_2O$ reaction mechanism for the bimodal agglomerate. . . . .	87
48	Area/reactivity multiplication factors for the $OH$ - $O_2$ reaction mechanism for the bimodal agglomerate .	88
49	Particle-life history for $\phi = 0.6$ , $T_f = 1663$ K and $d_{po} = 73.5$ $\mu m$ for the bimodal agglomerate. . . . .	91
50	Particle-life history for $\phi = 0.6$ , $T_f = 1953$ K and $d_{po} = 73.5$ $\mu m$ for the bimodal agglomerate. . . . .	92
51	Particle-life history for $\phi = 1.0$ , $T_f = 1683$ K and $73.5$ $\mu m$ for the bimodal agglomerate. . . . .	93

# LIST OF TABLES

<u>Table</u>		<u>Page</u>
1	Summary of Test Conditions for the Flat-Flame Burner Apparatus. . . . .	18
2	Summary of Reaction Rate Parameters in $K_{ri}$ . . . . .	30
3	Summary of Agglomerate Structure Parameters (Monodisperse Carbon-Black) . . . . .	43
4	Effect of Carbon-Black Ultimate Carbon Particle Size on Agglomerate Combustion Times . . . . .	74
5	Summary of Agglomerate Structure Parameters (Bimodal Blend). . . . .	90
6	Effect of Blending on Agglomerate Combustion Times. .	95

# NOMENCLATURE

<u>Symbol</u>	<u>Description</u>
$a_i$	Area/reactivity factor
$A_i$	Preexponential factor
$C_p$	Specific heat
$d_p$	Particle diameter
$d_u$	Ultimate carbon-black particle size
$D$	Effective binary diffusivity
$E_i$	Activation energy
$h$	Heat transfer coefficient
$i$	Mixture enthalpy
$K$	Dimensionless mass burning rate
$K_{pi}$	Equilibrium constant
$K_{ri}$	Reaction rate constant
$Le$	Lewis number
$m_p$	Total particle mass
$\dot{m}''_c$	Net mass flux of carbon
$M$	Mixture molecular weight
$M_i$	Molecular weight of species $i$
$n_i$	Reaction order
$Nu', Nu$	Conventional and corrected Nusselt number
$p$	Total pressure
$p_i$	Partial pressure of species $i$
$q''_c$	Convective heat flux at particle surface
$q''_r$	Radiative heat flux at particle surface
$r_p$	Particle radius

# NOMENCLATURE (Concluded)

<u>Symbol</u>	<u>Description</u>
R	Universal gas constant
$R_i$	Reaction rate due to species i
Sh', Sh	Conventional and corrected Sherwood number
t	Time
T	Temperature
u	Velocity
x	Axial distance from exit of flame jet
$Y_i$	Mass fraction of species i
$\tilde{Y}_i$	Mass fraction of element i
$\epsilon$	Reacted mass fraction
$\epsilon_p$	Surface emissivity
$\zeta$	Transport-enhancement factor
$\mu_{ij}$	Stoichiometric parameters
$\rho$	Density
$\sigma$	Stefan-Boltzmann constant
$\phi$	Equivalence ratio
$\chi$	Reaction parameter, Eq. (11)

## Subscripts

c	Carbon
f	Flame condition
p	Particle surface
s	Support probe, drop surface
T	Energy boundary
w	Surface of enclosure
o	Initial condition
$\infty$	Surroundings of particle

## SUMMARY

An investigation of the combustion properties of carbon agglomerates, formed during the combustion of carbon-black slurry fuels, is described. The carbon agglomerates of several noncatalyzed carbon-black formulations were considered. This included monodisperse blacks having ultimate carbon particle sizes of 70, 150 and 300 nm as well as a blend of the 70 and 300 nm blacks (50% each by mass). Since carbon-black slurry fuel formulation efforts are continuing, the formulations tested are not necessarily optimum.

Observations of the combustion properties of carbon agglomerates were made by injecting dried agglomerates (initial diameters of 10-75  $\mu\text{m}$ ) into the post-flame region of a flat-flame burner. The burner was operated at atmospheric pressure with fuel equivalence ratios in the range 0.2-1.4 and flame temperatures in the range 1620-1960 K. Gas compositions were measured by isokinetic sampling and analysis with a gas chromatograph; gas temperatures were measured with a coated fine-wire thermocouple--corrected for radiation errors; gas velocities were measured using laser Doppler anemometry. Particle diameter, mass, temperature, velocity and residence time were measured as a function of position above the point of particle injection using a combination of sampling and non-intrusive methods.

The measurements were interpreted using an analysis of agglomerate combustion developed during earlier work with carbon-black slurries in this laboratory. The model provides predictions of particle-life history, i.e., the variation of diameter, mass and temperature as a function of



## SUMMARY (Cont'd.)

time in the burner gases. The analysis treats heat and mass transfer processes in the convective environment surrounding the carbon agglomerate as well as radiative heat transfer between the agglomerate and its surroundings. Two carbon reaction mechanisms are considered: one assuming reaction between carbon and  $O_2$ ,  $CO_2$  and  $H_2O$ ; and one assuming reaction between carbon and OH (high equivalence ratios) or  $O_2$  (low equivalence ratios). The carbon agglomerates have a porous structure. This was treated using a shrinking-sphere model but employing empirical transport enhancement and area/reactivity multiplication factors to allow for effects of pores.

The model provided a good correlation between predictions and measurements using either reaction mechanism. The empirical parameters were nearly independent of flame conditions and initial agglomerate diameter. After an initial period of pore development, the empirical parameters were also relatively independent of mass fraction of carbon that was reacted. In general, the empirical parameters provide a useful method of summarizing the properties of a carbon-black formulation, since their values tend to increase for faster reacting materials.

The rate of combustion of monodisperse blacks increased slightly as the ultimate carbon-black particle size was reduced, i.e., size reductions from 300 to 70 nm yielded 10-20% reductions in particle residence times to react fixed fractions of the carbon. The carbon-black blend had an initial density that was 16% larger than the monodisperse agglomerates. Times to react fixed fractions of the carbon in the blend were also longer than for monodisperse agglomerates; ranging from 10-20% longer at diffusion-controlled conditions to as much as 50% longer at

## SUMMARY (Concluded)

kinetic-controlled conditions. These increases are only partly explained by the increased density, suggesting that the presence of the smaller particles in the blend tends to inhibit the development of pores.

Variations in initial agglomerate diameter,  $d_{po}$ , and flame conditions influenced residence times required for reaction to a much greater degree than the carbon-black formulation. Reaction residence times were proportional to  $d_{po}^{1 \text{ to } 2}$ , for the low particle Reynolds numbers (0-0.35) of the present tests--tending toward the lower power near kinetic-controlled conditions and the higher power near diffusion-controlled conditions. Residence time requirements decreased monotonically as flame equivalence ratio was reduced, for the relatively high gas temperatures of the present tests. Therefore, effects of atomization and mixing in the combustion chamber are very significant for achieving good combustion efficiencies with carbon-black slurry fuels.

## 1. Introduction

### 1.1 General Objectives

Liquid fuels having high energy densities (high energy release when burned with air per unit volume of fuel) are needed to improve the performance of volume-limited propulsion systems [1].\* It has become increasingly difficult, however, to obtain additional improvements employing liquids alone [2]. Therefore, slurries are increasingly receiving attention since they can be handled and burned similar to liquids, but have higher energy densities due to the presence of solids [2-5].

The combustion properties of slurry fuels are not well known. Past work, however, has shown that combustion of the solid in a slurry requires substantially longer combustion chamber residence times than conventional liquid fuels [2-7]. This implies that effective use of slurries will require modification of combustor designs from those used for conventional liquid hydrocarbons. Slurry fuel formulation also has a significant effect on residence time requirements, since solids loading and solid particle properties affect both atomization and combustion properties. This adds new dimensions to fuel development efforts which are not encountered for conventional liquid fuels.

The objective of the present investigation was to examine the combustion properties of a particular class of slurry fuels of interest to the Air Force, consisting of slurries using carbon-black particles as the solid phase. These slurries were formulated by Suntech, Inc., Marcus Hook, PA, as part of an Air Force sponsored fuel development effort. While the fuels investigated are representative of candidate carbon slurry fuels, they are not necessarily the most attractive formulations since

---

\* Numbers in brackets denote references.

fuel development efforts are continuing. However, the materials still provide a reasonable indication of carbon-black slurry combustion properties, useful for future fuel development efforts.

The main emphasis of the present investigation was to observe the combustion of the solid phase originating from individual slurry drops. In order to simulate practical combustor conditions, observations were made of free particles injected into the post-flame region of a flat-flame burner operating at atmospheric pressure (initial particle diameters less than 100 microns). Analysis of the process was also undertaken in order to assist interpretation of the measurements.

In the following, past work on combustion properties of carbon-black slurries is reviewed prior to specifically identifying the objectives of the present investigation. Experimental and theoretical methods used during the investigation are then described. The report concludes with a discussion of experimental results and the comparison between predictions and measurements. The entire investigation is considered here, although portions of the study have also been reported elsewhere [8-10].

## 1.2 Background

Existing information on the combustion properties of carbon-black slurries is relatively limited. Carbon-black slurries have been burned in a gas-turbine combustor, by Bruce et al., [2,3] and in well-stirred reactors by Salveson [5], and Lavid and Ruth [11]. These studies indicated that carbon slurries required a greater combustor residence time for good combustion efficiency than conventional liquid fuels, however, the mechanism of combustion was not established.

Law and coworkers [12,13] considered the related problem of coal slurry combustion--observing both supported and freely falling drops burning in air. It was found that the process could be broadly divided into two stages. The liquid fuel evaporated or burned in the first stage, leaving an irregular agglomerate of the coal particles. The agglomerate subsequently reacted or was quenched, depending upon ambient conditions, during the second stage of the process.

Earlier studies in this laboratory considered the combustion of large carbon-black slurry drops, 400-1000  $\mu\text{m}$  diameter, supported at various positions in a turbulent diffusion flame [4,6,7]. It was found that carbon-black slurries burned in a two-stage process similar to coal slurries. The liquid evaporated rapidly, leaving a porous agglomerate containing all the carbon-black particles originally in the drop. The agglomerate then heated-up and either reacted or was quenched depending upon position in the flame. Even at maximum agglomerate reaction rates, however, the second stage was at least an order of magnitude longer than the liquid evaporation stage. Therefore, agglomerate combustion represents the rate-controlling step for good combustion efficiency.

A model of slurry drop combustion was also developed during earlier work in this laboratory [6,7]. Liquid gasification was treated following past practice for analysis of sprays [14-16], but extended to allow for the presence of solid in the liquid phase. Agglomerate reaction was modeled by extending the carbon particle combustion analysis of Libby and Blake [17]. Two carbon reaction mechanisms were considered: (1) the approach of Neoh et al. [18] for soot combustion, where carbon reaction with OH dominates at high fuel equivalence ratios while reaction with  $\text{O}_2$

becomes significant at low equivalence ratios; and (2) the approach of Libby and Blake [17] for reaction of carbon with  $O_2$  and  $CO_2$ , but extended to include reaction with  $H_2O$ . The analysis of liquid evaporation was successfully evaluated using data from supported pure liquid drops in the diffusion flame [8]. The agglomerate combustion model, using either reaction mechanism, also yielded good comparison with measurements for a wide range of flame conditions--after specifying empirical constants to allow for effects of catalyst and pores on gas-phase transport and reactive surface area. Combining these two models yielded good predictions of slurry drop-life histories (the variation of drop/particle size and temperature with time) throughout both stages of the process [7]. Major limitations of this work, however, were that drop sizes were large in comparison to drops in conventional combustors, only a single slurry formulation was studied, and effects of pores on the density of the agglomerates was not studied. This raises significant questions concerning the generality of the results--particularly the empirical parameters--for practical combustor conditions. The effect of fuel formulation--particularly carbon-black type--on slurry combustion properties was also not established.

### 1.3 Specific Objectives

The present investigation extends the study of carbon-black slurry combustion--considering particle sizes more representative of practical combustors (initial diameters of 10-75  $\mu m$ ). Since the liquid gasification stage is conventional [6,7], the study was limited to agglomerate combustion properties. Freely moving agglomerate particles were observed in the post-flame region of a laminar flat-flame burner,

yielding the variation of agglomerate temperature, diameter, mass and velocity as a function of residence time.

In addition to effects of overall agglomerate size, experiments were also conducted to determine the combustion properties of various carbon-blacks with ultimate carbon particle sizes in the range 70-300 nm. Limited testing was also completed on a blend consisting of carbon blacks of different ultimate carbon particle size, since blends may be required to yield slurries having acceptable rheological and stability properties. All the measurements were interpreted using the agglomerate combustion model developed earlier [6,7].

## 2. Experimental Methods

### 2.1 Apparatus

A sketch of the flat-flame burner apparatus appears in Fig. 1. The arrangement consists of a slurry-droplet generator, a convergent-flow section, a liquid evaporation section, and a flat-flame burner. The mono-disperse drops produced in the drop generator are dried in a heated section of tubing leaving an agglomerate of solid-particles. The carbon agglomerates then pass through the post-flame region of a flat-flame burner where observations are made. A sampling probe placed above the flat-flame burner collects the carbon agglomerates for further analysis.

The flat-flame burner was fueled with a mixture of gaseous nitrogen, oxygen, carbon dioxide, carbon monoxide, methane and hydrogen. The mixing pressure was monitored with a Heise absolute-pressure gauge having a pressure range of 0.0-0.41 MPa. Gas flow rates were controlled with pressure regulators and needle valves and measured with rotameters. All rotameters were calibrated using wet-test meters.

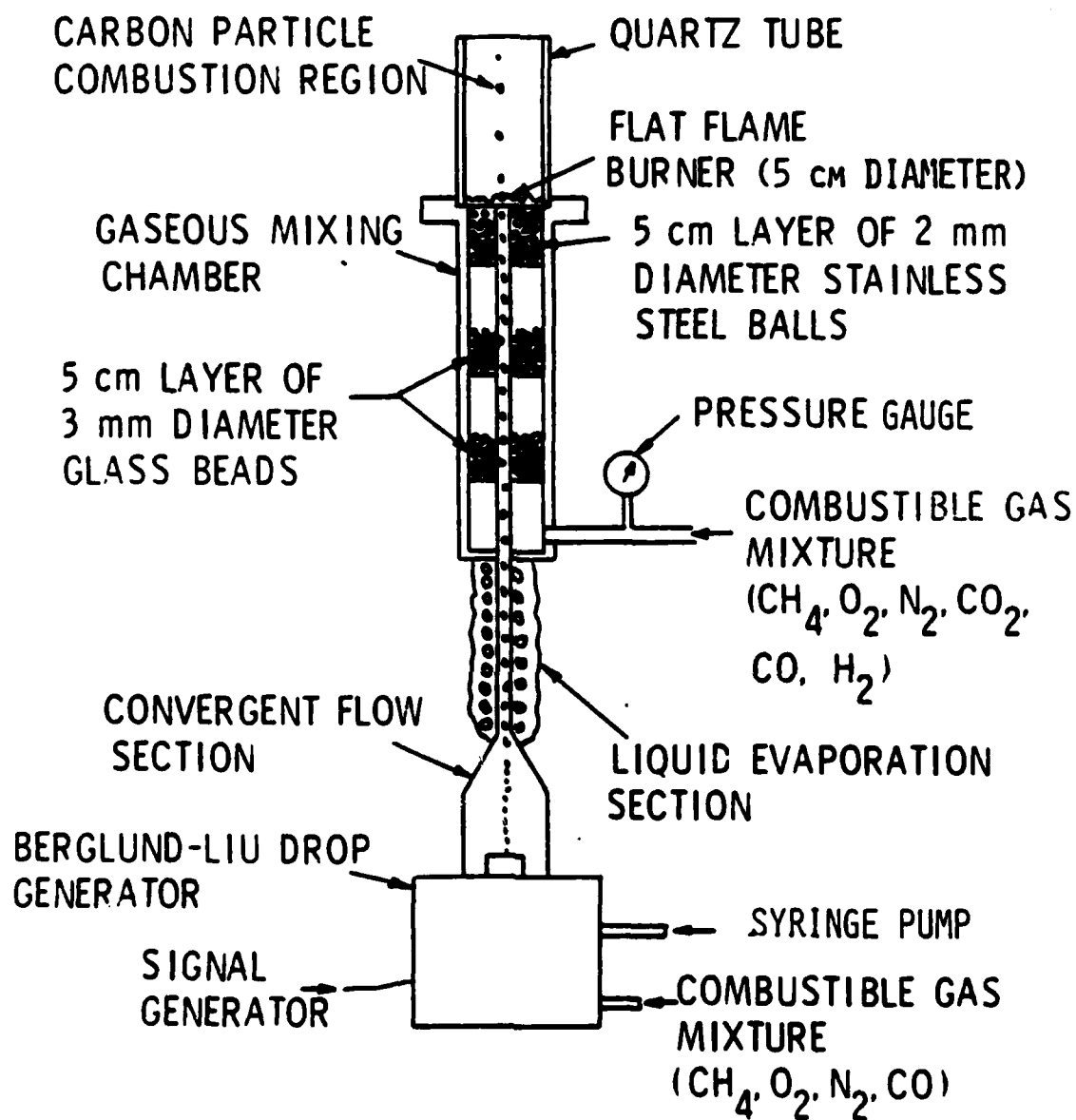


Figure 1. Schematic of the flat-flame-burner apparatus.



Gas mixing was aided by flowing the gases through a 1.5 m length of 10 mm I.D. tubing. The gas mixture then entered the mixing chamber through an inlet near its bottom. The gas mixing chamber was constructed from a 51 mm nominal diameter schedule 40 stainless-steel welded pipe and had a length of 300 mm. To provide a thoroughly mixed fuel gas with a uniform-velocity profile, several layers of small beads separated by void spaces were provided in the gas mixing chamber--as indicated in Fig. 1. A flat flame was stabilized near the top surface of the burner. The flame was approximately 1-2 mm thick and was completely uniform and stable at all operating conditions.

Equivalence ratios between 0.2 and 1.4 were used during the tests. The temperatures of these flames could be varied between 1600 K and the softening temperature of stainless steel. By blending carbon monoxide, carbon dioxide, hydrogen and methane, the C/H ratio could be varied over a very wide range. Finally, the bed of stainless-steel balls at the top of the burner inhibited flash-back and aided flame attachment so that gas velocities could be varied between 0.5 and 3.0 m/s.

Once the flame was ignited, a 53 mm I.D. quartz tube was placed on the burner surface. The tube surrounded the flame to prevent entrained air from mixing with the products of combustion and lowering the flame temperature. The quartz tube also helped maintain a uniform high temperature of the products of combustion far above the burner. The quartz tube was cut into lengths of 50 mm to 200 mm, in 50 mm increments, to facilitate the access of measuring probes at various locations above the burner surface.

The drop generator consisted of a TSI model 3050 Berglund-Liu vibrating-orifice monodisperse-aerosol generator, a Sage model 355

continuously-variable syringe pump, and a Hewlett-Packard model 3310B function generator. Three orifices were used in the Berglund-Liu drop generator: a TSI model 10356 100  $\mu\text{m}$  orifice, a TSI model 10355 50  $\mu\text{m}$  orifice and a TSI model 10353 20  $\mu\text{m}$  orifice. Both a 10 and 50 ml reusable multifit syringe with metal luer tips were used with the syringe pump.

A mixture of methane, oxygen, carbon monoxide and nitrogen was used in the Berglund-Liu droplet generator to dilute and disperse the drops. These gases were mixed to yield the same equivalence ratio and C/H ratio as the fuel mixture in the flat-flame burner assembly after evaporation of the hydrocarbon carrier of the slurry. The flow rates of the dilution and dispersion flows were metered and measured similar to the main burner gases.

The slurry had to be thinned in order to generate slurry droplets with the drop generator without clogging the orifice. This involved mixing JP-10 with the slurry fuel. It was found that the carbon particles remained suspended in the mixture for several hours. Thus, mixtures of carbon slurry and n-pentane ranging from one to five parts n-pentane per part of volume of slurry were used in the droplet generating system.

The syringe pump was adjusted to the minimum velocity necessary to establish a liquid jet emerging from the orifice in the Berglund-Liu droplet generator. The frequency of the signal generator was set at a value between 1000 and 4000 Hz. Thus, between 1000 and 4000 drops per second were formed ranging in initial diameter between 24 and 270  $\mu\text{m}$ . The 50 ml syringe allowed continuous operation for up to 3.5 hours.

The Berglund-Liu droplet generator exhausted the slurry droplets into a 50 mm length of a 115 mm diameter plexiglass tube. The plexiglass tube was connected to a stainless-steel 45° convergent cone, which was

attached to the plexiglass with silicon sealant. The cone was 40 mm high, had a 115 mm diameter opening at the base and a 3.4 mm diameter opening at its tip. The outlet of the cone was welded to a tube having an inner diameter of 3.4 mm and a length of 610 mm. The top end of this tube was welded to a tube with a 1.8 mm inner diameter and a length of 460 mm. This tube passed through a Conax thermocouple seal at the bottom of the mixing chamber. The top end of the 1.8 mm diameter tube was flush with the surface of the flat-flame burner.

Nichrome heater wire and fiberfrax ceramic insulation were wrapped around the outside of the 3.4 mm diameter section. Thus, when a particle left the Berglund-Liu droplet generator it was accelerated through the convergent core section of the droplet guide. Next, the droplet entered the 3.4 mm diameter section, which was heated to 600 K. In this region the liquid fuel evaporated leaving behind an agglomerate of solid-carbon particles. The evaporating liquid also served to further accelerate the agglomerate. When the gas flow emerged from top of the 1.8 mm diameter tube it had the same equivalence ratio, C/H ratio and velocity as the surrounding gas of the flat-flame burner. The particle velocity was somewhat lower than the flow velocity due to the gravity effects on the particle. The initial size of the carbon agglomerates leaving the 1.8 mm diameter tube ranged between 10 and 75  $\mu\text{m}$ . The particles continued to flow up through the quartz tube as they reacted.

Figure 2 is a time exposure photograph of the carbon agglomerates passing through the flat-flame burner and reacting. The quartz tube shown in Fig. 1 was not in place for this photograph, and the particles cool upon exiting the hot potential core of the flame. Although the particles do

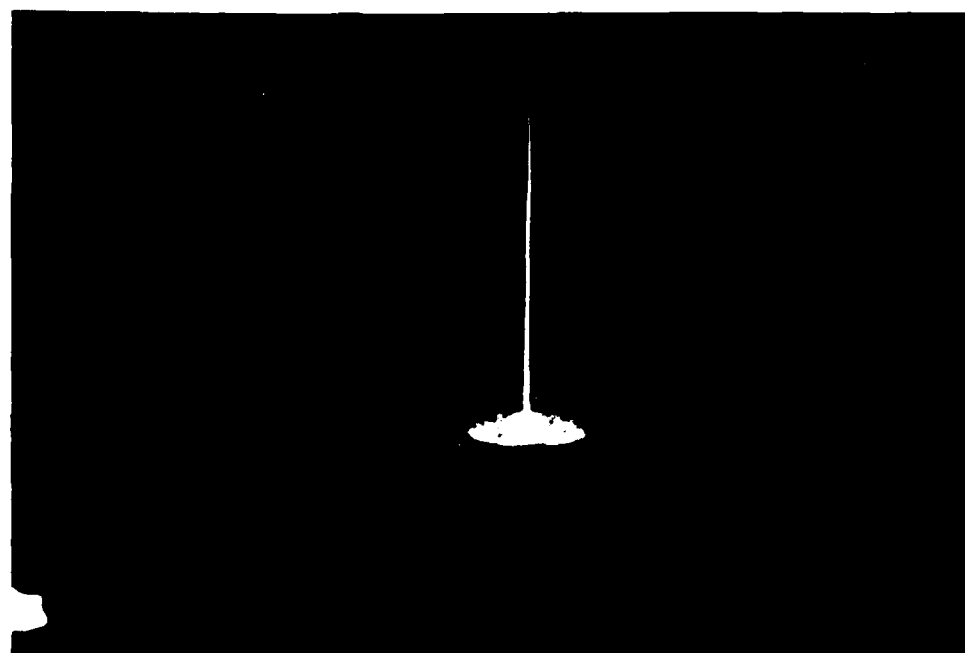


Figure 2. Time-exposure photograph of particles reacting above the flat-flame burner.

disperse somewhat, the photograph shows that the particles travel in a straight line producing a streak approximately 3 mm wide at the base for an initial particle diameter of 73.4  $\mu\text{m}$ .

## 2.2 Particle Environment Measurements

### 2.2.1 Velocity Measurements

Gas velocities were measured along the axis of the burner using a laser Doppler anemometer (LDA). This involved a 5 mW helium-neon laser operating in the dual-beam backscatter mode (241 mm focal length, free aperture of 60 mm, 50 mm beam spacing, photodetector aperture of 0.256 mm, with 200 mm focal length detector focusing lens). This arrangement produced an ellipsoidal probe volume 0.31 mm in diameter and 3 mm long. The LDA output was processed using a frequency tracker. The gas flow was seeded with 0.3  $\mu\text{m}$  aluminum oxide particles for velocity determinations using a reverse cyclone seeder [19].

### 2.2.2 Temperature Measurements

The gas temperatures along the axis of the post-flame region of the flat-flame burner were measured using a thermocouple probe. The probe was constructed from 25  $\mu\text{m}$  diameter platinum/platinum-10% rhodium wires which were spot-welded onto 50  $\mu\text{m}$  diameter lead wires of the same material. The probe was mounted on a traversing mechanism which allowed it to be positioned at various locations along the flame axis. The emissivity of the thermocouple was maintained at approximately  $0.22 \pm 0.02$  by coating the thermocouple with a layer of silica roughly 3  $\mu\text{m}$  thick [20]. The silica layer also eliminated catalytic decomposition heating of the probe.

The thermocouple probe was calibrated with a 50  $\mu$ m chromel/alumel thermocouple in a furnace environment where the radiation errors are minimized. Both thermocouples agreed within 6°C, up to a temperature of 1500 K, which was the maximum temperature of the furnace. The maximum radiation correction for this temperature probe was 39°C over the test range. The reference junction was at the ambient temperature, shielded from the flame. An integrating digital voltmeter was used to average the signal over a two-minute period.

### 2.2.3 Concentration Measurements

The concentration measurements were made using a gas chromatograph (Varian model 3720) incorporating a thermal-conductivity detector. The gas samples were extracted from the flow at nearly isokinetic conditions using a water-cooled probe constructed of stainless steel. The inlet of the probe was 0.7 mm in diameter. The temperature of the cooling water was maintained constant about 338 K ( $\pm$  2 K) to avoid the condensation of fuel and water vapor in the probe. An ice bath cold trap was placed in the sampling line, however, in order to condense water prior to gas analysis.

The samples were analyzed using a carbosieve column (Supleco, Carbo-sieve, type S, 100/120 mesh, 2.1 m x 3.2 mm stainless steel; 4 min. hold at 35°C; programming, 25°C to 175°C at 25°C/min.) for the analysis of hydrogen, oxygen, nitrogen, carbon monoxide, carbon dioxide and methane. The concentration of water vapor was obtained by a conservation of element analysis. Helium at a flow rate of 30 ml/min. was used as carrier gas. The output of the hot-wire thermal-conductivity detector was recorded with a Varian strip chart recorder.

The Carbosieve column was calibrated for hydrogen, oxygen, nitrogen, carbon monoxide, carbon dioxide and methane using calibration gases manufactured by the Scott Company. A 0.5 ml sample size was used for all composition measurements.

## 2.3 Particle Measurements

### 2.3.1 Velocity Measurements

The particle velocity measurements were made with the LDA system used to measure the velocity of the gas above the flat-flame burner. The particle spacing was also measured with the LDA system. A Nicolet, model 206, digital oscilloscope was employed to measure the time between the pedestal signals generated by individual particles. Since the particle velocity was known, the distance between particles could be determined.

### 2.3.2 Temperature Measurements

The temperature of the carbon particles as they reacted above the flat-flame burner assembly was measured using an optical pyrometer. The pyrometer used was a Leeds and Northrup, model 8622, with a temperature range of 1000-3150 K. The optical pyrometer was calibrated using the platinum/platinum-10% rhodium thermocouple temperature probe employed for gas temperature measurements.

The particle temperature measurement is a brightness temperature, assuming that the particles are black bodies. This technique is particularly adapted for temperature measurements of high temperature particle streams, since it is independent of the number of particles observed at any instant.

### 2.3.3 Diameter Measurements

The probe used to collect the carbon-agglomerate particles for analysis is shown in Fig. 3. The probe was positioned along the flame

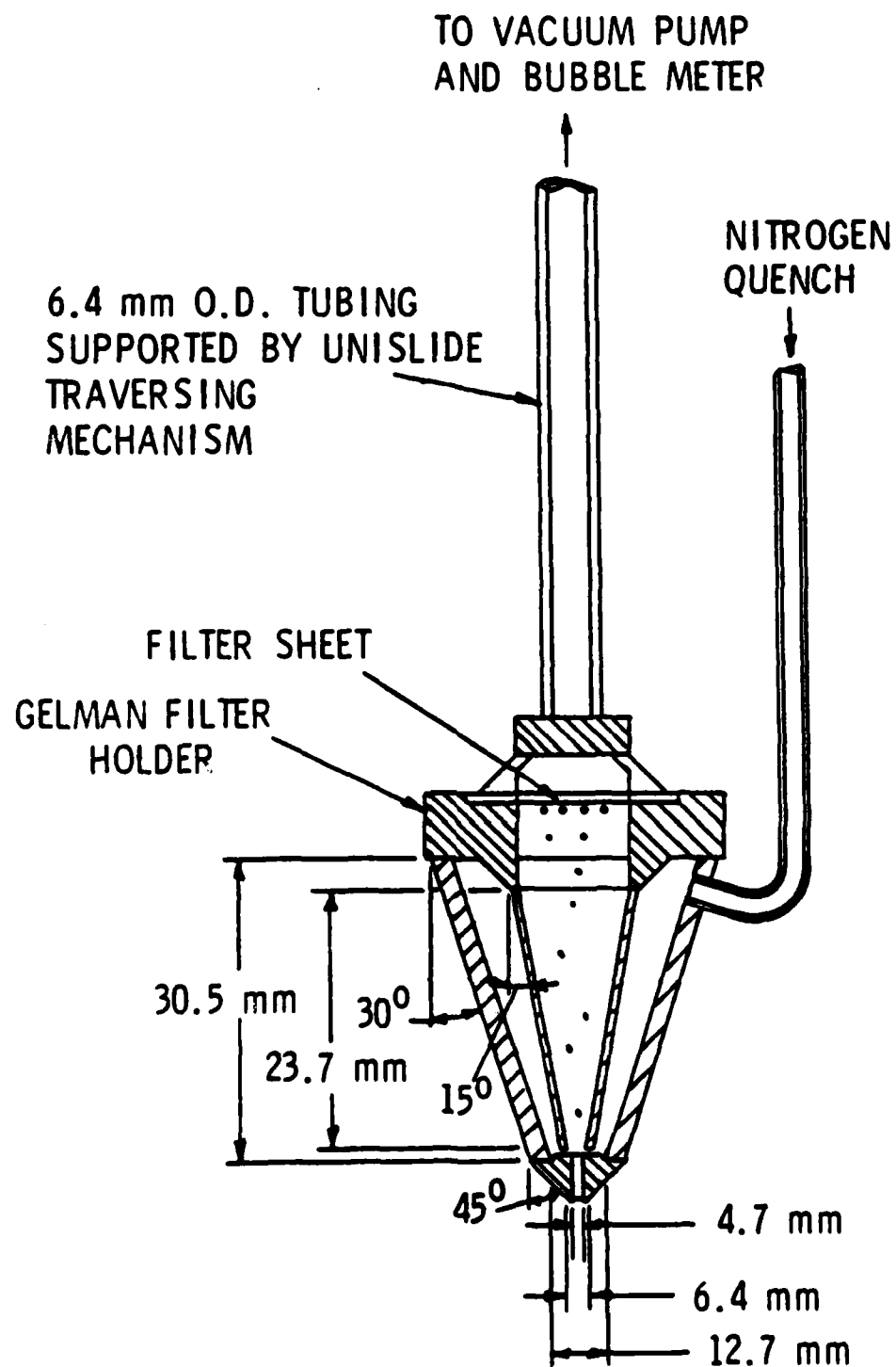


Figure 3. Sketch of the quenching probe used for particle collection.



centerline at various locations above the flat-flame burner with a traversing mechanism. The collection filter was constructed from a Gelman, model 2220, stainless-steel inline filter holder. The upstream end of the filter holder was modified to include two concentric stainless-steel cones which were silver soldered to the upstream face of the filter holder. The inner cone had a 6.4 mm inlet, a  $15^{\circ}$  angle, and a length of 23.7 mm. The outer cone had a 12.7 mm inlet, a  $30^{\circ}$  angle, and a length of 30.5 mm. Both cones had an approximate thickness of 1.6 mm. A stainless-steel tip was silver soldered to the outer cone. The tip was 12.7 mm in diameter, 6.4 mm in length and tapered to a 4.7 mm inlet with an angle of  $45^{\circ}$ .

A nitrogen-quenching flow passed through the outer cone of the filter holder from a 6.4 mm diameter tube. The nitrogen passed between the two concentric cones to the inlet of the collection probe where the reacting particles were quenched as they entered the probe. The particles then were collected on 47 mm diameter Alpha metrical, grade Alpha-200, Gelman membrane filters, model 60585. These filters have a pore size of 0.2  $\mu\text{m}$ , a thickness of 65  $\mu\text{m}$ , a very high chemical resistance, and a maximum operating temperature of 450 K.

The particle collection probe was connected to a vacuum pump. The velocity at the inlet to the collection probe was matched with the gas velocity at the sampling location, using a regulating valve and bubble flow meter. A sufficient amount of nitrogen gas was mixed in the collection filter to lower the gas temperature to 400 K and quench the reacting carbon particles. The operating pressure in the filter was approximately 71 kPa which also tended to help quench the reacting carbon particles.

A quick response toggle operated bellows valve was also placed in the flow line between the collection probe and the vacuum pump so that the collection filter could be operated for short time periods. Small sampling times resulted in widely spaced single particles on the collection filter. After the sample was collected the filter medium was removed and the sizes of the particles collected were analyzed on a scanning electron microscope (SEM).

The particle diameter quoted here is the arithmetic average of six diameter measurements per particle each spaced  $30^\circ$  apart and passing through the center of the particle. At least eight particles were examined in order to obtain an average particle size.

#### 2.3.4 Mass Measurements

The filter collection probe illustrated in Fig. 3 was employed to collect particles for particle mass measurements. However, the sampling period for the mass measurements was increased to between 10 seconds and 2 hours. A stainless-steel filter medium was also substituted for the Alpha metrical filter described earlier. The stainless-steel filter was a Dynalloy filter, model X4, manufactured by the Fluid Dynamics Branch of Brunswick Technetics. The filters had a diameter of 47 mm, a thickness of 300  $\mu\text{m}$ , a pore size of 3  $\mu\text{m}$ . The filters were preconditioned by baking them for three hours at a temperature in excess of 1000 K to burn off any contaminants.

After the carbon particles were collected, the filter was removed and placed in an evacuated reaction chamber. The temperature was raised to 500 K, and the pressure was lowered below 4 kPa. These conditions were maintained for several hours to remove any condensibles entrapped within the

particles. The dried carbon particles were then exposed to an oxygen and hydrogen environment. The temperature was then raised above 1000 K and the pressure increased to 85 kPa. These conditions were maintained for several hours until all of the carbon was reacted. By measuring the carbon dioxide and carbon monoxide concentrations in the reaction chamber, the mass of carbon initially present on the filter was determined. Knowing the total number of particles collected during the collection period (from the droplet production frequency) gave the mass of carbon per particle. The pressure of the reaction chamber was kept below atmospheric to monitor whether the system developed leaks, since nitrogen would show up in the gas analysis of the reacted gas if a leak was present. The gas chromatograph system used for these measurements was the same as for the particle environment measurements.

The carbon slurry mixture incorporated several additives to assure stability. In order to determine whether these additives altered the carbon mass measurement, a slurry mixture without additives was prepared in this laboratory and results with this material were compared with the stabilized samples. It was found that mass measurements were independent of the presence or absence of additives.

#### 2.4 Experimental Conditions

Experimental conditions for the present investigation are summarized in Table 1. The temperature and composition of major species were found from the gas environment measurements described in Section 2.2. The concentration of OH is significant for one of the carbon agglomerate reaction mechanisms. This concentration was found using the NASA CEC-72 chemical equilibrium computer program [21].

Table 1. Summary of Test Conditions for the Flat-Flame-Burner Apparatus<sup>a</sup>

Flame Condition	Equivalence Ratio	C/H Ratio <sup>b</sup>	Temperature (K)	Velocity <sup>c</sup> (m/s)	Mass Fraction						
					O <sub>2</sub>	N <sub>2</sub>	CO <sub>2</sub>	CO	H <sub>2</sub>	H <sub>2</sub> O <sup>d</sup>	OH <sup>e</sup>
1	0.2	2.99	1667	1.47	0.569	0.252	0.098	00	00	0.080	--
2	0.6	2.97	1663	1.52	0.098	0.719	0.101	--	--	0.083	--
3	0.6	2.96	1814	1.54	0.111	0.681	0.114	--	--	0.094	--
4	0.6	2.98	1953	1.49	0.125	0.640	0.129	--	--	0.105	0.001
5	1.0	2.96	1683	1.50	--	0.813	0.102	--	--	0.084	--
6	1.0	2.99	1819	1.52	0.001	0.789	0.115	0.001	--	0.095	--
7	1.0	2.99	1952	1.53	0.002	0.761	0.128	0.002	--	0.107	--
8	1.4	3.10	1624	1.52	--	0.767	0.077	0.059	0.004	0.098	--

<sup>a</sup>The dispersed carbon is a medium thermal carbon black having ultimate particle size of 70-300 nm, and analysis by weight: C, 99.3%; H, 0.3%; O, 0.1%, provided by R. S. Stearns and L. W. Hall, Jr. of Suntech Group. The tests were conducted at 97 kPa.

<sup>b</sup>Mass Basis.

<sup>c</sup>Ambient velocity at injector exit.

<sup>d</sup>H<sub>2</sub>O mass fraction was obtained from H and O element balances.

<sup>e</sup>OH mass fraction was found using Ref. 21.

The temperature and composition of the burner gas were essentially constant over the measuring region (0-200 mm from the burner)--except for the first 2 mm above the burner surface where the burner flame was present. Gas velocities, however, increased by as much as a factor of two, from the values at the burner surface given in Table 1, due to boundary layer development on the quartz tube surrounding the post-flame region. A more complete tabulation of burner-gas properties is given in Appendix A.

Initial particle velocities varied, depending upon size, due to effects of gravity. The velocity defect of the agglomerates, also varied as reaction proceeded. Therefore, measured local values of the velocity defect were used to estimate the transport properties of the flow around the particle.

Agglomerate spacing varied during the tests, reaching a minimum of eight particle diameters. Results of Sangiovanni and Kesten [22], for monodisperse streams of drops, suggested that interparticle effects are relatively small for the present spacings. Specific examination of present conditions indicated that reaction of the particle stream varied local reactant concentrations generally less than 10%; therefore, the test conditions are essentially representative of results for individual particles.

Measurement accuracy varied significantly over the particle lifetime. Estimates of average errors in agglomerate properties over the test range are: diameter, 10%; velocity defect, 10%; velocity, 5%; mass, 28%; residence time, 20%; axial location, 5%; and temperature, 10%. Burning rates, based on particle diameter, had estimated errors of 15-30% for particle diameters of 2-75  $\mu\text{m}$ . All measurements were repeatable within these ranges.

Properties of the carbon-blacks used during the tests are also summarized in Table 1. They consisted of medium thermal carbon blacks with ultimate particle sizes ranging from 70-300 nm. The fuels were originally mixed with hydrocarbon carriers and stabilized. However, they were diluted for present use in the drop generator as noted earlier. Since only dried agglomerates were considered during the present study, and no effect of additives was found, carrier properties are irrelevant and have been omitted from the table.

### 3. Theoretical Methods

#### 3.1 Description of Model

Slurry drop combustion is analyzed in two stages. The first stage treats evaporation of the liquid carrier to produce the carbon agglomerate. This portion of the analysis is a straightforward application of drop evaporation theory, aside from allowing for the thermal capacity and volume of the dispersed carbon particles. Since the liquid phase was not considered during this investigation, this analysis and its evaluation will not be considered here. A complete description of the theoretical treatment of the liquid evaporation period is presented in Refs. 6, 8 and 10.

Given initial conditions based on analysis of the liquid evaporation process, the agglomerate combustion model provides the subsequent life-history of the particle during the second stage of the process. This involves computation of agglomerate mass, size, temperature, velocity and position as a function of time--for given ambient conditions of the particle. Only the major features of the model will be presented here, in order to assist understanding of the present results. Complete details of the agglomerate combustion model may be found in Refs. 6, 7 and 10.

The model must account for the physical features of agglomerates formed from carbon-black slurries. The nature of the agglomerates can be seen from the SEM photographs of Fig. 4--one at the start of reaction and a second after 12.2% of the agglomerate mass was reacted. The nonreacted particle has some irregularities, but is roughly spherical with a relatively smooth surface. The particle diameter decreases as reaction proceeds, however, the particle also becomes porous with increased porosity near the surface--similar to observations of large agglomerates [6,7].

The variation of particle density with extent of reaction provides a more quantitative indication of the extent of subsurface reaction and porosity. This is illustrated in Fig. 5 for the complete range of particle environments considered here (300 nm ultimate carbon particle size). The unreacted density of  $1820 \text{ kg/m}^3$  agrees with the value reported by Bruce et al. [2] for dried slurries of the same carbon black. The variation of density with extent of reaction is relatively independent of particle diameter and flame condition, yielding the following empirical correlation

$$\rho_p = \rho_{po} (1 - \epsilon)^{0.6} \quad (1)$$

A characteristic thickness ( $\delta$ ) of the pore zone can be defined as the difference in radius between the particle and a particle having the same mass but the initial density. The density correlation of Eq. (1) yields

$$\delta/r_p = 1 - (1 - \epsilon)^{0.2} \quad (2)$$

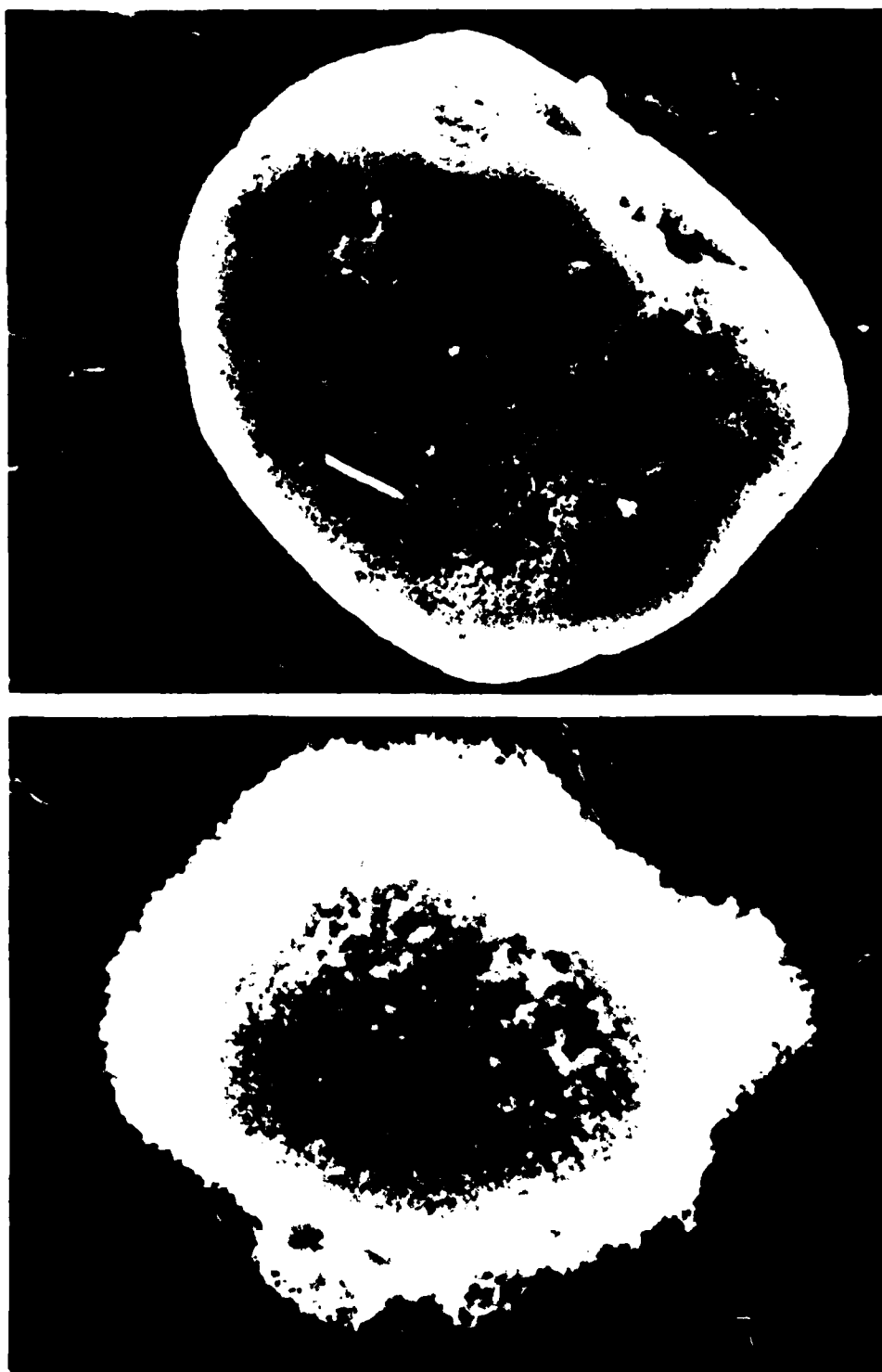


Figure 4. SEM photographs of collected particles:  $\phi = 1$ ,  $T_f = 1683$  K,  $d_{po} = 73.4$   $\mu\text{m}$ . Upper and lower photographs have reacted mass fractions of 0.000 and 0.122, respectively, and  $d_u = 300$  nm.



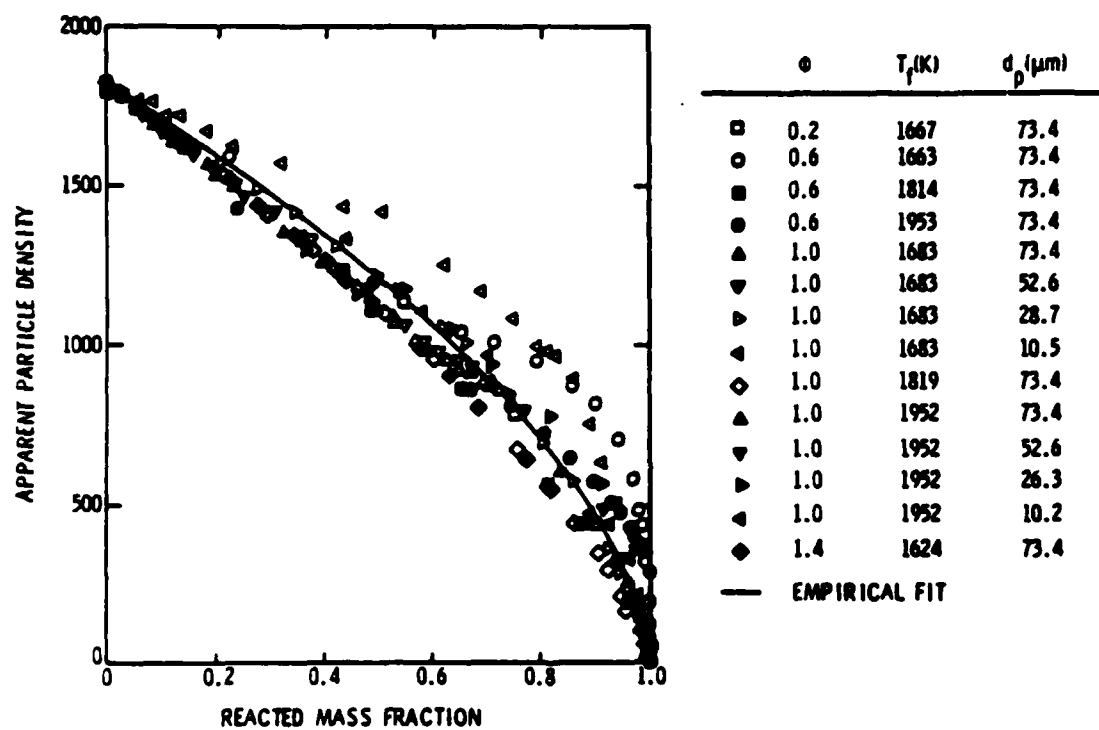


Figure 5. Apparent particle density as a function of reacted mass fraction for  $d_u = 300$  nm.

Equation (2) indicates that  $\delta/r_p < 25\%$  for  $\epsilon < 75\%$ . Therefore, the particle decreases in size, accompanied by the development of a pore structure which is confined to a relatively small fraction of the current particle radius, over much of the particle lifetime.

Pore combustion models have been constructed for burning coal particles, however, such models are relatively complex. A great deal of information on pore structure is also needed prior to computations with pore models. While such developments are a desirable long-term objective, work along these lines was deferred for the present, in favor of a semi-empirical treatment of effects of pore structure. A shrinking sphere model was considered, since this approach represents the major features of the process. Empirical parameters were defined to treat enhancement of convective transport rates and increased surface area for reaction due to pores. The latter parameters also represent effects of catalyst [6,7]. Fortunately, the empirical parameters are relatively independent of particle size and flame environment, similar to density. Therefore, they provide a convenient method for summarizing effects of pores.

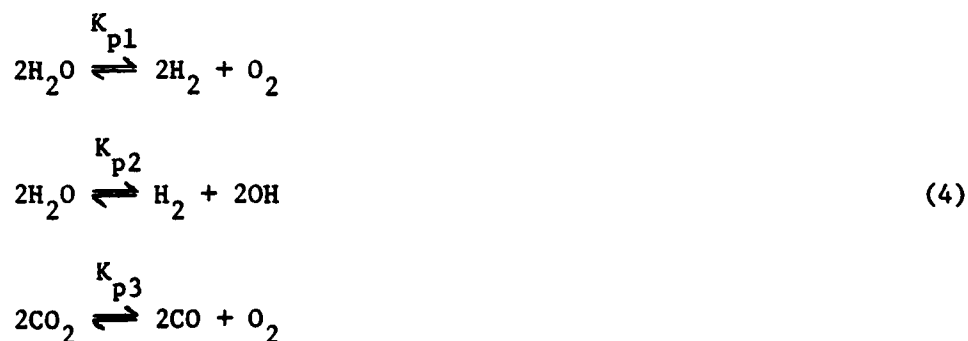
The model was an extension of the carbon combustion analysis of Libby and Blake [17]. Major assumptions of the model are: spherical isolated particle; uniform particle properties at each instant consisting of pure carbon; quasisteady gas phase; mass diffusion only by concentration gradients; all species assumed to have equal molecular weights and specific heats; and constant average gas-phase properties at each instant of time (evaluated at the reference state given elsewhere [6,7]), and radiation from the agglomerate to the surroundings treated assuming a transparent flame and an opaque blackbody agglomerate.

### 3.2 Gas-Phase Transport

Since binary diffusivities are equal, mass transport is conveniently expressed in terms of element mass fractions. Four elements, C, O, N and H, and seven species,  $O_2$ ,  $N_2$ ,  $CO_2$ ,  $CO$ ,  $H_2O$  and  $OH$ , appear in the analysis. The element and species mass fractions are related as follows:

$$\tilde{Y}_i = \sum_{j=1}^7 \mu_{ij} Y_j, \quad i = 1, 4 \quad (3)$$

where  $\mu_{ij}$  is the mass fraction of the  $i$ 'th element in the  $j$ 'th species. Given the  $\tilde{Y}_i$  at a particular location, Eq. (3) provides four equations to determine the seven unknown  $Y_i$ . Three additional equations were obtained from the assumption of thermodynamic equilibrium. The equilibrium relations used were:



where the  $K_{pi}$  are known functions of temperature.

The  $\tilde{Y}_i$  are found by solving gas-phase transport equations. During this solution, effects of convection were evaluated using film theory, where the gas phase is treated as a spherically symmetric layer having an outer radius found from empirical convection correlations for spheres as follows [23]:

$$r_{\infty T}/r_p = Nu/(Nu-2) \quad ; \quad r_{\infty M}/r_p = Sh/(Sh-2) \quad (5)$$

The effect of flow through the pore structure was considered by defining a transport enhancement factor,  $\zeta$ , where

$$Nu = \zeta Nu' ; \quad Sh = \zeta Sh' \quad (6)$$

$Nu'$  and  $Sh'$  are the Nusselt and Sherwood numbers of smooth spheres found similar to past work on drop transport properties [14-16,23].

Denoting carbon as element 1, the film theory analysis yields the following expressions for the  $\tilde{Y}_1$  at the particle surface:

$$\tilde{Y}_{1p} = 1 - (1 - \tilde{Y}_{1\infty}) \exp(-2K/Sh) \quad (7)$$

$$\tilde{Y}_{ip} = \tilde{Y}_{i\infty} \exp(-2K/Sh) \quad , \quad i = 2,4 \quad (8)$$

where

$$K = \dot{m}_c'' r_p / \rho D \quad (9)$$

The analogous expression for the heat flux at the particle surface is

$$\frac{q_c'' C_p}{(i_p - i_\infty)} = \frac{\lambda K / r_p}{1 - \exp(2K/LeNu)} \quad (10)$$

Given the ambient conditions, the temperature of the particle, and  $K$ , Eqs. (3)-(10) provide the  $\tilde{Y}_{1p}$ ,  $Y_{1p}$  and  $q_c''$ . The complete solution requires a relationship between  $K$  and the  $Y_1$ . This is provided by the surface reaction properties discussed next.

### 3.3 Surface Reaction Models

There are numerous uncertainties in modeling the reaction of a porous carbon agglomerate in a flame. The flame environment contains

several species which are potential oxidants of carbon, e.g.,  $H_2O$ ,  $CO_2$ ,  $O$ ,  $O_2$  and  $OH$ , and the reaction mechanism is not well established. Since the material is porous, reaction is not limited to the apparent outer surface of the agglomerate. Carbon substances exhibit intrinsic variations in reactivity due to their surface structure. Finally, the presence of a catalyst is known to influence reaction rates [6,7].

The effect of various gaseous reactants was treated by considering a mechanism recently proposed by Neoh et al. [18], as well as an extension of an earlier approach employed by Libby and Blake [17]. The effect of pores, surface reactivity and catalysts was treated by identifying empirical area/reactivity factors, selected to best match the present measurements. (It was found that a fixed value, for a given carbon black and reaction, could correlate the measurements over the range of the data.)

Neoh et al. [18] concluded that  $OH$  is the dominant carbon oxidant under fuel-rich conditions; that  $O$  is of secondary importance at temperatures below 2000 K; and that  $O_2$  becomes a significant factor for fuel-lean conditions, particularly at lower temperatures. Present test conditions correspond to these circumstances, therefore, carbon reaction with  $OH$  and  $O_2$  was considered, while ignoring the remaining species. Neoh et al. [18] found that reaction of carbon with  $OH$  could be represented by assuming a constant collision efficiency, yielding the following reaction rate expression

$$R_1 = K_{r1} P_{OH} \quad (11)$$

The results of Nagle and Strickland-Constable [24] were employed to determine the rate of reaction of carbon with  $O_2$ . These rate expressions are also in reasonable agreement with later measurements by Park and Appleton [25]. The carbon reaction rate is given by

$$R_2 = K_{r2} P_{O_2} \chi / (1 + K_{r3} P_{O_2}) + K_{r4} P_{O_2} (1 - \chi) \quad (12)$$

where

$$\chi = [1 + K_{r5} / (K_{r4} P_{O_2})]^{-1} \quad (13)$$

The measurements of Neoh et al. [18] suggest that the larger of  $R_1$  or  $R_2$  should represent the reaction rate at any condition. Therefore, the dimensionless mass burning rate was determined from

$$K = (r_p / \rho D) \max (a_1 R_1, a_2 R_2) \quad (14)$$

where the  $a_i$  appearing in Eq. (14) are the empirical area/reactivity multiplication factors.

The carbon reaction mechanism used by Libby and Blake [17] considers reaction with  $O_2$  and  $CO_2$  employing the following expressions:

$$R_3 = K_{r6} P_{O_2} \quad (15)$$

$$R_4 = K_{r7} P_{CO_2} \quad (16)$$

This approach was extended during the present study to include the reaction of carbon with  $H_2O$ , employing the results of Johnstone et al. [26]. The reaction rate expression in this case is

$$R_5 = K_{r8} P_{H_2O} / (1 + K_{r9} P_{H_2} + K_{r10} P_{H_2O}) \quad (17)$$

For this second approach, the total reaction rate of carbon was obtained as the sum of the rates for  $O_2$ ,  $CO_2$  and  $H_2O$ , ignoring potential interactions between reactants. This yields:

$$K = (r_p / \rho D) \sum_{i=3}^5 a_i R_i \quad (18)$$

The specific reaction rate parameters used in the computations are summarized in Table 2, where the  $K_{ri}$  are assumed to have the following general form:

$$K_{ri} = A_i T^{n_i} \exp(-E/RT) \quad (19)$$

In all cases,  $p_i$  was found from the mass fractions at the particle surface as follows:

$$p_i = M Y_i p / M_i \quad (20)$$

The  $a_i$  and  $\zeta$  were selected to fit the data as well as possible. Particular values of these parameters will be presented later. Given the gas-phase solution for a particular value of  $K$ , the  $Y_{ip}$  are found as described earlier. Equations (11)-(14) for the Neoh et al. [18] approximation, or Eqs. (15)-(17) for the extended Libby and Blake [17] approximation yield a prediction of  $K$ , which could then be iterated to find particle transport rates.

### 3.4 Particle-Life Histories

Given the temperature and size of the particle, and the ambient conditions, the gas phase and surface reaction analyses yield the  $\tilde{Y}_{ip}$ ,  $Y_{ip}$ ,  $K$  and  $q_c''$ . The variation of the size and temperature of the particle was determined by solving equations for conservation of particle mass and energy.

Table 2. Summary of Reaction Rate Parameters in  $K_{ri}$

i	A	n	E (kcal/gmol)
1 <sup>a</sup>	361 kg K <sup>1/2</sup> /m <sup>2</sup> s atm	-1/2	0
2	2400 kg/m <sup>2</sup> s atm	0	30.0
3	21.3 atm <sup>-1</sup>	0	- 4.1
4	0.535 kg/m <sup>2</sup> s atm	0	15.2
5	18.1 x 10 <sup>6</sup> kg/m <sup>2</sup> s	0	97.0
6	87100 kg/m <sup>2</sup> s atm	0	35.8
7	2470 kg/m <sup>2</sup> s atm	0	41.9
8 <sup>b</sup>	15.15 x 10 <sup>-3</sup> kg/m <sup>2</sup> s atm	0	32.7
9	9.42 x 10 <sup>-11</sup> atm <sup>-1</sup>	0	-60.8
10	7.07 x 10 <sup>-16</sup> atm <sup>-1</sup>	0	-79.3

<sup>a</sup> Assuming a collision efficiency of 0.28.

<sup>b</sup> Assuming a surface area of reaction of 1.15 m<sup>2</sup>/g of carbon, which is the average surface area over the period of reaction.



Neglecting the relatively slow density variation of the particle, conservation of particle mass yields:

$$\frac{d r_p}{dt} = -\rho_p D K / \rho_p r_p \quad (21)$$

where  $\rho_p$  is found from Eq. (1)

Conservation of energy at the particle surface yields:

$$\frac{d T_p}{dt} = \left( \frac{-3}{\rho_p C_{p_p} r_p} \right) (\dot{m}_p'' (i_p - i_c) + q_c'' + q_r'') \quad (22)$$

where  $q_r''$  is the particle surface heat flux for radiation to the enclosure surrounding the flow:

$$q_r'' = \sigma \epsilon_p (T_p^4 - T_w^4) \quad (23)$$

The initial conditions for Eqs. (21) and (22) were based on conditions at the end of the particle injection tube. At this point, all the carbon initially in the slurry was present in the agglomerate and the agglomerate density and temperature are known.

Equations (21) and (22) were numerically integrated on the computer, using Gear's method. The nonlinear algebraic set of equations which must be satisfied in order to determine the  $\tilde{Y}_{i_p}$ ,  $Y_{i_p}$ ,  $q_c''$  and  $K$ , were solved using the Newton-Raphson method, given the current values of  $T_p$ ,  $r_p$  and the ambient conditions.

Measured particle and gas velocities were used during these computations. Residence time, position and velocity of the particles were related by integrating

$$\frac{dx_p}{dt} = u_p \quad (24)$$

#### 4. Results and Discussion

##### 4.1 Agglomerates of Monodisperse Carbon Blacks

###### 4.1.1 Appearance

The appearance of the carbon agglomerates varied with extent of reaction, but was relatively independent of flame conditions or ultimate carbon particle size in the slurry. Therefore, the SEM photographs in Fig. 4, for  $d_u = 300$  nm, are representative of the appearance of agglomerates at and near the start of reaction. Similar SEM photographs of particles when the extent of reaction is nearly unity appear in Fig. 6. Comparing all four photographs indicates that the pore structure continues to develop throughout reaction, eventually reaching the center of the particle. Near the end of reaction, the pore structure develops to the point where the particle has a lacey structure, with an apparent density near zero, but with a substantial diameter. This behavior is reflected by the density correlation of Eq. (1).

Similar to agglomerate appearance, density was primarily a function of extent of reaction. Results for agglomerates where  $d_u = 300$  nm for a wide range of flame conditions have already been presented in Fig. 5. Similar measurements for various  $d_u$  are illustrated in Fig. 7, along with the correlation of Eq. (1). These findings show that Eq. (1) provides an adequate representation of agglomerate density for monodisperse carbon-blacks having  $d_u$  in the range 70-300 nm.

###### 4.1.2 Empirical Parameters

The pore structure enhances convective transport since the ambient gas can percolate through the porous particle. Transport enhancement factors found from present data for  $d_u = 300$  nm are illustrated in Fig. 8. Results from the large-particle tests (400-1000  $\mu$ m agglomerates),

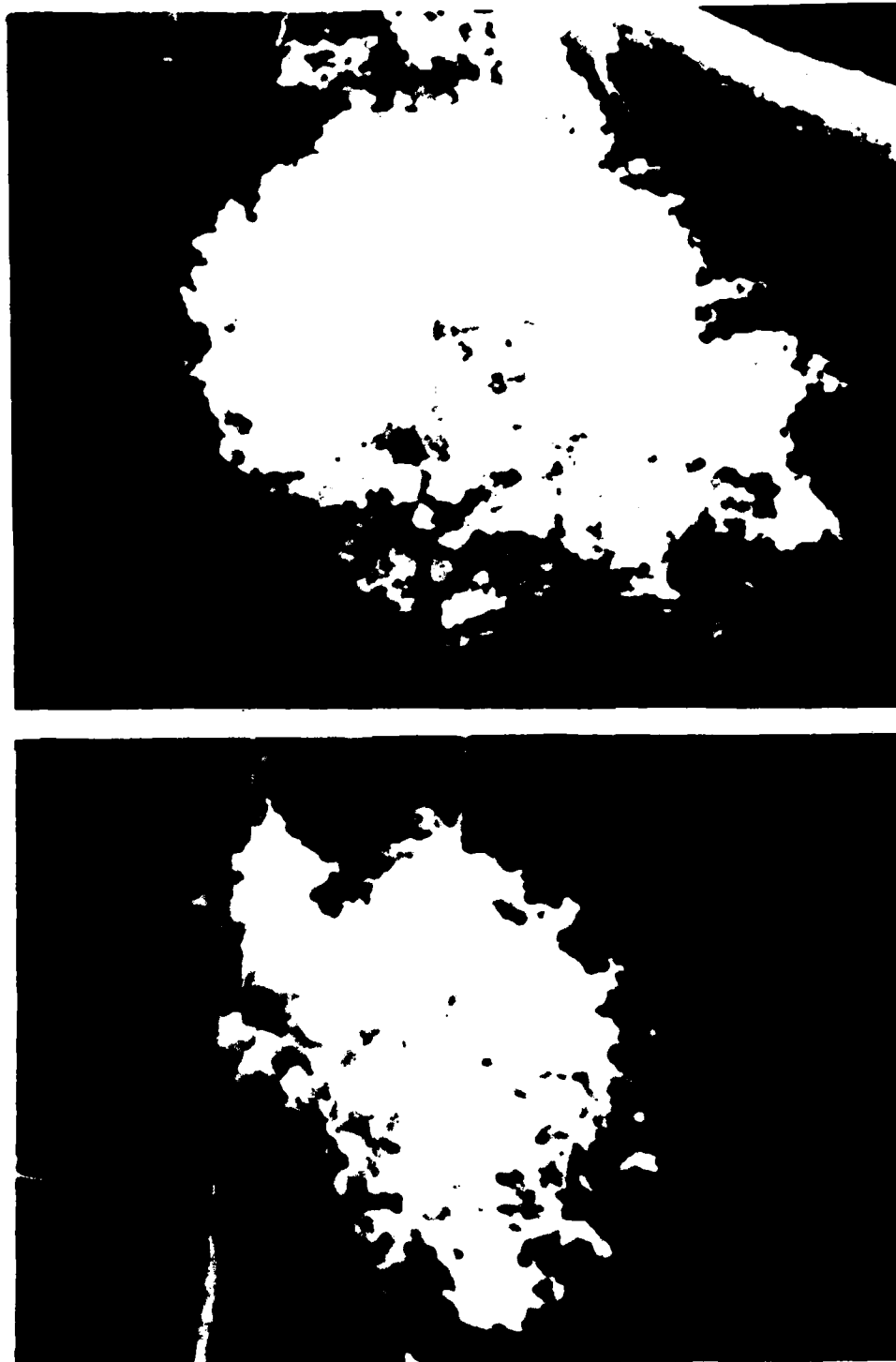
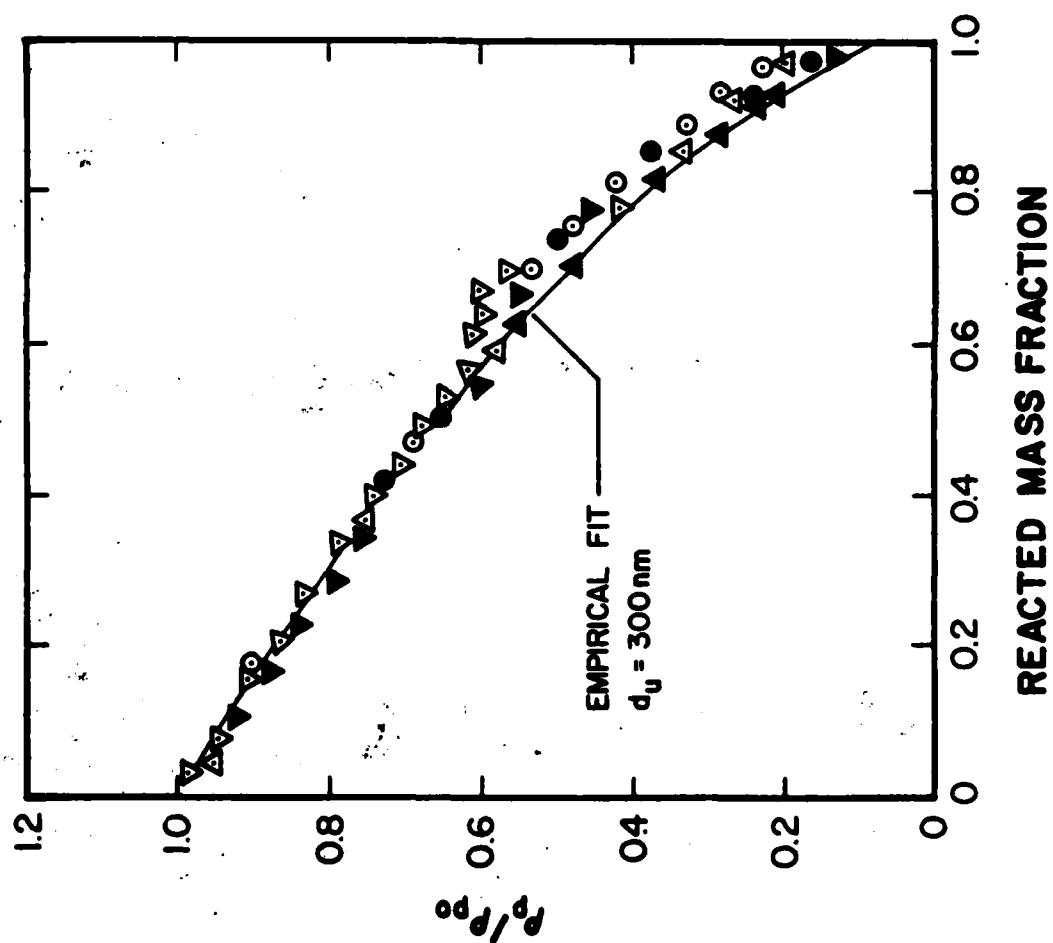


Figure 6. SEM photographs of collected particles:  $\phi = 1$ ,  $T_f = 1683$  K,  $d_{po} = 73.4$   $\mu\text{m}$ . Upper and lower photographs have reacted mass fractions of 0.902 and 0.999 and  $d_u = 300$  nm.



$\phi$	$T_f$ (K)	$d_u$ (nm)
○	0.6	1663 150
●	0.6	1663 70
△	0.6	1953 150
▲	0.6	1953 70
▽	1.0	1683 150
▼	1.0	1683 70

$d_{p0} = 73.4 \mu\text{m}$

Figure 7. Apparent particle density as a function of reacted mass fraction for various  $d_u$ .

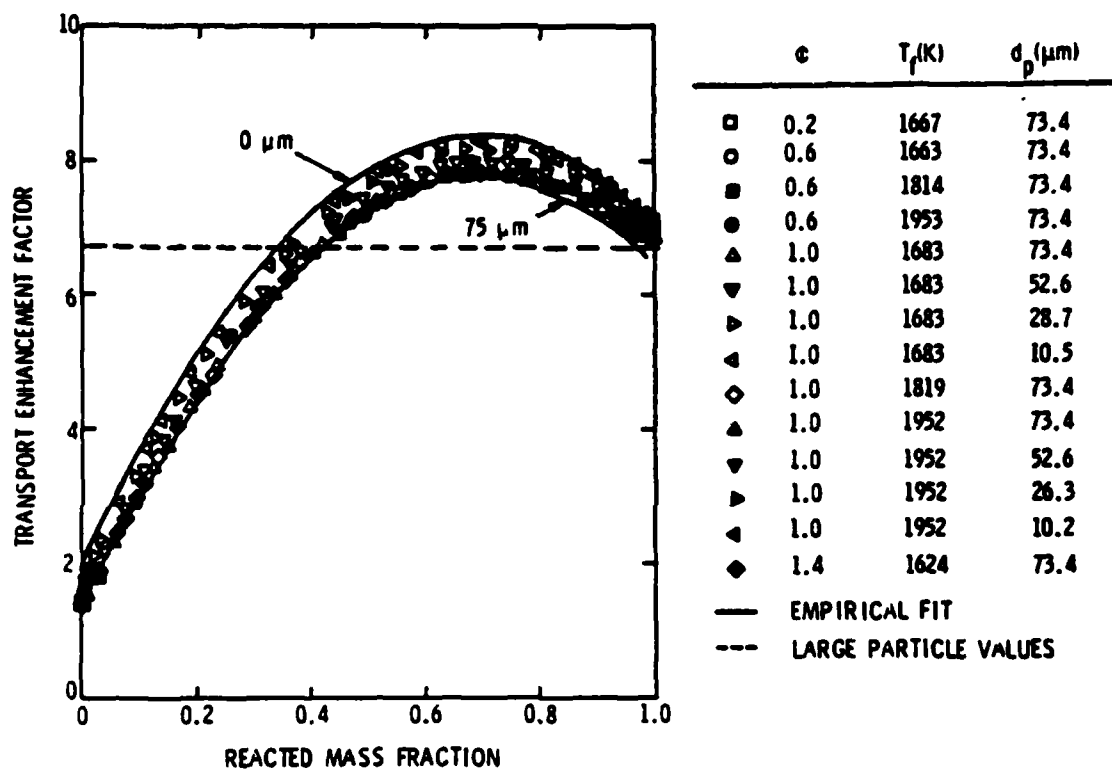


Figure 8. Transport-enhancement factor as a function of reacted mass fraction for  $d_u = 300$  nm.

for the same  $d_u$ , are also shown on the figure. This value was taken to be constant due to insufficient data. Present tests considered particles in the range 0-75  $\mu\text{m}$ .

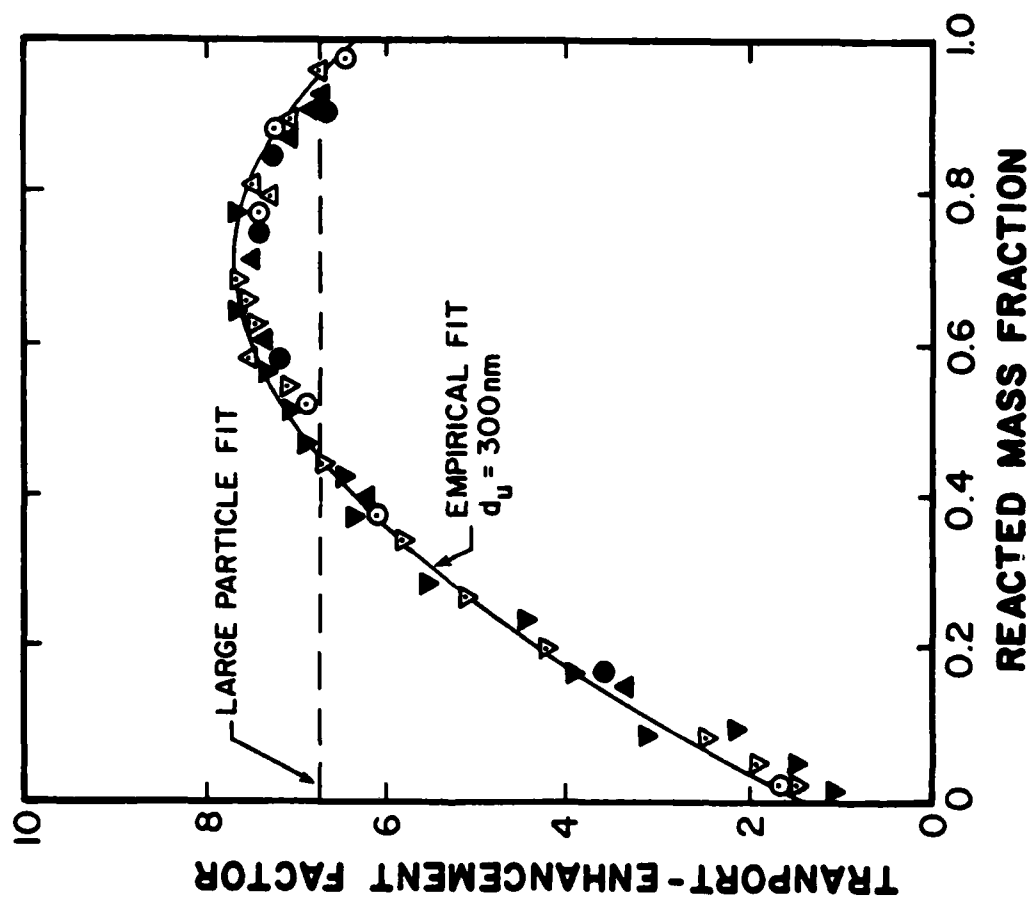
Similar to the large-particle tests, both energy and mass transport-enhancement factors were identical. At the start of reaction, the particles are relatively smooth and the transport-enhancement factor is nearly unity. As reaction proceeds, however, the pore structure develops and the transport enhancement factor increases. The final reduction in  $\zeta$  is associated with the pore zone reaching the center of the particle. For  $\epsilon > 20\%$ ,  $\zeta$  is within  $\pm 20\%$  of the value found earlier for large particles [6,7], where effects of  $\epsilon$  were not resolved. This supports the conclusion that the effect of agglomerate size on  $\zeta$  is not large.

Measurements of transport enhancement factors for carbon-blacks with  $d_u$  in the range 70-300  $\mu\text{m}$  are illustrated in Fig. 9 for various flame conditions.\* These results indicate that effects of  $d_u$  on  $\zeta$  are not large for this range of ultimate carbon particle sizes.

Area/reactivity factors ( $a_1$ ) for the  $\text{O}_2\text{-CO}_2\text{-H}_2\text{O}$  reaction mechanism are illustrated in Fig. 10 for  $d_u = 300 \text{ nm}$ . The results are plotted as a function of reacted mass fraction for various flame conditions and initial agglomerate diameters. The results found for large supported agglomerates are also shown on the figure [6,7], although effects of  $\epsilon$  were not resolved for this data. The  $a_1$  exhibit less variation with  $\epsilon$  than  $\zeta$ , indicating that microroughness which provides reaction surface is less influenced by the development of pores. However, the  $a_1$  do increase somewhat as the pore structure develops. Present values of the  $a_1$  are comparable to the large particle values. The greatest discrepancy between the present

---

\* Results for  $d_u = 300 \text{ nm}$  are presented as a data correlation.



$\phi$	$T_f$ (K)	$d_u$ (nm)
○	0.6	1663
●	0.6	1663
△	0.6	1953
▲	0.6	1953
▽	1.0	1683
▼	1.0	1683
		150
		70
		150
		70

$d_{p0} = 73.4 \mu\text{m}$

Figure 9. Transport-enhancement factor as a function of reacted mass fraction for various  $d_u$ .

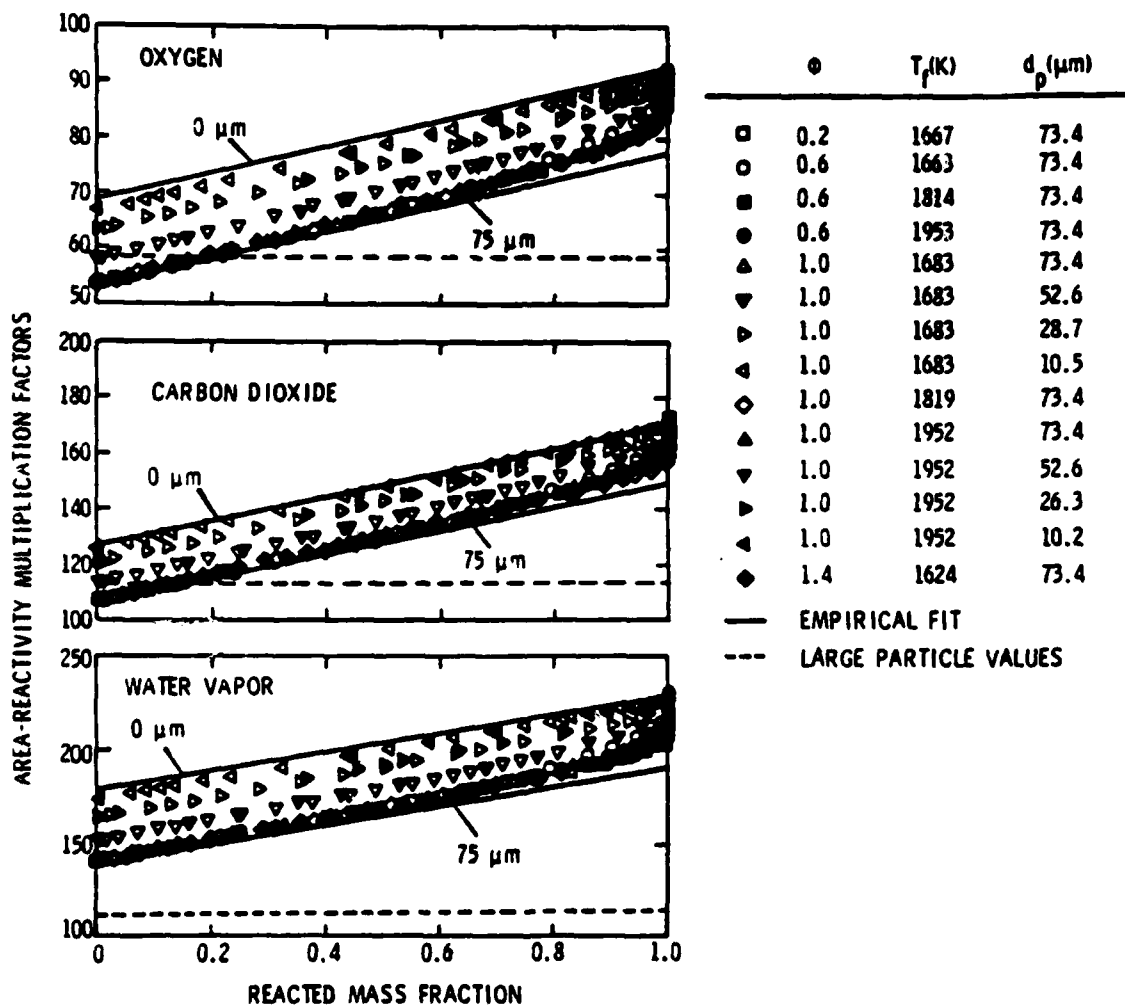


Figure 10. Area/reactivity multiplication factors for the  $\text{O}_2\text{-CO}_2\text{-H}_2\text{O}$  reaction mechanism for  $d_u = 300 \text{ nm}$ .



measurements and Refs. 6 and 7 appears for  $a_{H_2O}$ . This difference is not significant, however, since  $a_{H_2O}$  was arbitrarily set equal to  $a_{CO_2}$  during the earlier work, since C/H ratios were not varied during these tests. The present measurements for various C/H ratios indicate the  $a_{H_2O}$  should be somewhat greater than  $a_{CO_2}$ .

The effect of ultimate carbon particle size on the  $a_1$  for the  $O_2$ - $CO_2$ - $H_2O$  reaction mechanism is illustrated in Fig. 11. Decreasing  $d_u$  causes a progressive increase in the  $a_1$ , for all values of  $\epsilon$ . This trend is reasonable, since smaller ultimate carbon particle sizes should yield higher reactive surface areas per unit volume.

The  $a_1$  for the  $OH$ - $O_2$  reaction mechanism are illustrated in Fig. 12 for  $d_u = 300$  nm. The large particle values for the same  $d_u$  are also shown on the figure. The  $a_1$  are also relatively independent of flame conditions in the case, tending to increase with increasing  $\epsilon$  and decreasing  $d_{po}$ . The present values are within 20% of the values found earlier for large particles--where effects of  $\epsilon$  were not resolved.

The effect of  $d_u$  on the  $a_1$  for the  $OH$ - $O_2$  reaction mechanism is illustrated in Figure 13. Similar to the  $O_2$ - $CO_2$ - $H_2O$  mechanism, the  $a_1$  progressively increase as the ultimate carbon particle size decreases.

Agglomerate densities,  $\zeta$  and the  $a_1$  were correlated as functions of  $\epsilon$ ,  $d_{po}$  and  $d_u$  over the present test range. Since effects of flame conditions were small, they were ignored in the correlations. These correlations are summarized in Table 3. Effects of  $d_p$  and  $d_u$ , while measurable, are not large. Except for particle density, the effect of  $\epsilon$  is also not large for  $\epsilon > 0.20$ . Therefore, mean values of  $\zeta$  and the  $a_1$  are also summarized in Table 3 for the present data, along with mean values found earlier for large particles. The values of the two sets of measurements are not much

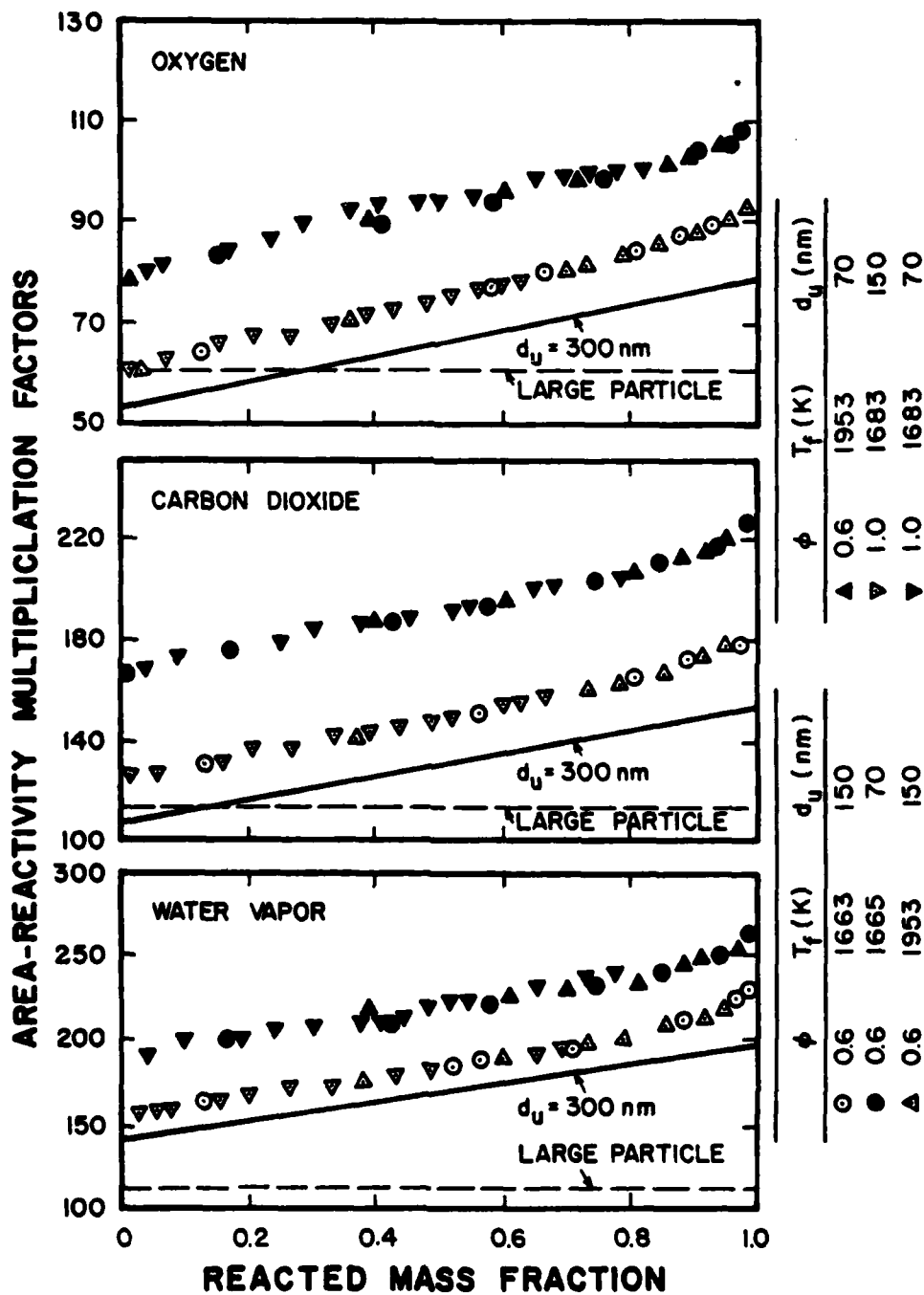


Figure 11. Area/reactivity multiplication factors for the  $O_2$ - $CO_2$ - $H_2O$  reaction mechanism for various  $d_u$ .

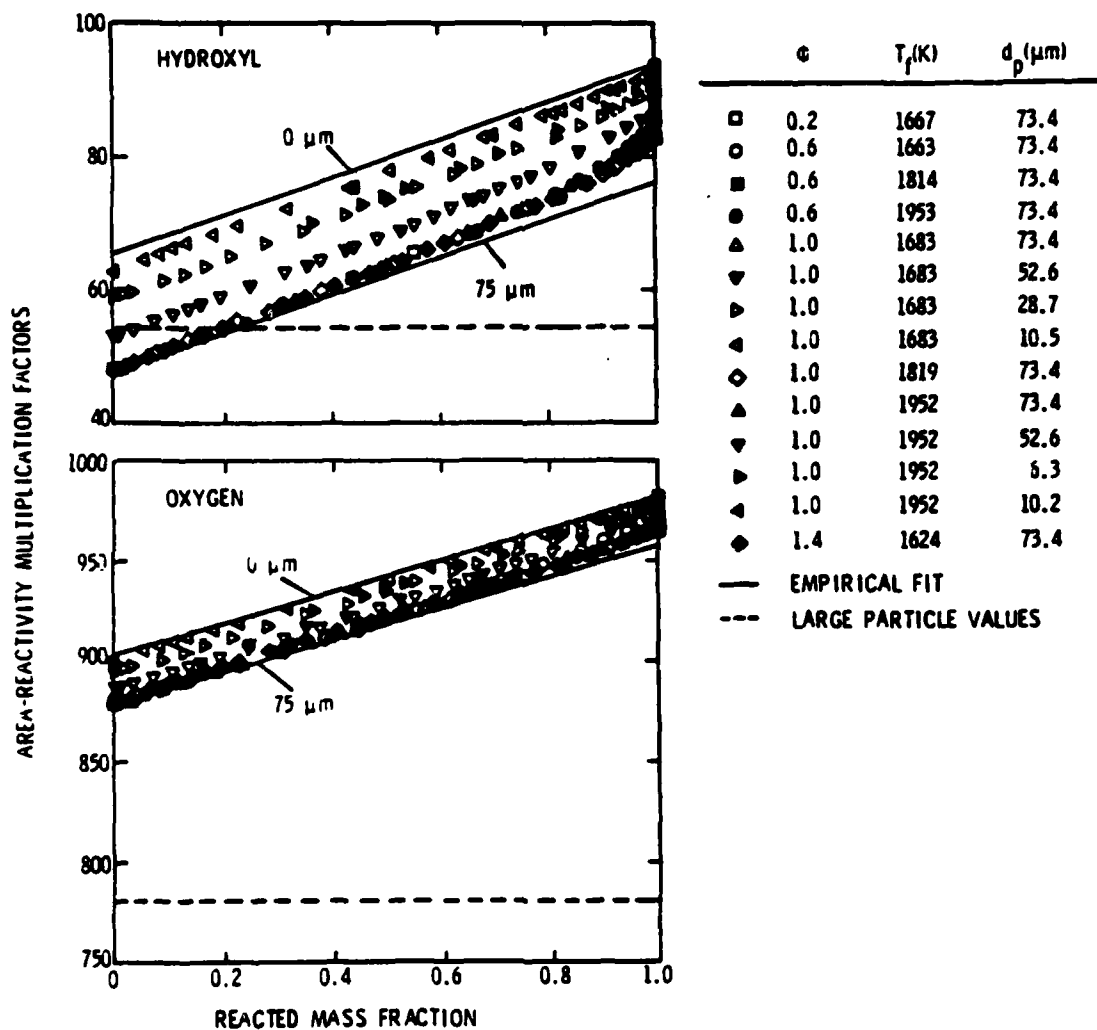


Figure 12. Area/reactivity multiplication factors for the OH-O<sub>2</sub> reaction mechanism for  $d_u = 300$  nm.



Table 3 Summary of Agglomerate Structure Parameters (Monodisperse Carbon-Black)<sup>a</sup>

Factor	Small Particles <sup>b</sup>		Large Particles <sup>c</sup>	
	Correlation ( $d_{po}$ and $d_u$ in $\mu m$ )	Mean Value	Mean Value	
$\rho_p^d$	$\rho_{po} (1 - \epsilon)^{0.6}$	--	1820	
$\zeta$	$1.49 - 0.00858 d_{po} + 18.3 \epsilon - 13.2 \epsilon^2 - 1.77 d_u$	7.5	6.7	
Neoh et al. Mechanism:				
$a_{OH}$	$56.8 - 0.234 d_{po} + 28.2 \epsilon + 2.55/d_u$	82.5	54.3	
$a_{O_2}$	$776.2 - 0.307 d_{po} + 79.3 \epsilon + 37.8/d_u$	963.0	758.0	
Extended Libby and Blake Mechanism:				
$a_{O_2}$	$61.3 - 0.206 d_{po} + 23.7 \epsilon + 2.27/d_u$	82.9	58.2	
$a_{CO_2}$	$109.6 - 0.290 d_{po} + 43.2 \epsilon + 5.56/d_u$	156.8	112.9	
$a_{H_2O}$	$164.7 - 0.513 d_{po} + 50.1 \epsilon + 4.21/d_u$	205.7	112.9	

<sup>a</sup> All for MT carbon black described in Table 1.

<sup>b</sup> Present study, 0-75  $\mu m$  diameter free particles, particle Reynolds numbers of 0-0.35,  $d_u = 70-300$  nm.

<sup>c</sup> Szekeley and Faeth [6,7], 400-1000  $\mu m$  diameter supported particles, particle Reynolds numbers of 10-200,  $d_u = 300$  nm. No variation of parameters was found in this case due to insufficient data.

<sup>d</sup> Initial densities are 1820 ( $d_u = 300$  nm), 1859 ( $d_u = 150$  nm) and 1933 ( $d_u = 70$  nm)---all in  $kg/m^3$ .

different, supporting the conclusion that the effect of  $d_u$  and  $d_p$  on reaction rates is relatively small for carbon black agglomerates. The  $a_1$  are all on the order of 100, which is reasonable in view of the large pore area per unit surface area seen in Figs. 4 and 6.

#### 4.1.3 Burning Rates

In the following, we examine the properties of agglomerate burning rates as a function of flame condition, agglomerate diameter and ultimate carbon particle size. The data are summarized in Appendix A. Predictions employ the empirical parameters summarized in Table 3.

Predicted and measured burning rates for agglomerates having  $d_u = 300$  nm are illustrated in Figs. 14-18. In these figures particle burning rate (based on rate of change of the particle diameter with time) is plotted as a function of particle diameter with either flame temperature, equivalence ratio or initial particle diameter taken as a parameter. For these tests, the burning rate based on particle diameter had an estimated error of less than 15% for a 75  $\mu$ m particle and less than 30% for a 2  $\mu$ m particle. Three sets of predictions are shown using the OH-O<sub>2</sub> and O<sub>2</sub>-CO<sub>2</sub>-H<sub>2</sub>O reaction models with the complete correlations for empirical parameters given in Table 3, as well as the latter correlation with the constant average values of empirical parameters given in Table 3.

Predictions for either reaction mechanism, using complete correlations of empirical parameters, are in reasonably good agreement with each other and with the data in Figs. 14-18. Maximum discrepancies are on the order of 20%. Predictions using constant average values of the empirical parameters are only slightly less satisfactory. This is partly expected since the parameters were selected to fit the data, however, it is most

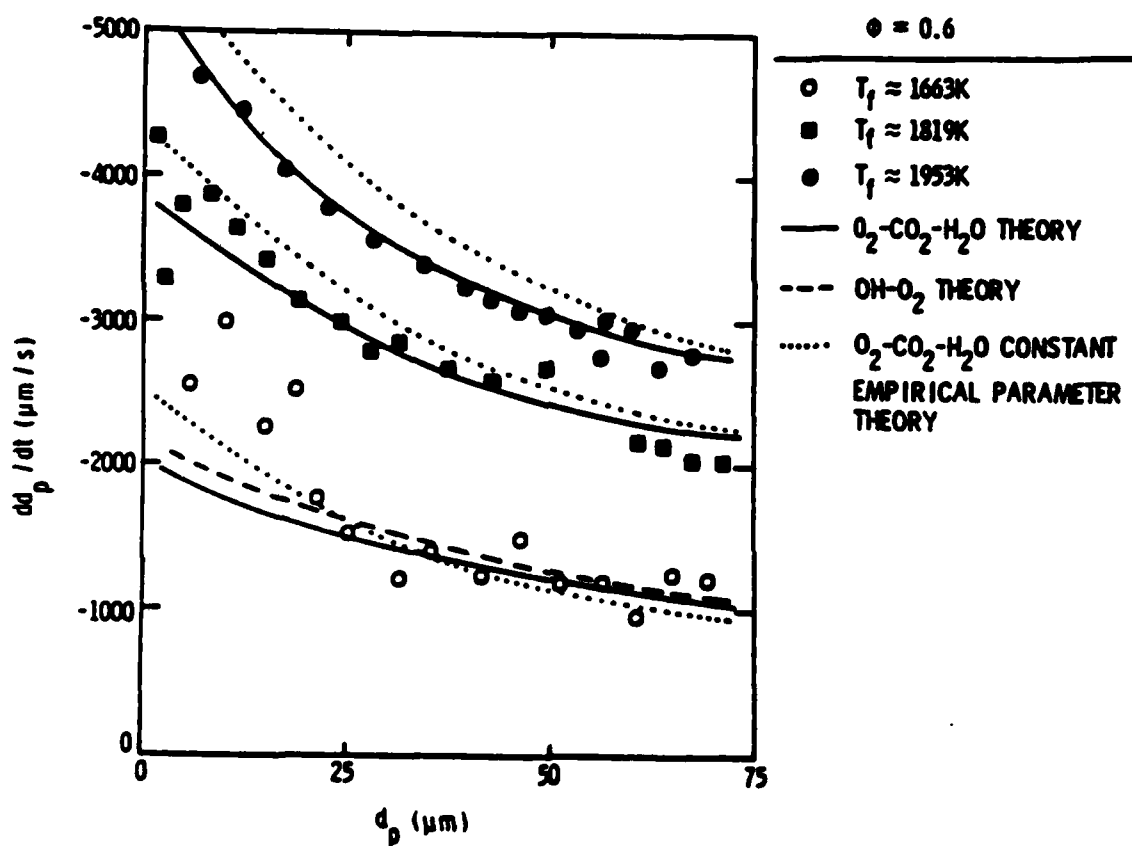


Figure 14. Variation of burning rate with particle diameter and temperature for  $\phi = 0.6$  and  $d_u = 300 \text{ nm}$ .

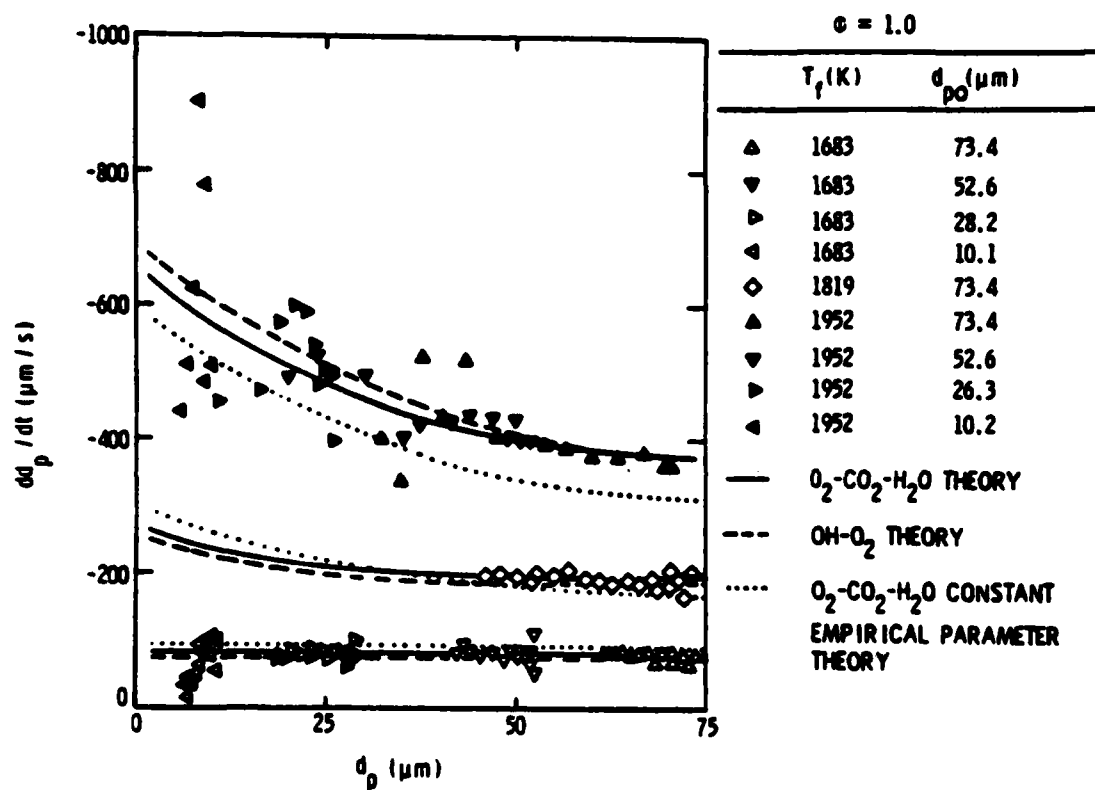


Figure 15. Variation of burning rate with particle diameter and temperature for  $\phi = 1.0$  and  $d_u = 300$  nm.



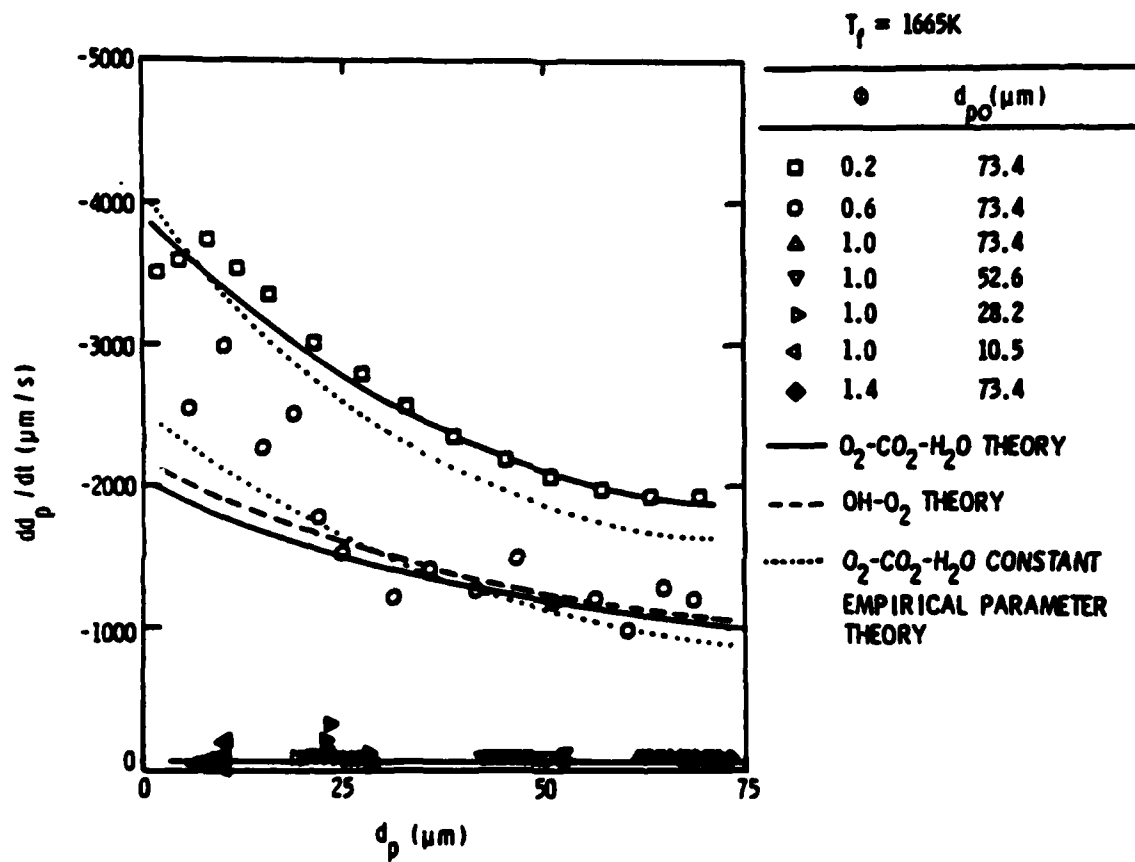


Figure 16. Variation of burning rate with particle diameter and equivalence ratio for  $T_f = 1665 K$  and  $d_u = 300 nm$ .

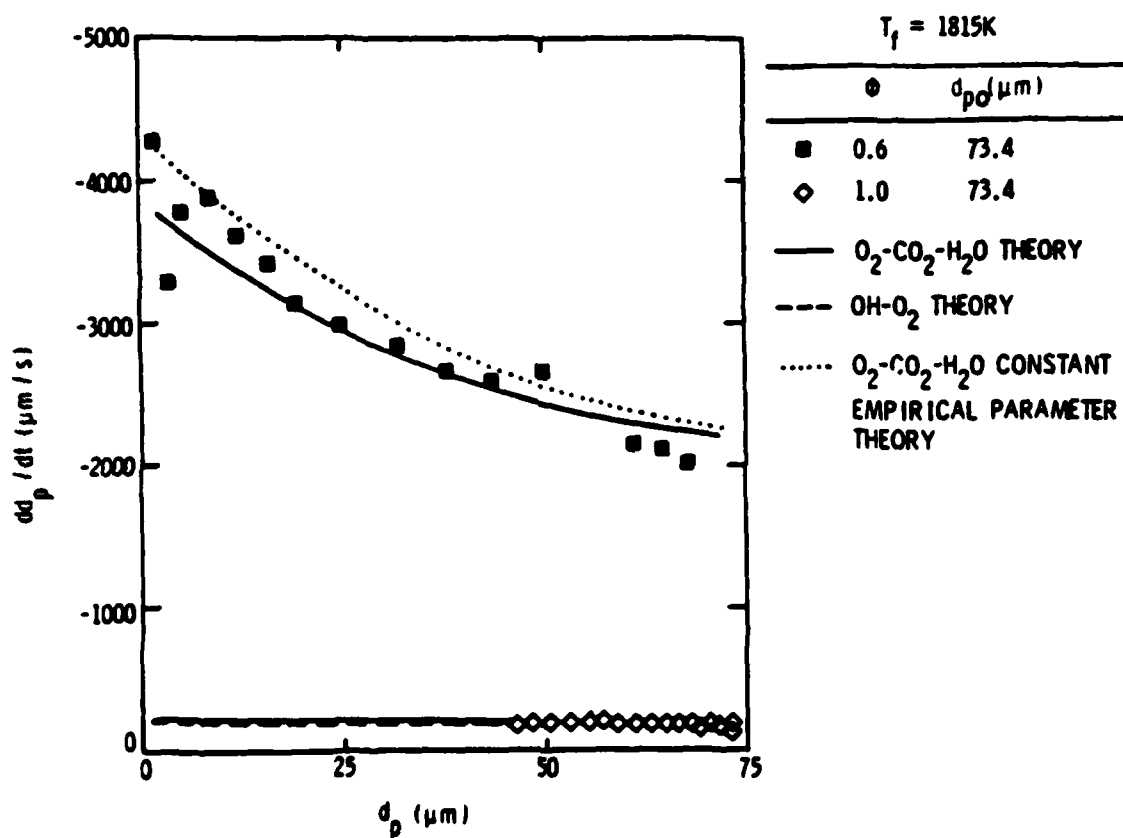


Figure 17. Variation of burning rate with particle diameter and equivalence ratio for  $T_f = 1815 K$  and  $d_u = 300 nm$ .

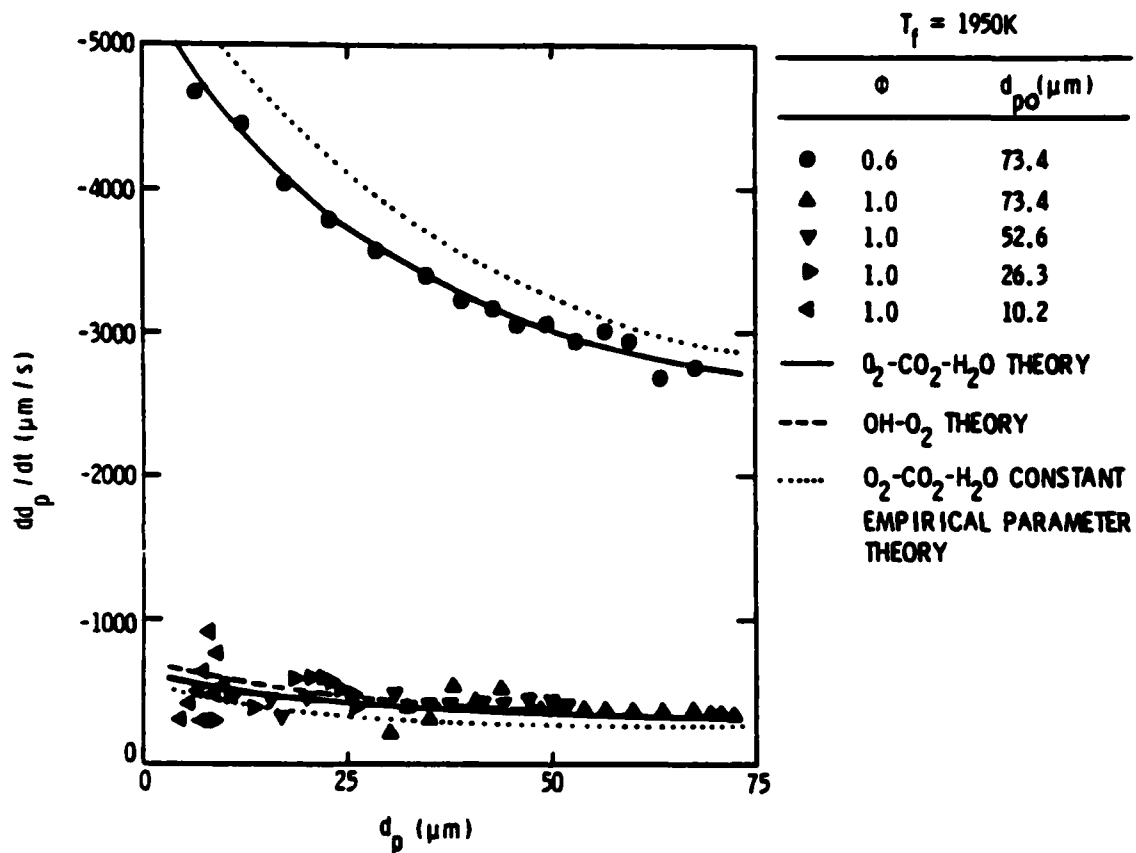


Figure 18. Variation of burning rate with particle diameter and equivalence ratio for  $T_f = 1950\text{ K}$  and  $d_u = 300\text{ mm}$ .

encouraging that the analysis can treat effects of flame conditions and particle size with this single set of parameters.

Agglomerate burning rates are independent of diameter under kinetic-controlled conditions, where reaction rates are low in comparison to rates of mass diffusion. For diffusion-controlled conditions, where reaction rates are high in comparison to diffusion rates, the burning rate is inversely proportional to  $d_p^{(0.5 \text{ to } 1.0)}$ , where the higher power is more representative of present tests at relatively low Reynolds numbers [6,7]. The results at high equivalence ratios, in Figs. 15-18, approach kinetic-controlled conditions--only tending toward diffusion control at the highest temperatures. The low equivalence ratio results of Fig. 14 approach diffusion control--except at the lowest flame temperatures. In all cases, the process tends toward kinetic-control for the smallest agglomerate diameters, since small particles provide little resistance to convective heat and mass transfer. The very high burning rate at  $\phi = 0.2$  in Fig. 16 is somewhat misleading, since it is difficult to approach this temperature level with a conventional adiabatic flame, e.g.,  $\phi = 0.2$  was a quenching condition for the adiabatic flame tests Refs. 6 and 7.

Burning rate results for agglomerates having  $d_u = 70$  and  $150$  nm were generally similar to the findings pictured in Figs. 14-18. As  $d_u$  is reduced,  $\zeta$  increases slightly while the  $a_i$  generally increase. The net effect is a slight increase in burning rates near diffusion-controlled conditions and a slight increase in burning rates near kinetic-controlled conditions. These trends are reasonable, since smaller ultimate particle sizes are likely to modify the effective roughness of the surface, which causes variations in transport enhancement, while increasing the reaction

area per unit volume causing the  $a_1$  to increase. Based on this observation, it seems likely that a pore model could be constructed to predict such trends from the fundamental properties of the slurry formulation.

#### 4.1.4 Life Histories

A more complete picture of the combustion properties of carbon-black agglomerates can be seen from predicted and measured agglomerate-life histories. Results along these lines will be considered in some detail, since they provide a stringent test of the model as well as a survey of effects of particle size and flame conditions on particle lifetime. Naturally, these results are not completely indicative of agglomerate behavior in an actual combustor. Under combustor conditions, ambient properties of the particles change continuously, while present tests involved a fixed ambient environment.

Measured agglomerate-life histories for  $d_u = 300$  nm are illustrated in Figs. 19-32 for various initial agglomerate diameters and flame conditions. The data involves particle diameter and mass, normalized by their initial values, and particle temperature, normalized by the flame temperature, as a function of time after injection into the burner gas. Predictions for both reaction mechanisms are also shown on the figures, using the correlations for empirical parameters given in Table 3. Use of constant average empirical parameters is not considered here, since the high value of  $\zeta$ , representative of  $\epsilon > 0.20$ , tends to overestimate particle heat-up times.

The predictions of both reaction mechanisms and the measurements are in reasonably good agreement in Figs. 19-32. This is partly expected since the model involved correlation of burning rate measurements over the same

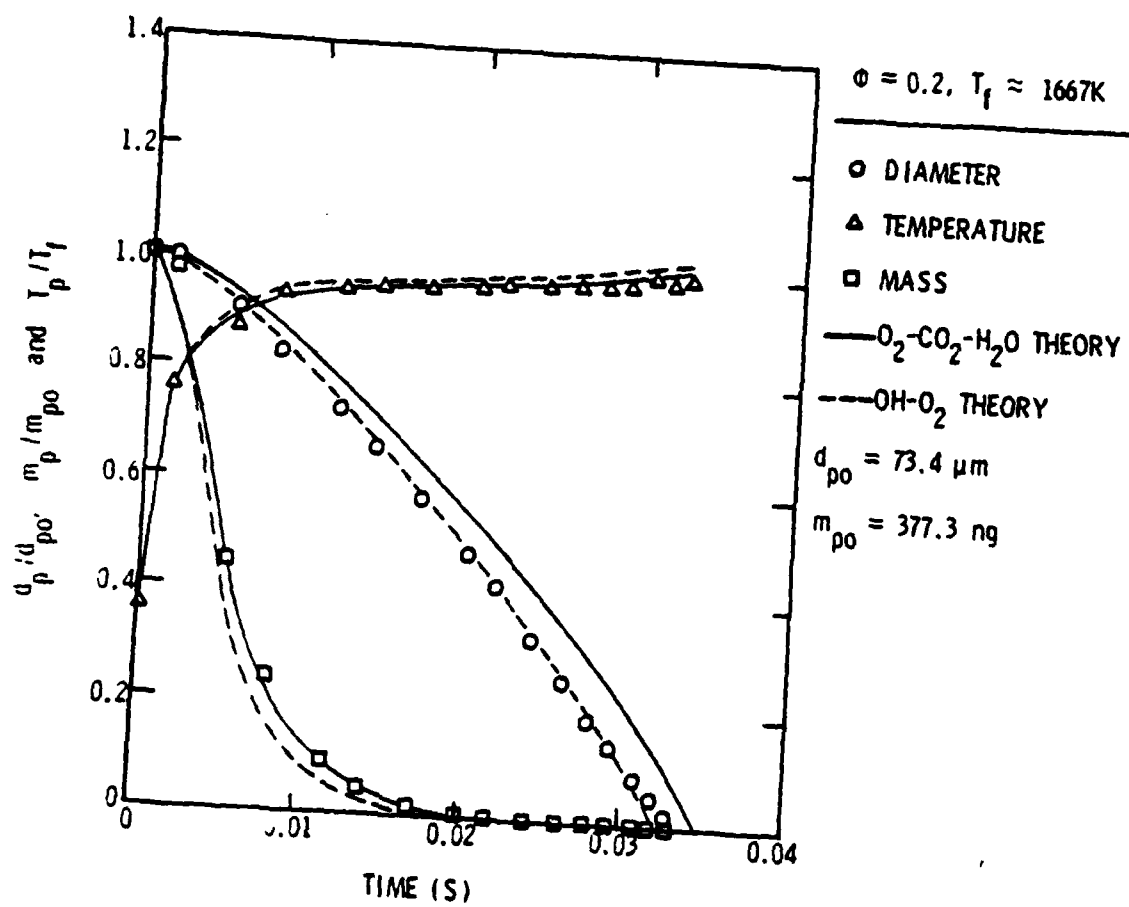


Figure 19. Particle-life history for  $\phi = 0.2$ ,  $T_f = 1667 K$ ,  $d_u = 300 nm$  and  $d_{po} = 73.4 \mu m$ .

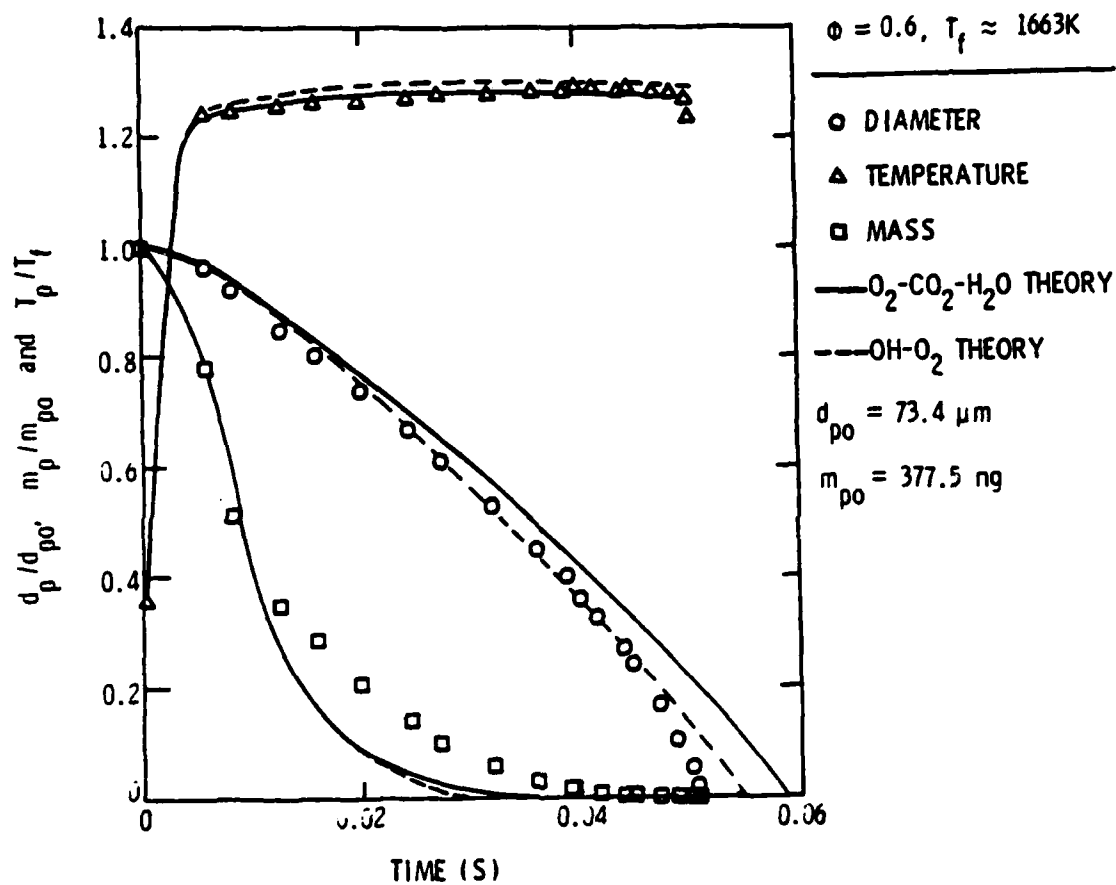


Figure 20. Particle-life history for  $\phi = 0.6$ ,  $T_f = 1663 K$ ,  $d_u = 300 nm$  and  $d_{po} = 73.4 \mu m$ .

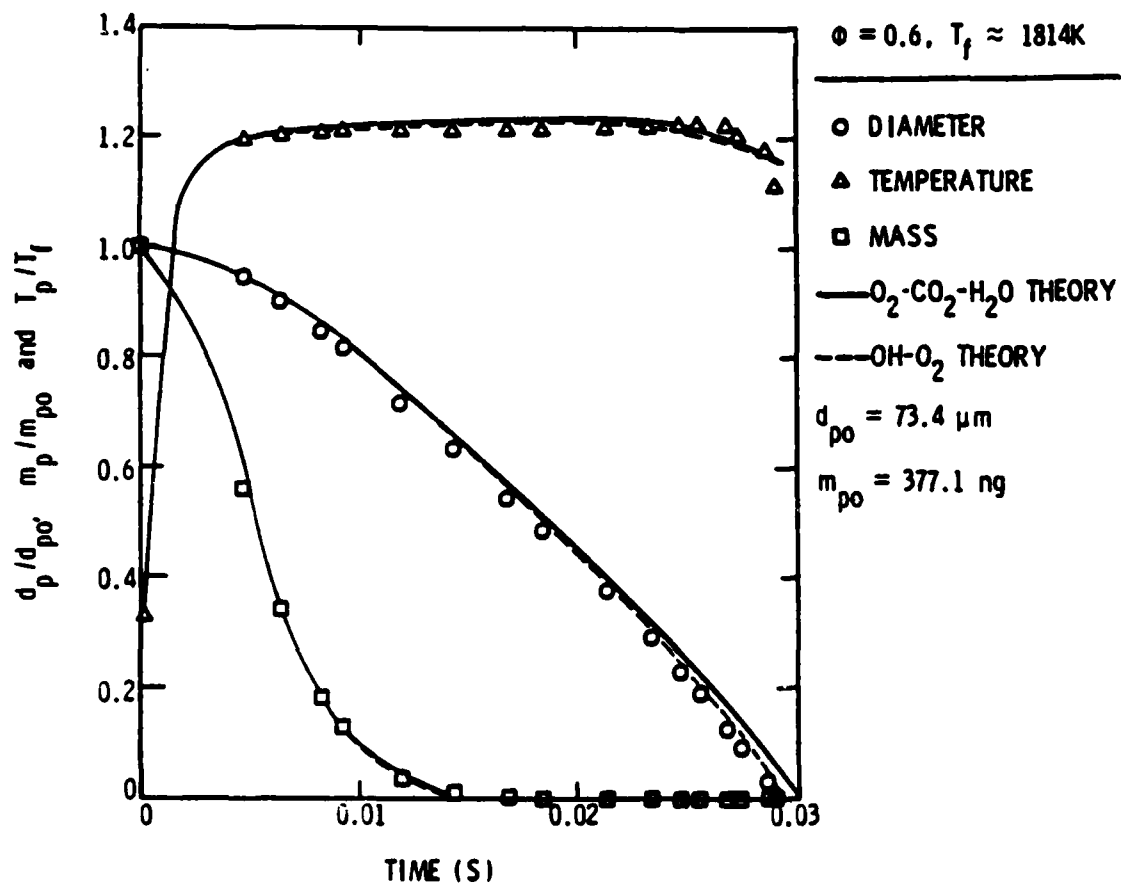


Figure 21. Particle-life history for  $\phi = 0.6$ ,  $T_f = 1814 \text{ K}$ ,  $d_u = 300 \text{ nm}$  and  $d_{po} = 73.4 \mu\text{m}$ .



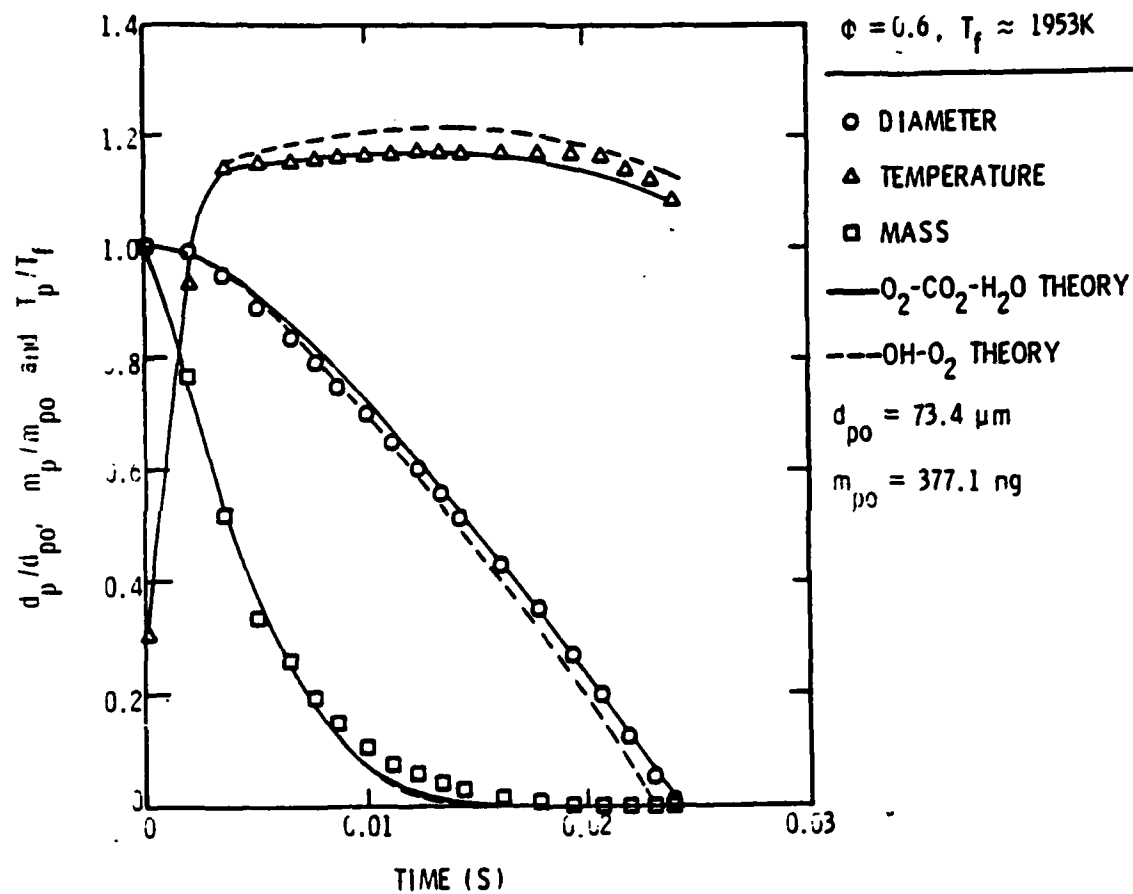


Figure 22. Particle-life history for  $\phi = 0.6$ ,  $T_f = 1953\text{ K}$ ,  $d_u = 300\text{ nm}$  and  $d_{po} = 73.4\text{ }\mu\text{m}$ .

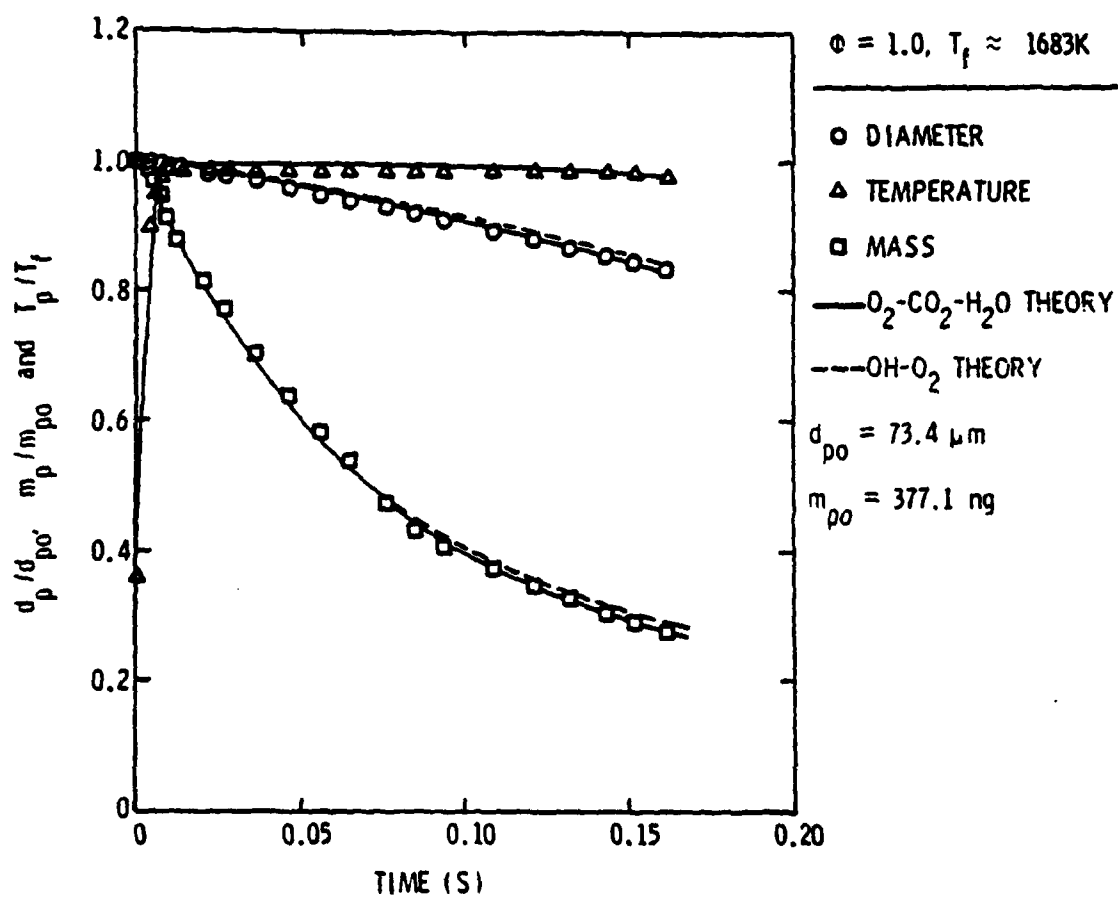


Figure 23. Particle-life history for  $\phi = 1.0$ ,  
 $T_f = 1683 K$ ,  $d_u = 300 nm$  and  $d_{po} = 73.4 \mu m$ .

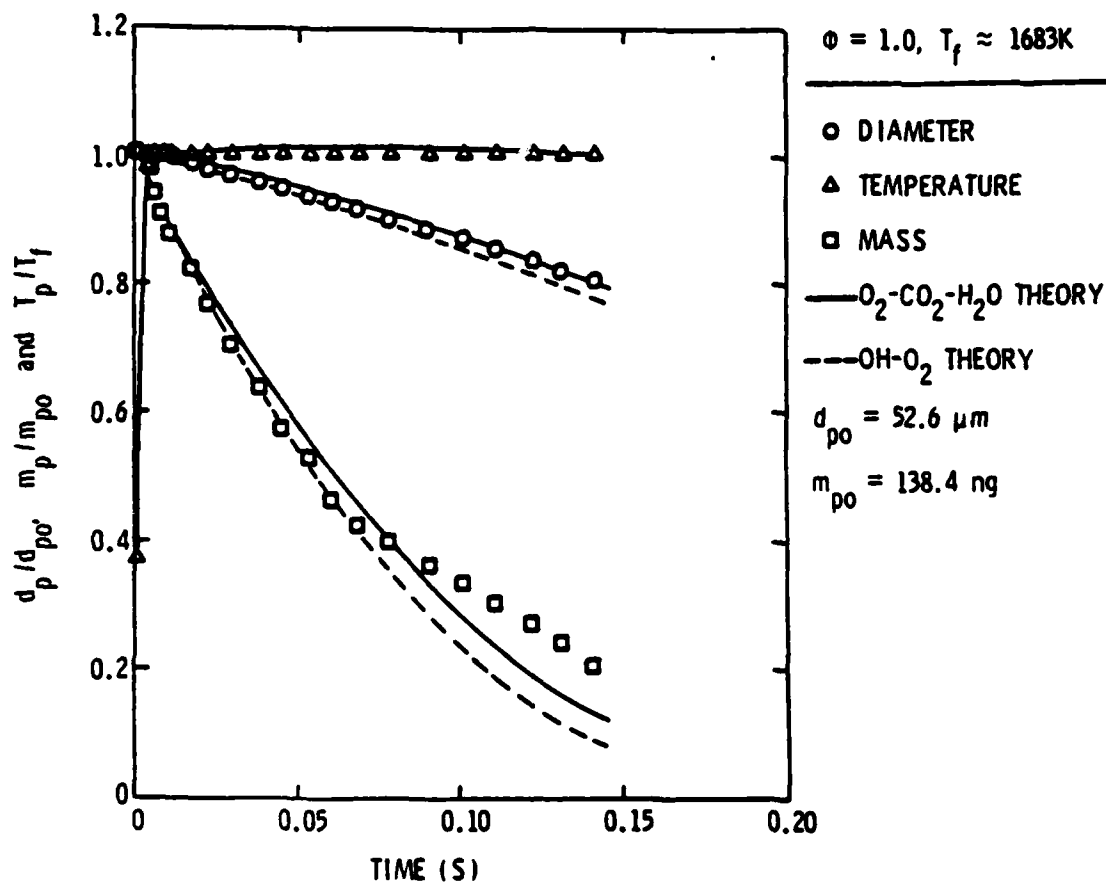


Figure 24. Particle-life history for  $\phi = 1.0$ ,  
 $T_f = 1683 K$ ,  $d_u = 300 nm$  and  $d_{po} = 52.6 \mu m$ .

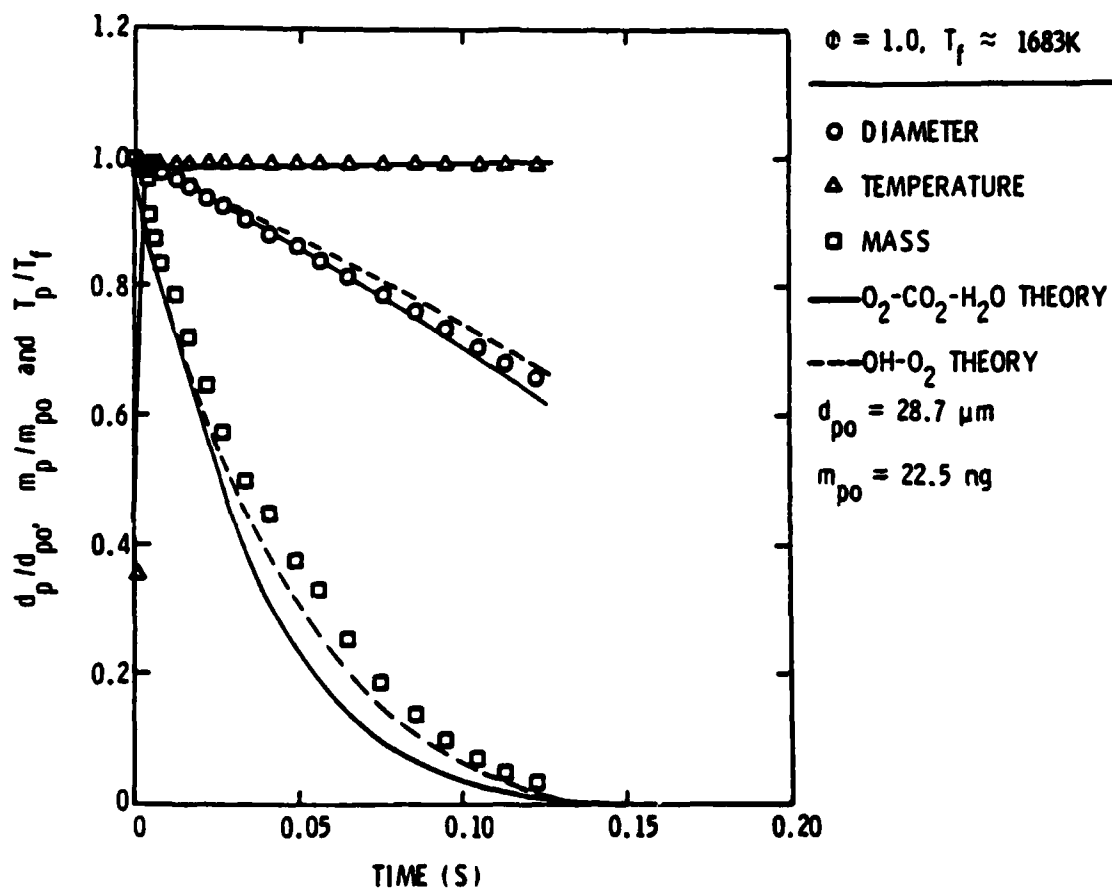


Figure 25. Particle-life history for  $\phi = 1.0$ ,  $T_f = 1683 \text{ K}$ ,  $d_u = 300 \text{ nm}$  and  $d_{po} = 28.7 \mu\text{m}$ .

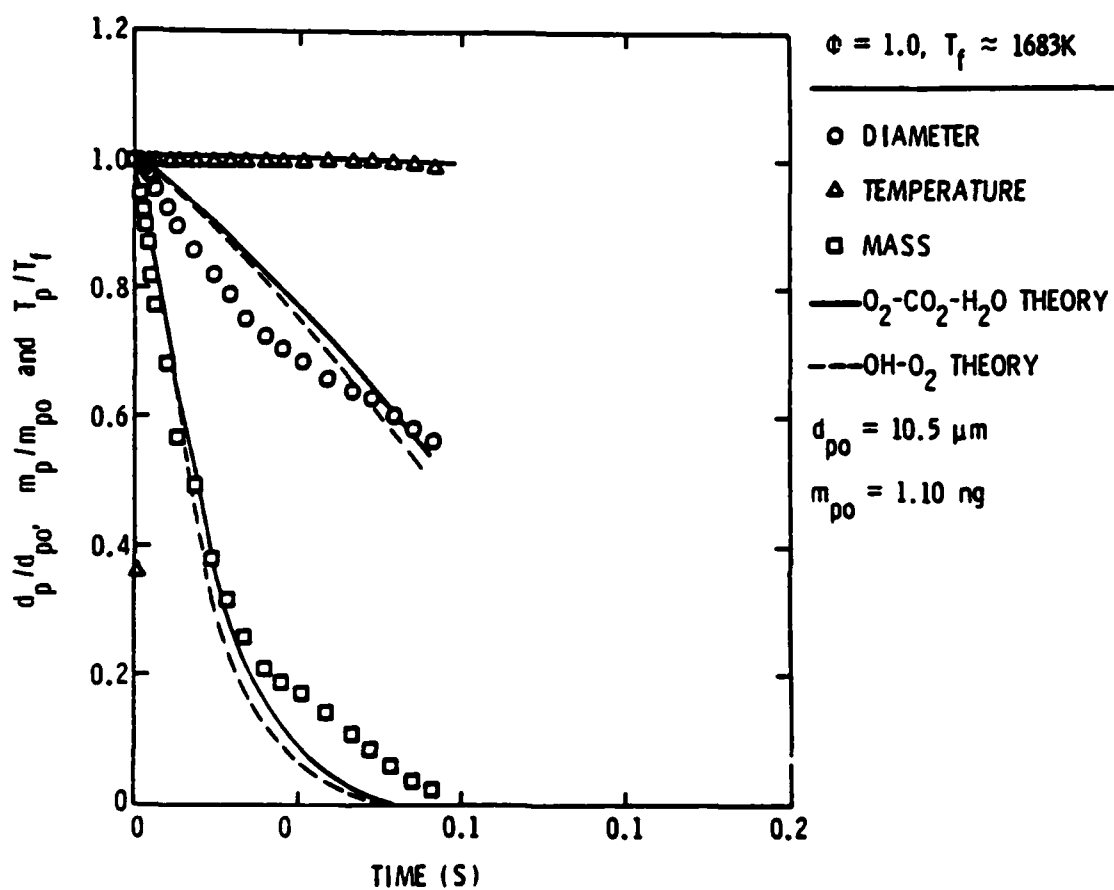


Figure 26. Particle-life history for  $\phi = 1.0$ ,  $T_f = 1683 \text{ K}$ ,  $d_u = 300 \text{ nm}$  and  $d_{po} = 10.5 \mu\text{m}$ .

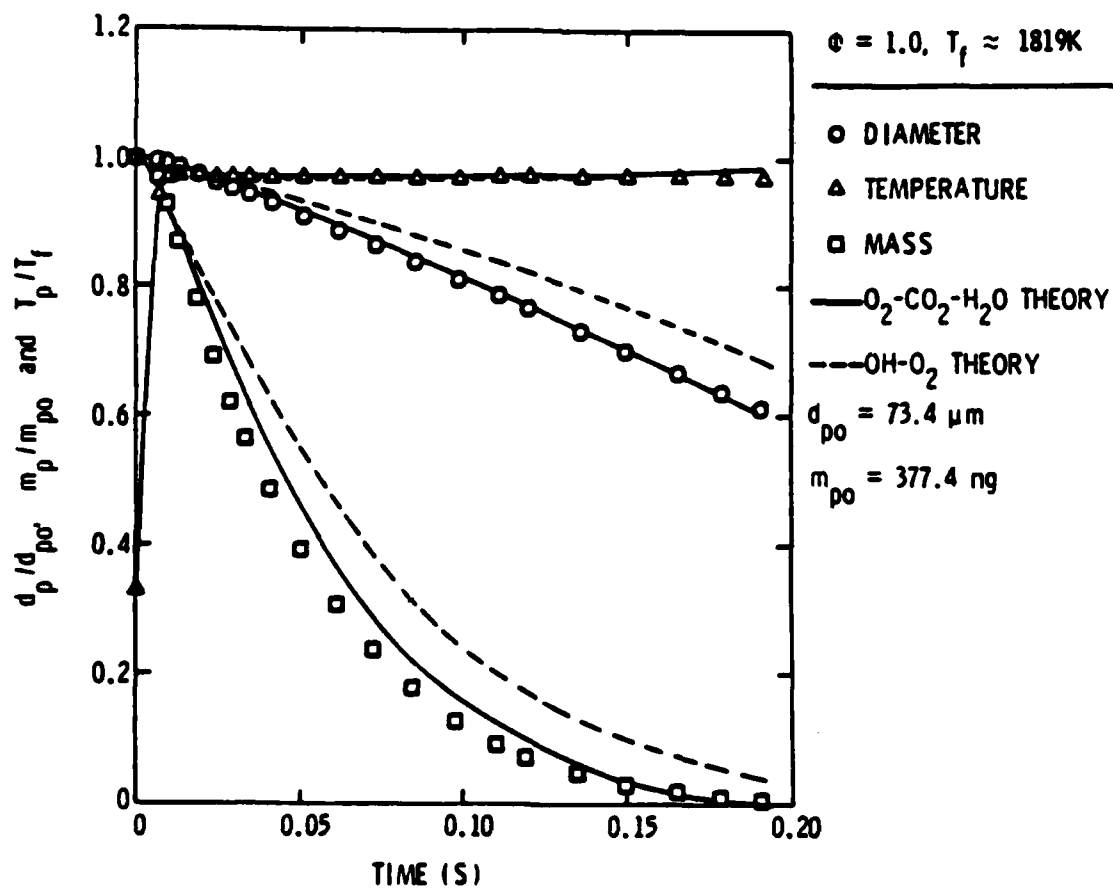


Figure 27. Particle-life history for  $\phi = 1.0$ ,  $T_f = 1819 K$ ,  $d_u = 300 nm$  and  $d_{po} = 73.4 \mu m$ .

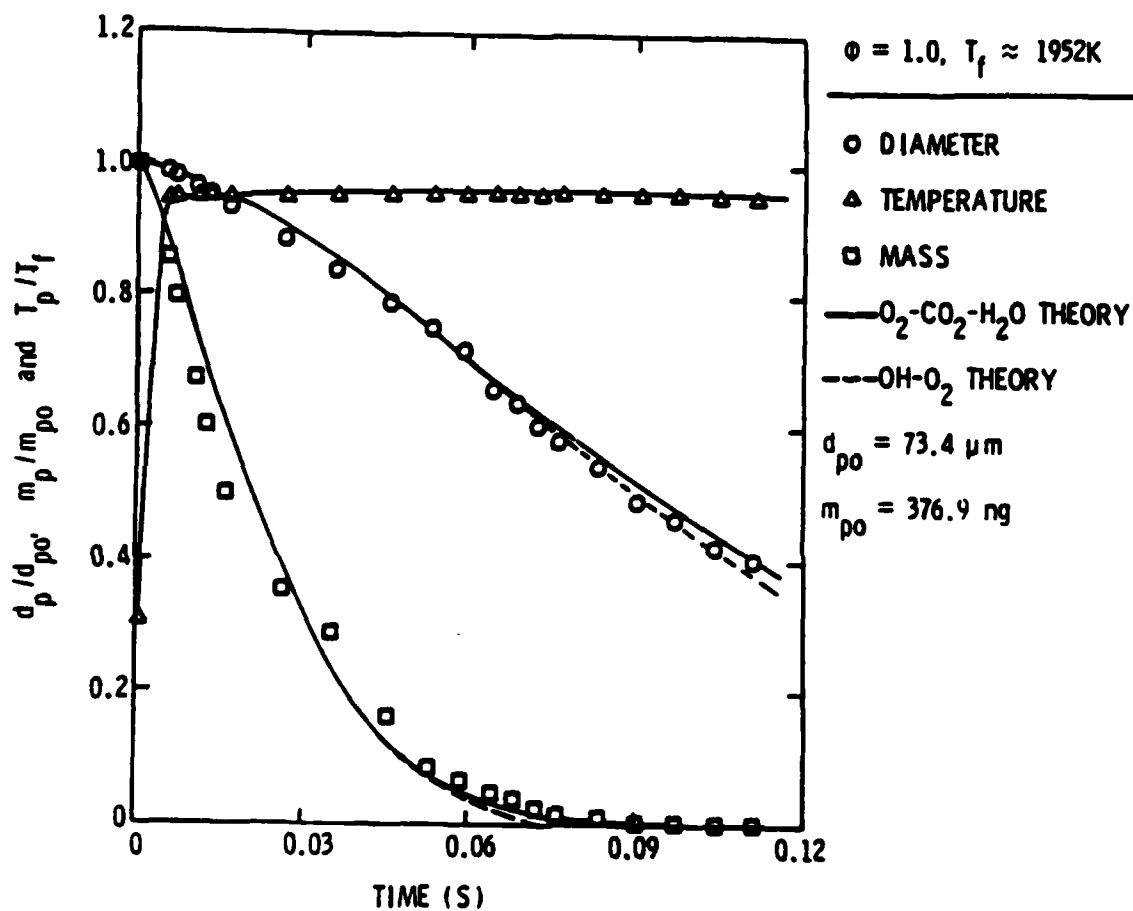


Figure 28. Particle-life history for  $\phi = 1.0$ ,  $T_f = 1952 K$ ,  $d_u = 300 nm$  and  $d_{po} = 73.4 \mu m$ .

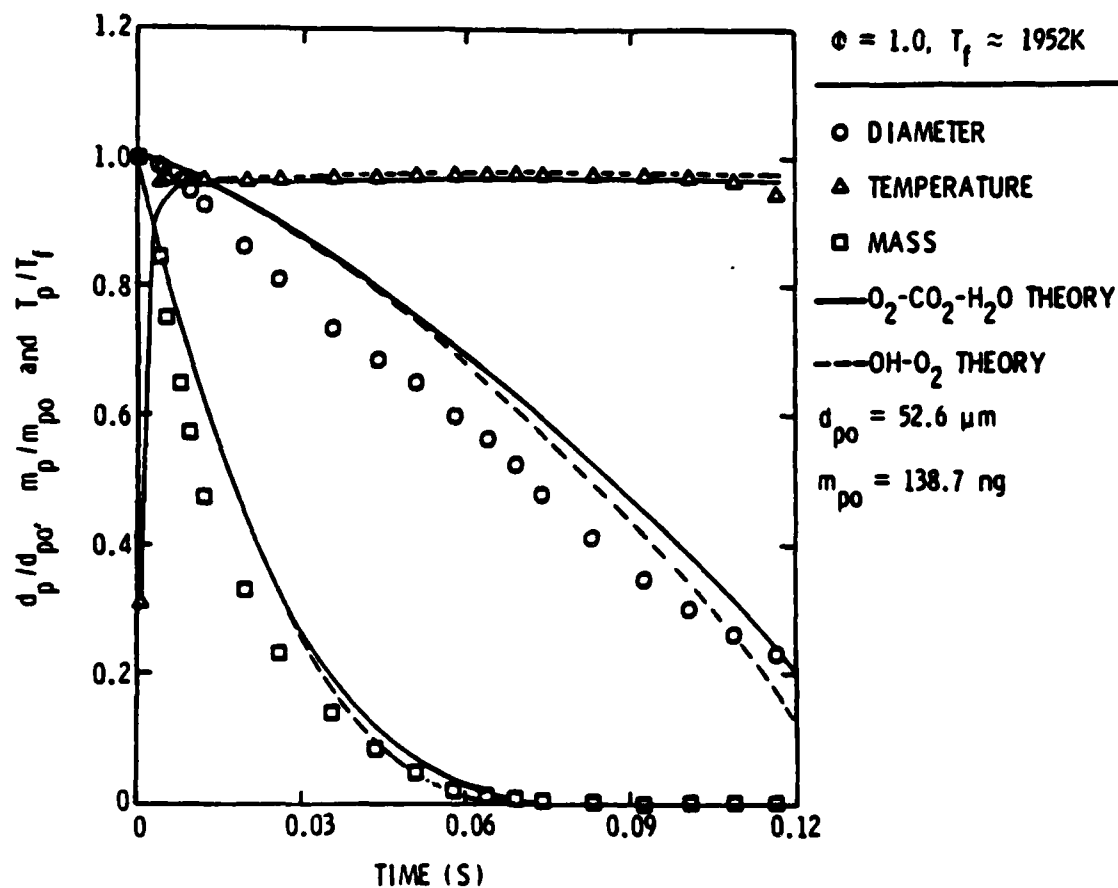


Figure 29. Particle-life history for  $\phi = 1.0$ ,  $T_f = 1952 \text{ K}$ ,  $d_u = 300 \text{ nm}$  and  $d_{po} = 52.6 \mu\text{m}$ .



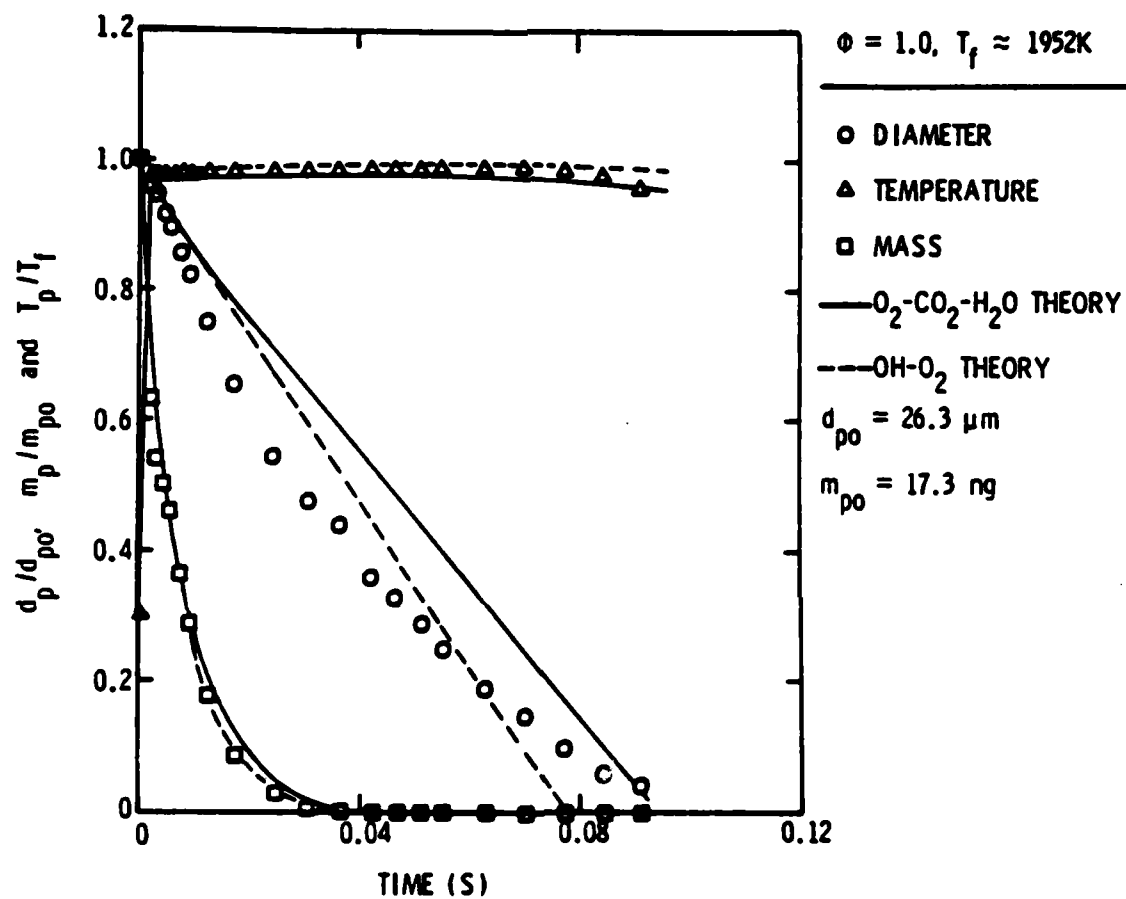


Figure 30. Particle-life history for  $\phi = 1.0$ ,  $T_f = 1952 \text{ K}$ ,  $d_u = 300 \text{ nm}$  and  $d_{po} = 26.3 \mu\text{m}$ .

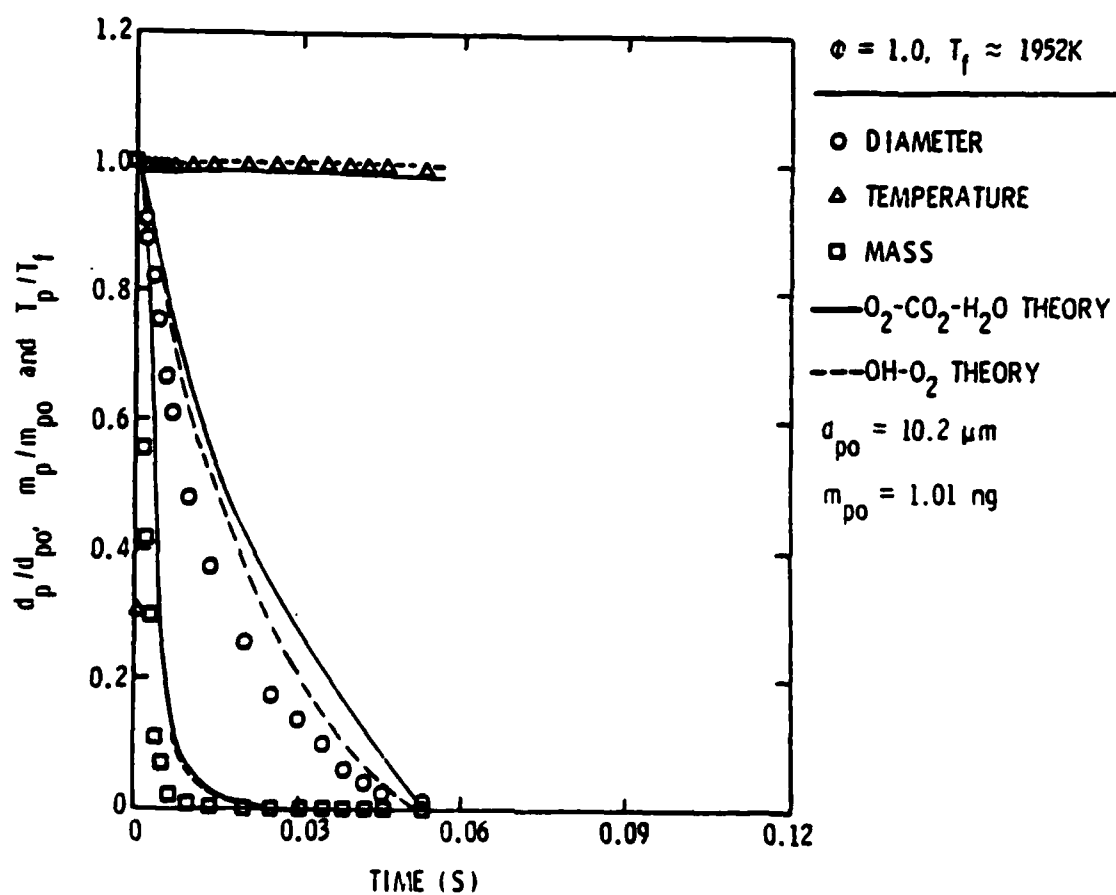


Figure 31. Particle-life history for  $\phi = 1.0$ ,  $T_f = 1952 \text{ K}$ ,  $d_u = 300 \text{ nm}$  and  $d_{po} = 10.2 \mu\text{m}$ .

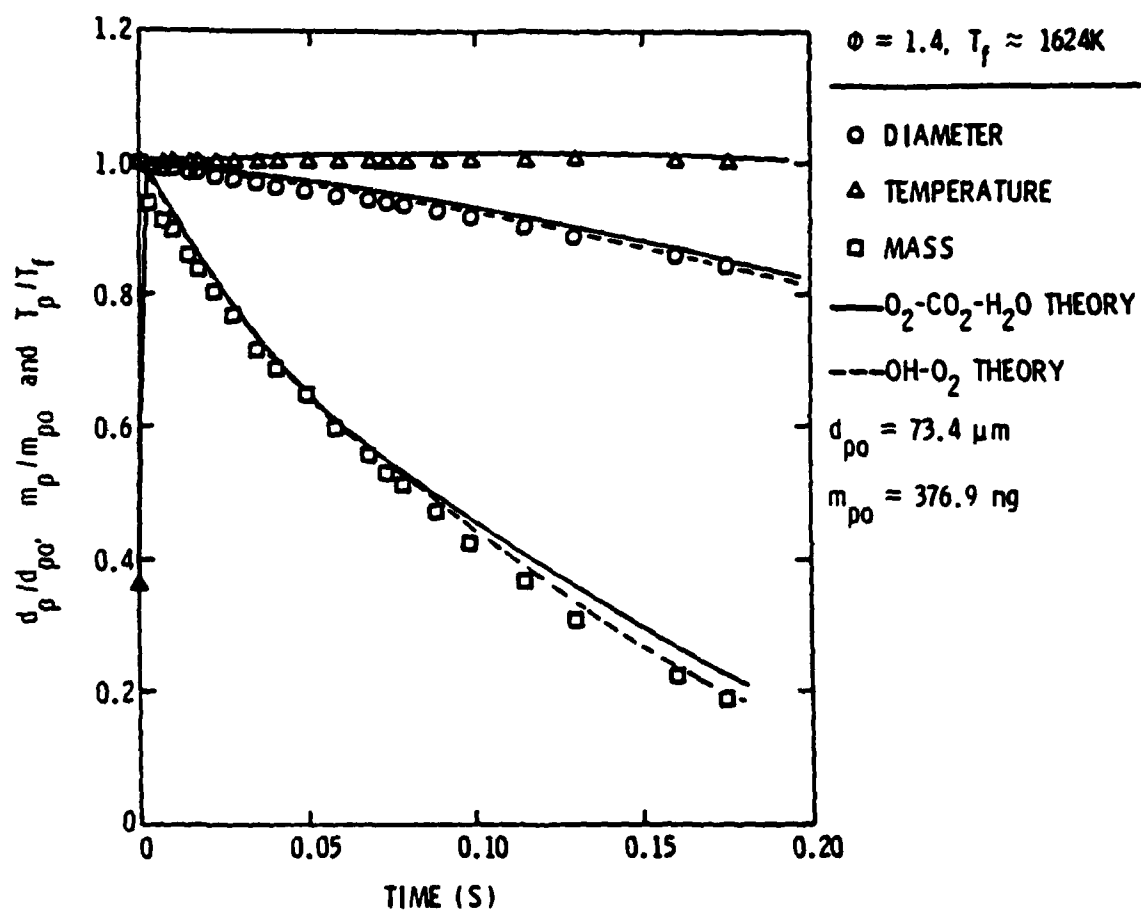


Figure 32. Particle-life history for  $\phi = 1.4$ ,  
 $T_f = 1624 \text{ K}$ ,  $d_u = 300 \text{ nm}$  and  $d_{po} = 73.4 \mu\text{m}$ .

range of conditions. However, the results also indicate that the model is effective in predicting particle heat-up, where reaction effects are small, and final particle temperature levels, where radiation and chemical energy release rates are important.

The time of particle heat-up is relatively short in comparison to the particle lifetime. Maximum particle temperatures exceed local gas temperatures when the reaction rate is high, e.g.,  $\phi = 0.6$  in Figs. 20-22; and are near or slightly below gas temperatures, due to radiation heat losses, when reaction rates are low, e.g., Figs. 19 and 23-32. Differences between gas and particle temperatures after heat-up are smaller than for the large particles observed earlier [6,7], since the small particle size of the present tests enhances convective transport. Due to the interaction of diffusion and reaction effects, agglomerate lifetime is a complex function of flame conditions and initial size. The main generality that can be made is that the lifetime is proportional to  $d_{po}^{1 \text{ to } 2}$ , where the latter power applies to diffusion-controlled conditions. Therefore, good slurry atomization is required to achieve high combustion efficiencies within a reasonable combustion chamber volume. Lifetimes are shortest for  $\phi = 0.6-0.8$  (considering present findings as well as Refs. 6 and 7); therefore, particle residence times at these conditions should be maximized to achieve high combustion efficiency in a minimum combustor volume.

Typical of any gasifying spherical particle, normalized particle mass decreases much more rapidly than normalized diameter; however, the rate of mass reduction is even greater for burning agglomerates due to the reduction in particle density as the pores develop. Therefore, conditions yielding a relatively high mass burnout of carbon could still yield relatively large agglomerate particles at the exit of the combustor.

Particle-life histories for agglomerates formed from carbon-blacks having  $d_u = 70$  and  $150$  nm are illustrated in Figs. 33-38. Flame conditions for these results were chosen to represent near kinetic-controlled (Figs. 37 and 38), near diffusion-controlled (Figs. 35-36) and intermediate (Figs. 33-34) conditions. Predictions of both reaction models are also plotted on the figures, using the correlations for empirical parameters appearing in Table 3. In general, the comparison between predictions and measurements is similar to the results for  $d_u = 300$  nm appearing in Figs. 19-32.

The effect of ultimate carbon particle size on the agglomerate-life history varied depending on flame conditions. Trends with respect to  $d_u$  are most easily seen by comparing residence times required to react fixed fractions of the initial agglomerate mass. These times are summarized in Table 4 for test conditions where all three values of  $d_u$  were considered. Measured residence times to react 70 and 90% of the carbon mass ( $t_{70\%}$  and  $t_{90\%}$ ) are shown in the table. Theoretical values are nearly the same, except for  $\phi = 0.6$ ,  $T_f = 1663$  K and  $d_u = 300$  nm, where the measured values are significantly larger than predicted, in which case both values are shown in the table. Since the theory provides satisfactory predictions for the rest of the database, this particular measurement may be anomalous. The plot of the data appearing in Fig. 20 for this condition also suggests problems with this measurement.

In general, reducing  $d_u$  reduces residence times required for carbon consumption. Aside from the condition mentioned above, when the prediction is probably the best indication of residence times, residence times are reduced in the range 10-20% as  $d_u$  is decreased from 300 to 70 nm. The

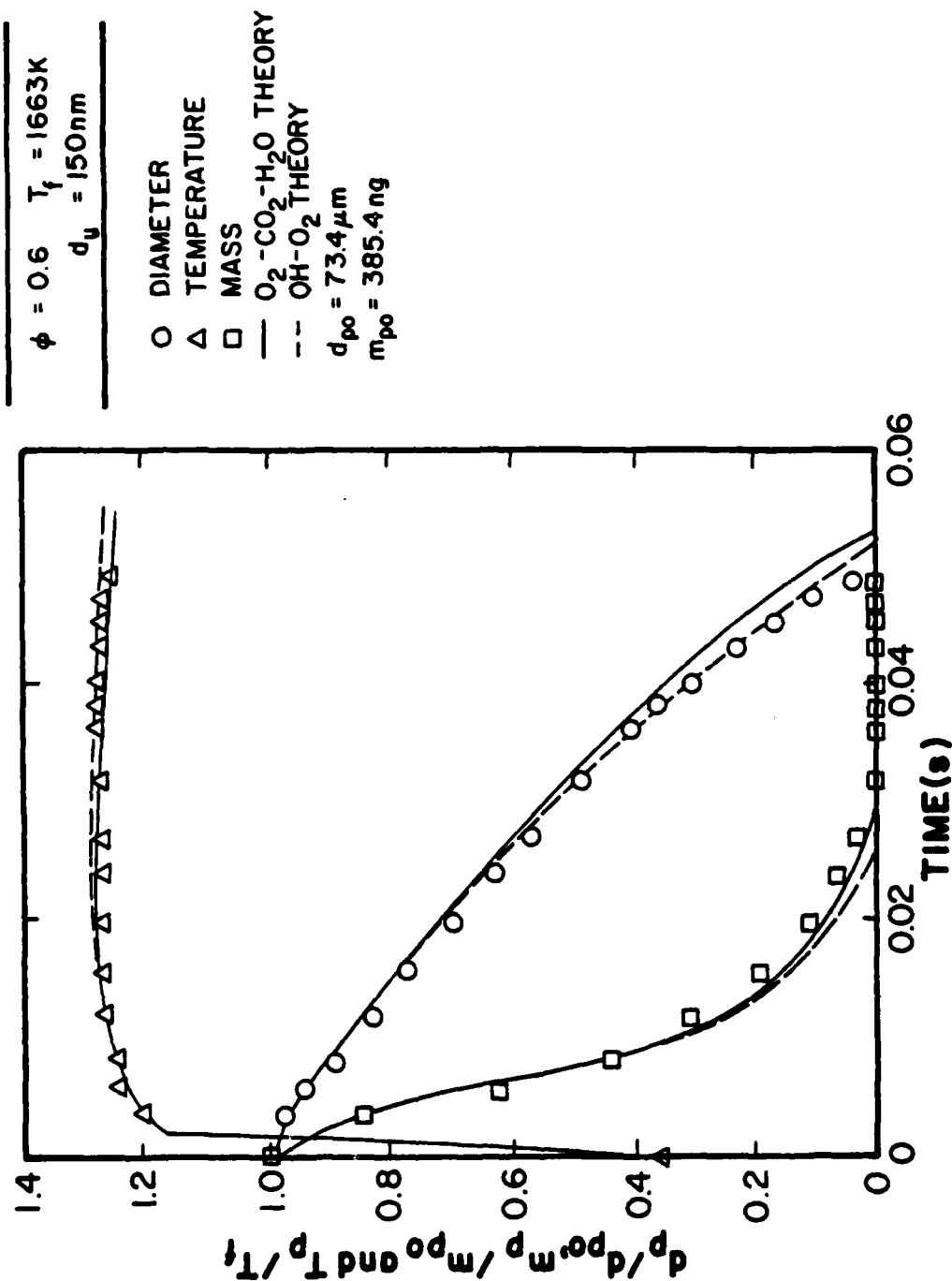


Figure 33. Particle-life history for  $\phi = 0.6$ ,  $T_f = 1663\text{ K}$ ,  $d_u = 150\text{ nm}$  and  $d_{p0} = 73.4\text{ }\mu\text{m}$ .

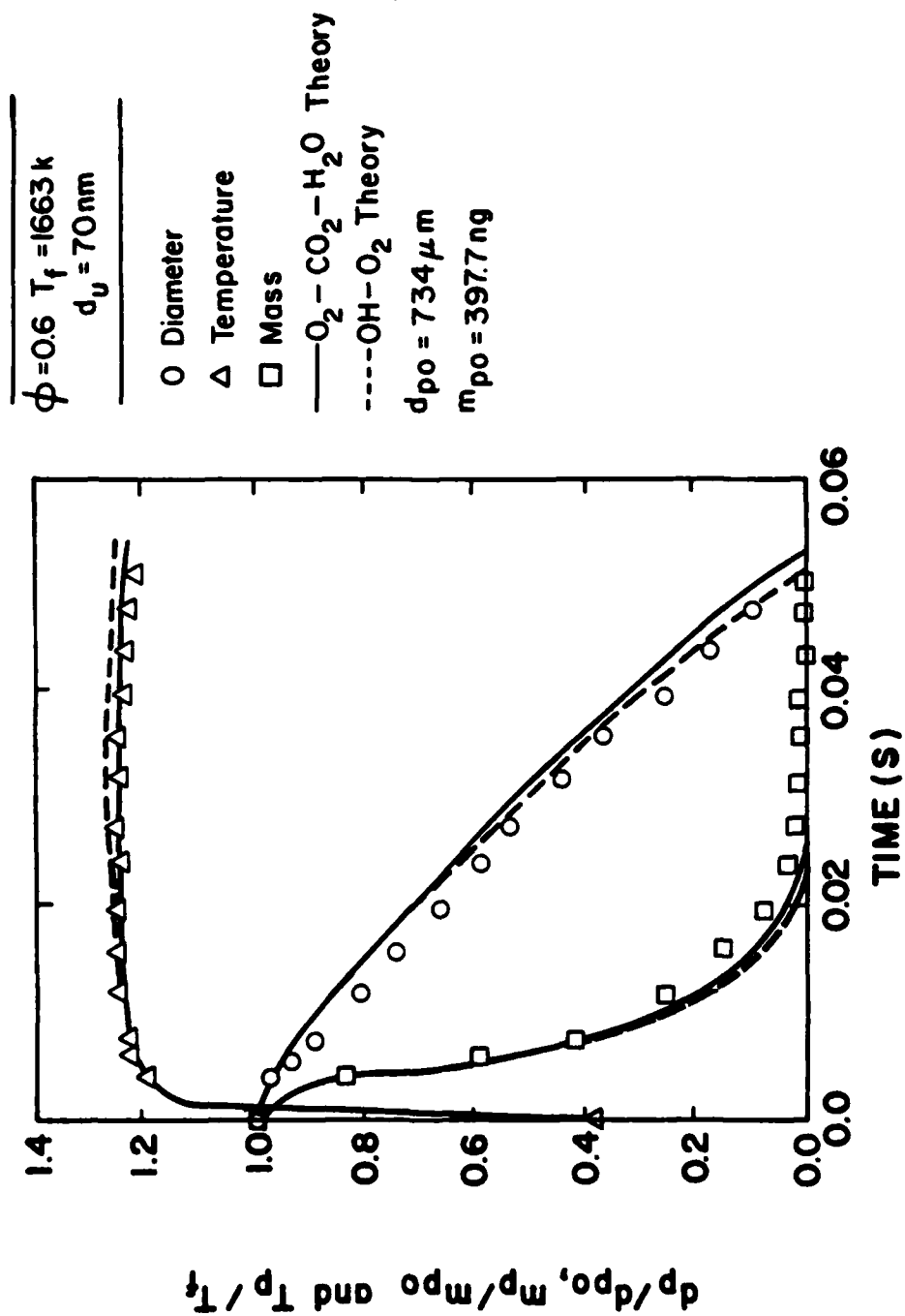


Figure 34. Particle-life history for  $\phi = 0.6$ ,  $T_f = 1663 \text{ K}$ ,  $d_u = 70 \text{ nm}$  and  $d_{po} = 73.4 \mu\text{m}$ .

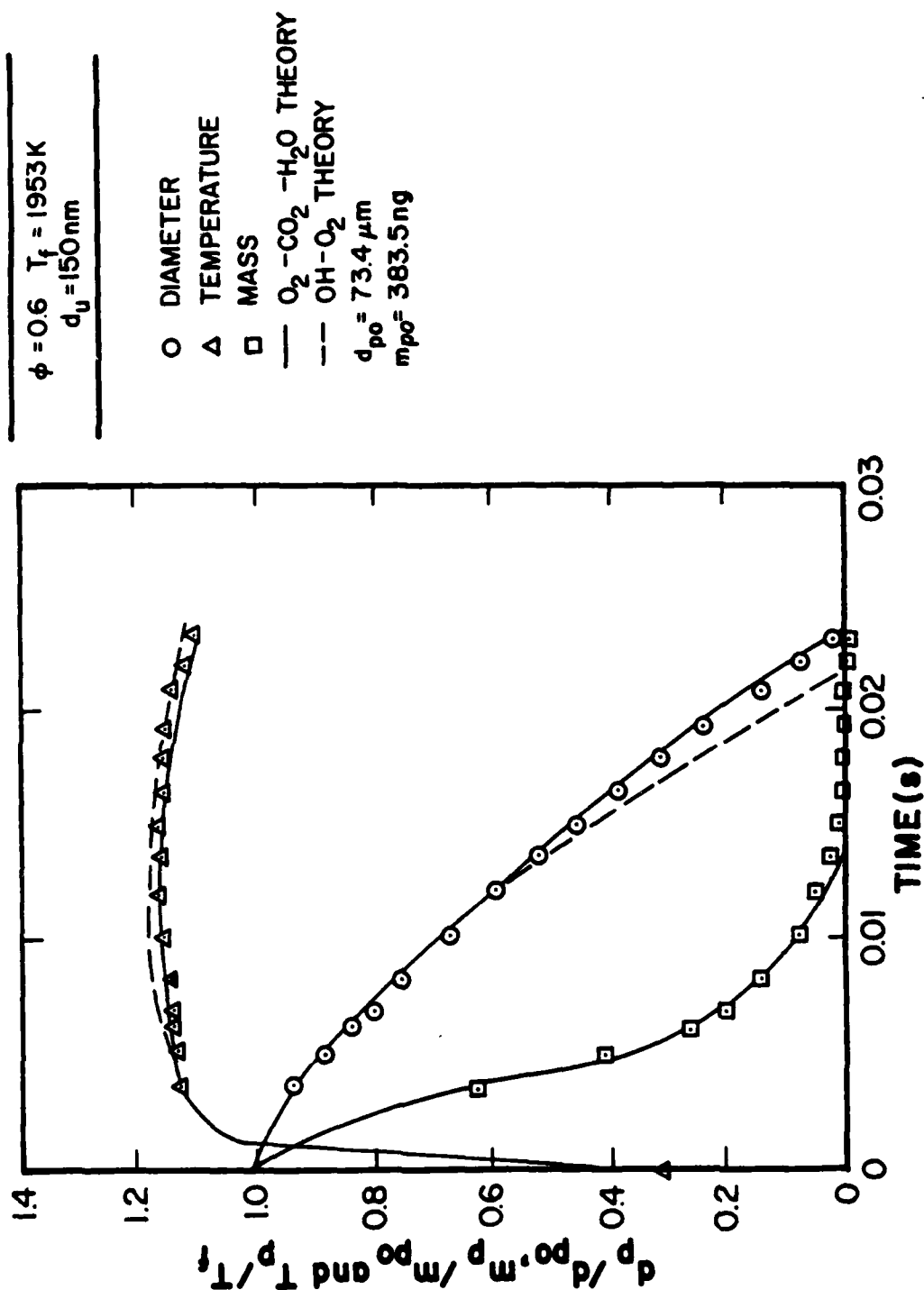


Figure 35. Particle-life history for  $\phi = 0.6$ ,  $T_f = 1953\text{ K}$ ,  $d_u = 150\text{ nm}$  and  $d_{po} = 73.4\text{ }\mu\text{m}$ .



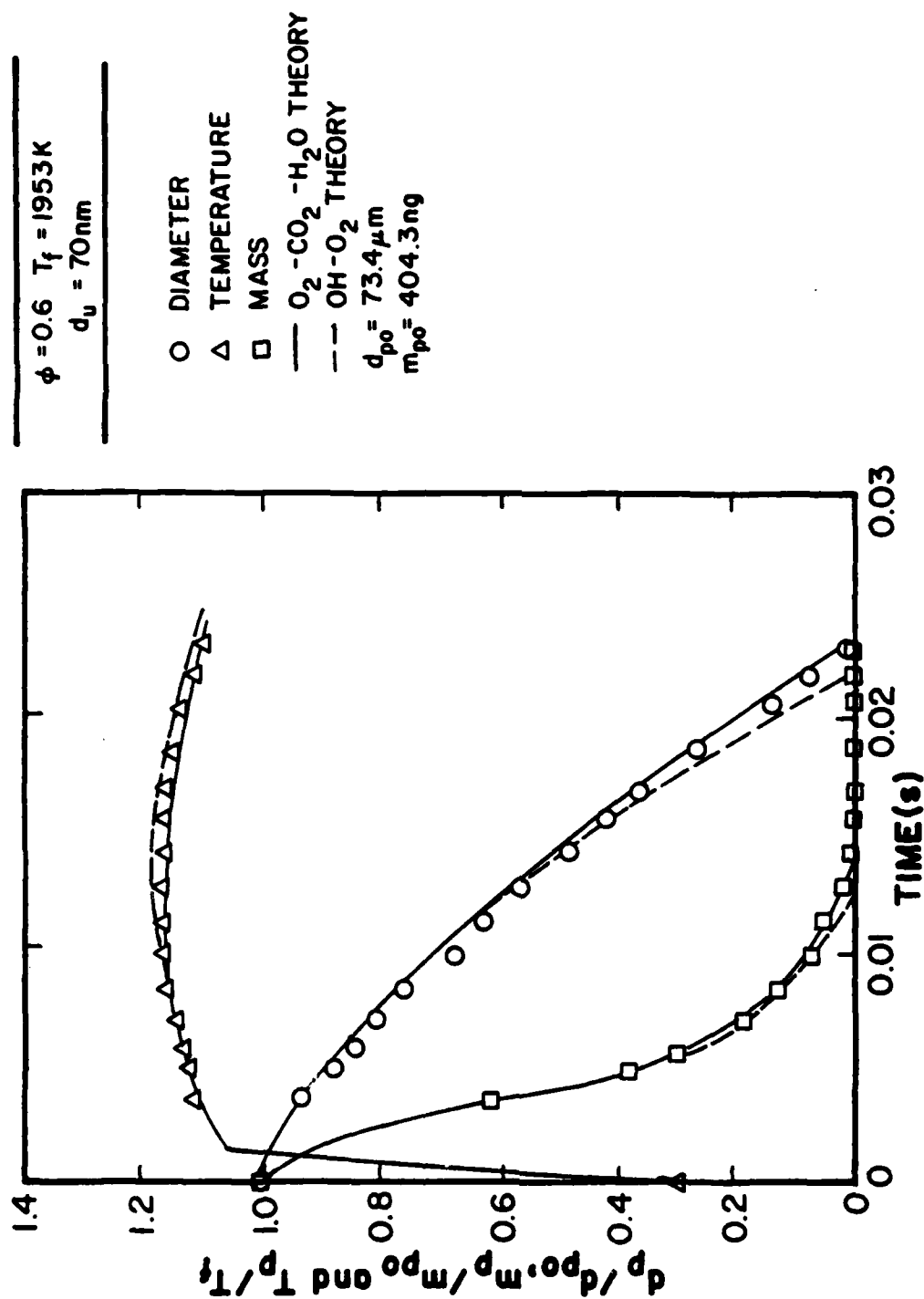


Figure 36. Particle-life history for  $\phi = 0.6$ ,  $T_f = 1953 \text{ K}$ ,  $d_u = 70 \text{ nm}$  and  $d_{po} = 73.4 \mu\text{m}$ .

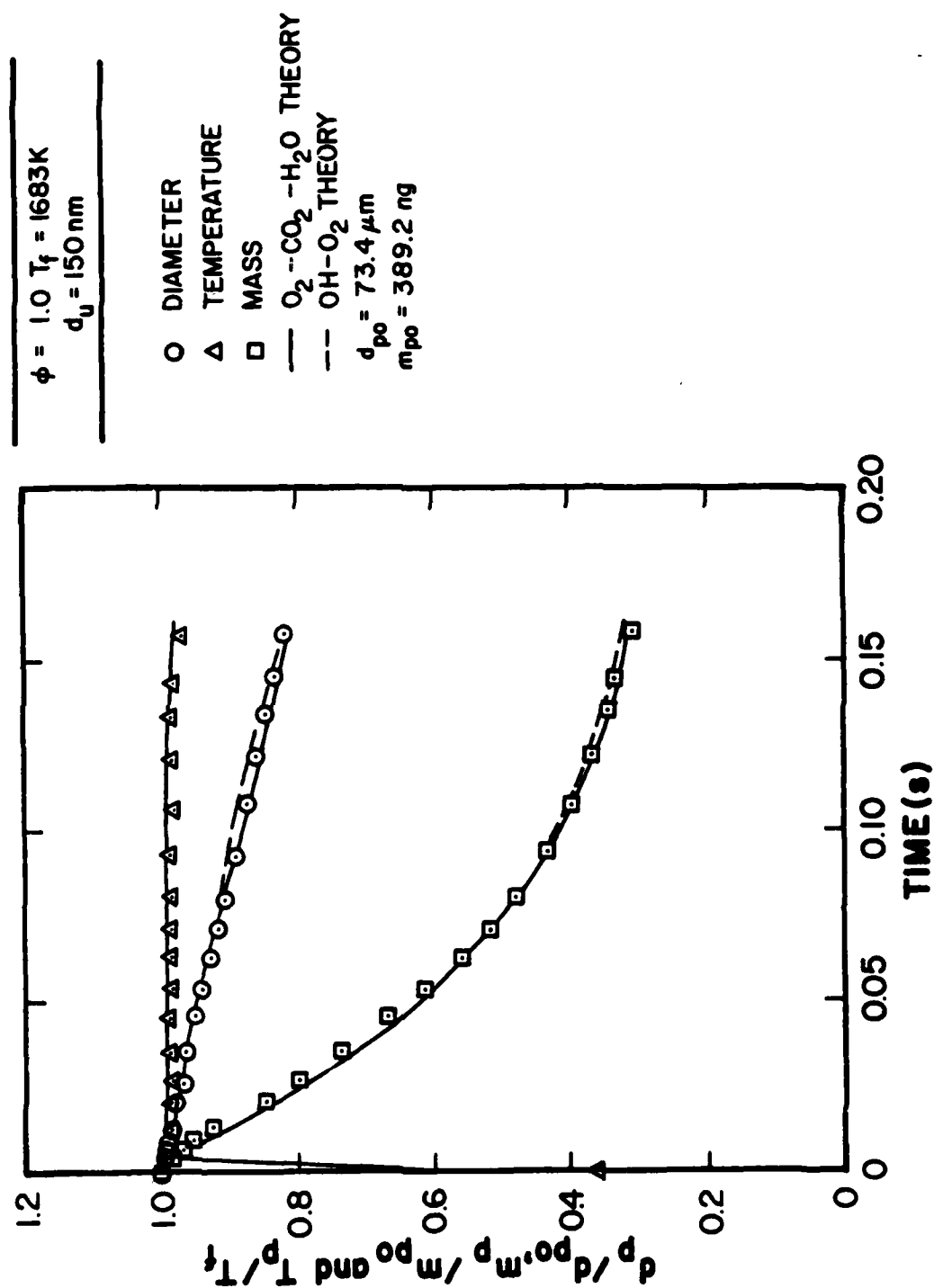


Figure 37. Particle-life history for  $\phi = 1.0$ ,  $T_f = 1683\text{ K}$ ,  $d_u = 150\text{ nm}$  and  $d_{p0} = 73.4\text{ }\mu\text{m}$ .

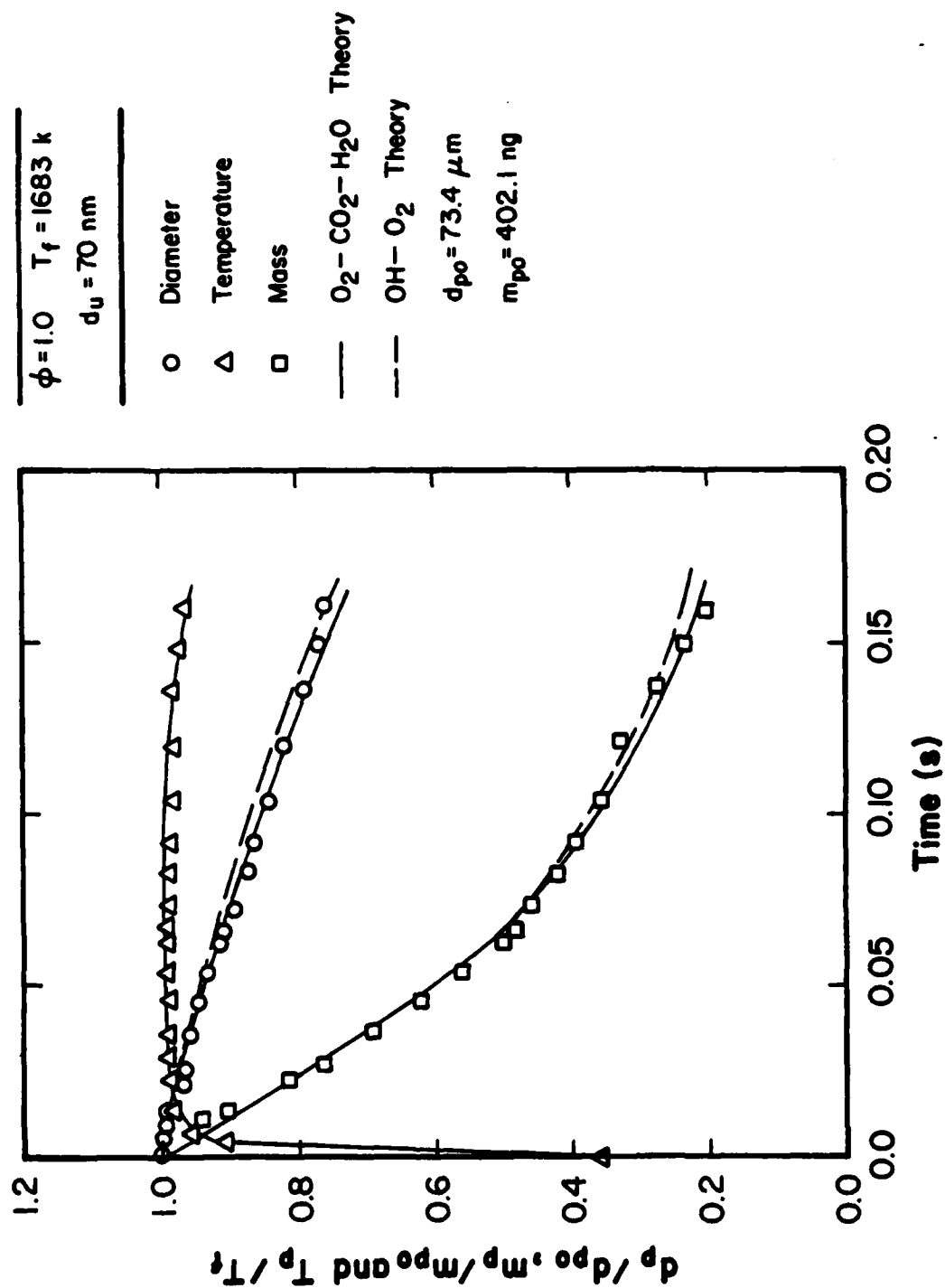


Figure 38. Particle-life history for  $\phi = 1.0$ ,  $T_f = 1683 \text{ K}$ ,  $d_u = 70 \text{ nm}$  and  $d_{p0} = 73.4 \text{ } \mu\text{m}$ .

Table 4. Effect of Carbon-Black Ultimate Carbon Particle Size on Agglomerate Combustion Times<sup>a</sup>

$d_u$ (nm)	$t_{70\%}$ (ms) <sup>b</sup>	$t_{90\%}$ (ms) <sup>b</sup>	Figure No.
$\phi = 0.6, T_f = 1663$ K, mixed condition:			
300	14.5 (12.1) <sup>c</sup>	27.3 (19.4) <sup>c</sup>	20
150	11.9	20.3	33
70	10.9	18.2	34
$\phi = 0.6, T_f = 1953$ K, near diffusion-control:			
300	5.5	10.0	22
150	5.5	9.4	35
70	5.6	9.1	36
$\phi = 1.0, T_f = 1683$ K, near kinetic-control:			
300	150	--	23
150	162	--	37
70	124	--	38

<sup>a</sup> $d_{po} = 73.4$   $\mu$ m

<sup>b</sup>Measured times for 70 and 90% consumption of initial agglomerate mass.

<sup>c</sup>Theoretical prediction (Neoh et al. mechanism).

largest reduction in residence time is observed near kinetic-controlled conditions. This behavior agrees with the trends of the empirical parameters as  $d_u$  is varied shown in Table 3, i.e., the  $a_1$  and  $\zeta$  increase slightly as  $d_u$  decreases, tending to increase rates of carbon consumption at kinetic-controlled conditions. In general, however, these effects are small--roughly comparable to present experimental accuracy.

Effects of flame conditions and initial agglomerate diameter exert stronger influences on residence times for agglomerate reaction than  $d_u$ . The effect of flame temperature variations for  $\phi = 0.6$  and 1.0 is illustrated in Figs. 39 and 40. Reacted mass fraction is plotted as a function of time for different flame temperatures with  $d_{po}$  and  $d_u$  held constant. Predictions for the models using both reaction mechanisms are shown along with the measurements. Increasing temperature results in appreciable reductions in the residence time required to react a given fraction of the agglomerate mass--particularly at conditions approaching reaction-control, e.g.,  $\phi = 1$  in Fig. 40. Near diffusion-controlled conditions, e.g., the high temperature results for  $\phi = 0.6$  in Fig. 39, the effect of temperature is less significant. Here, reaction rates are primarily dependent on gas-phase transport properties which are only mildly influenced by temperature changes for these conditions.

Similar results are plotted in Figs. 41-43. In this case,  $\phi$  is varied for a constant temperature in each figure. Over this test range, reducing  $\phi$  from unity results in significant reduction in particle lifetimes. This occurs since oxygen is the most effective reactant of carbon. At high equivalence ratios, there is little oxygen available in the particle surroundings and reaction primarily proceeds via OH--if the recent results of Neoh et al. [18] are correct--and OH is never present in high concentrations.

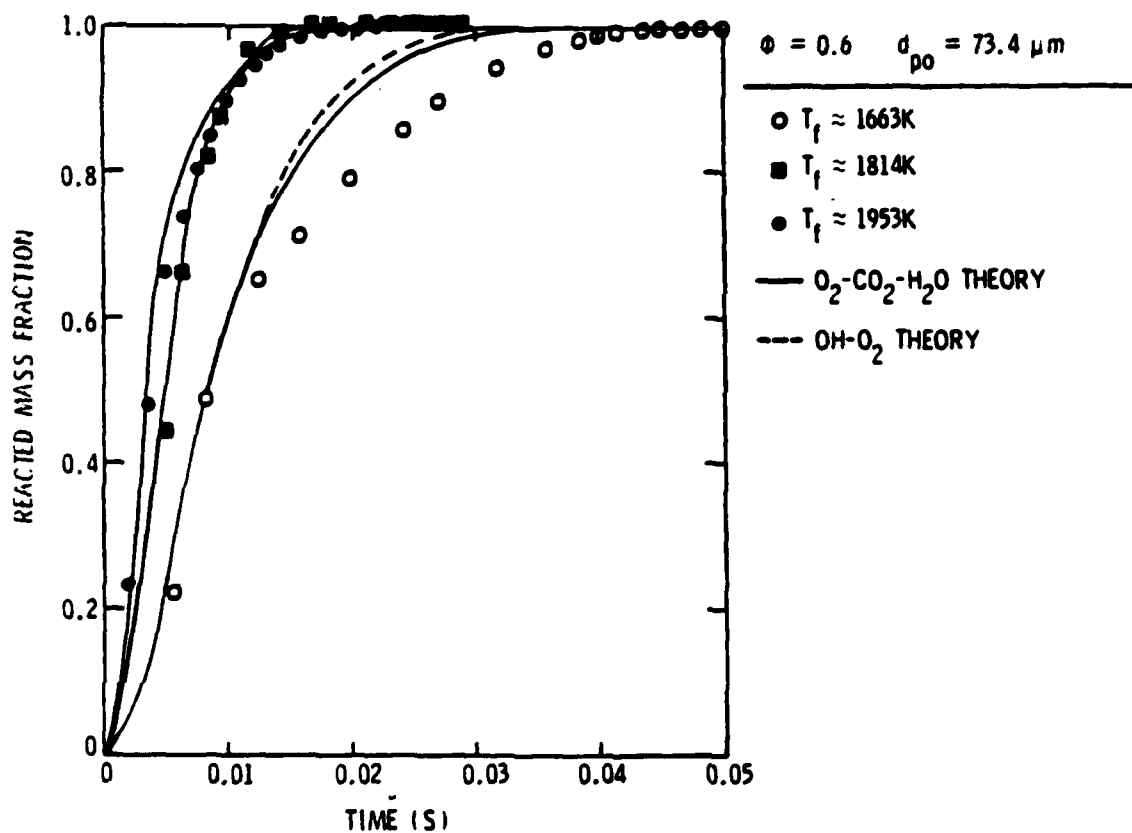


Figure 39. Effect of ambient temperature on the variation of reacted mass fraction with time.  $\phi = 0.6$ ,  $d_{po} = 73.4 \mu m$ ,  $d_u = 300 nm$ .

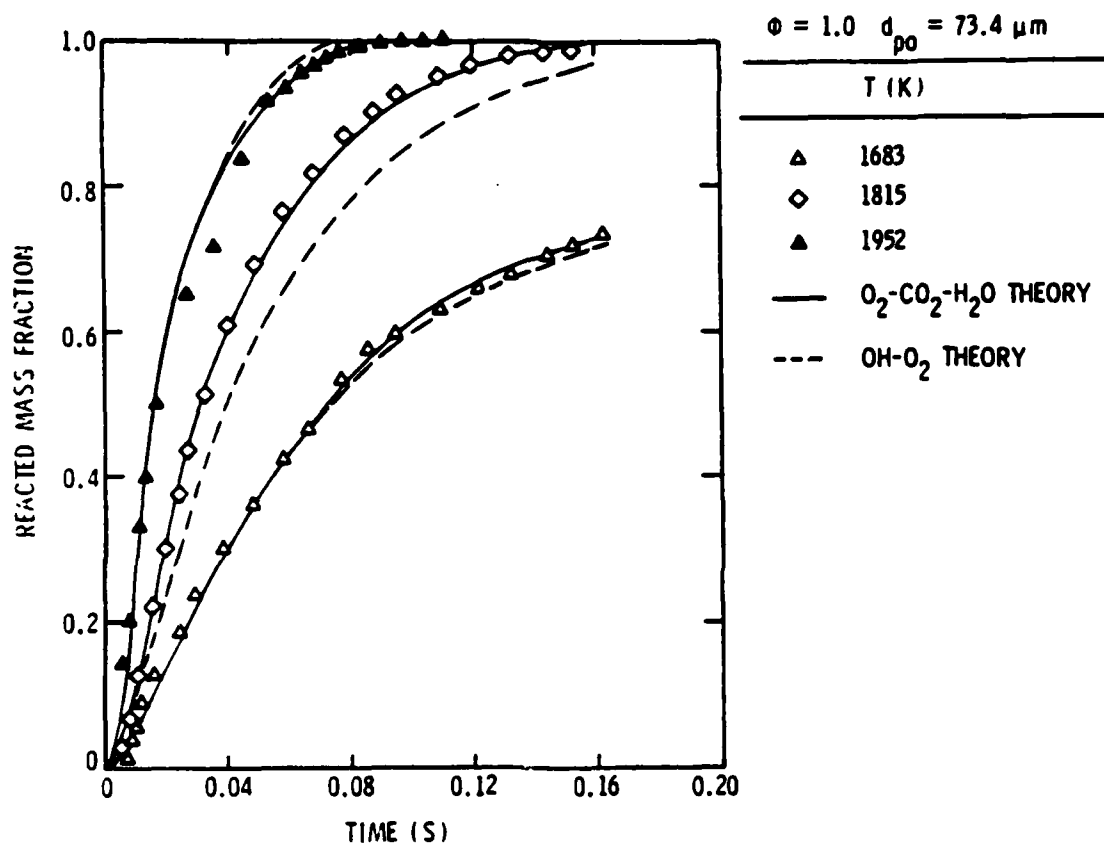


Figure 40. Effect of ambient temperature on the variation of reacted mass fraction with time.  $\phi = 1.0$ ,  $d_{po} = 73.4 \mu m$ ,  $d_u = 300 nm$ .

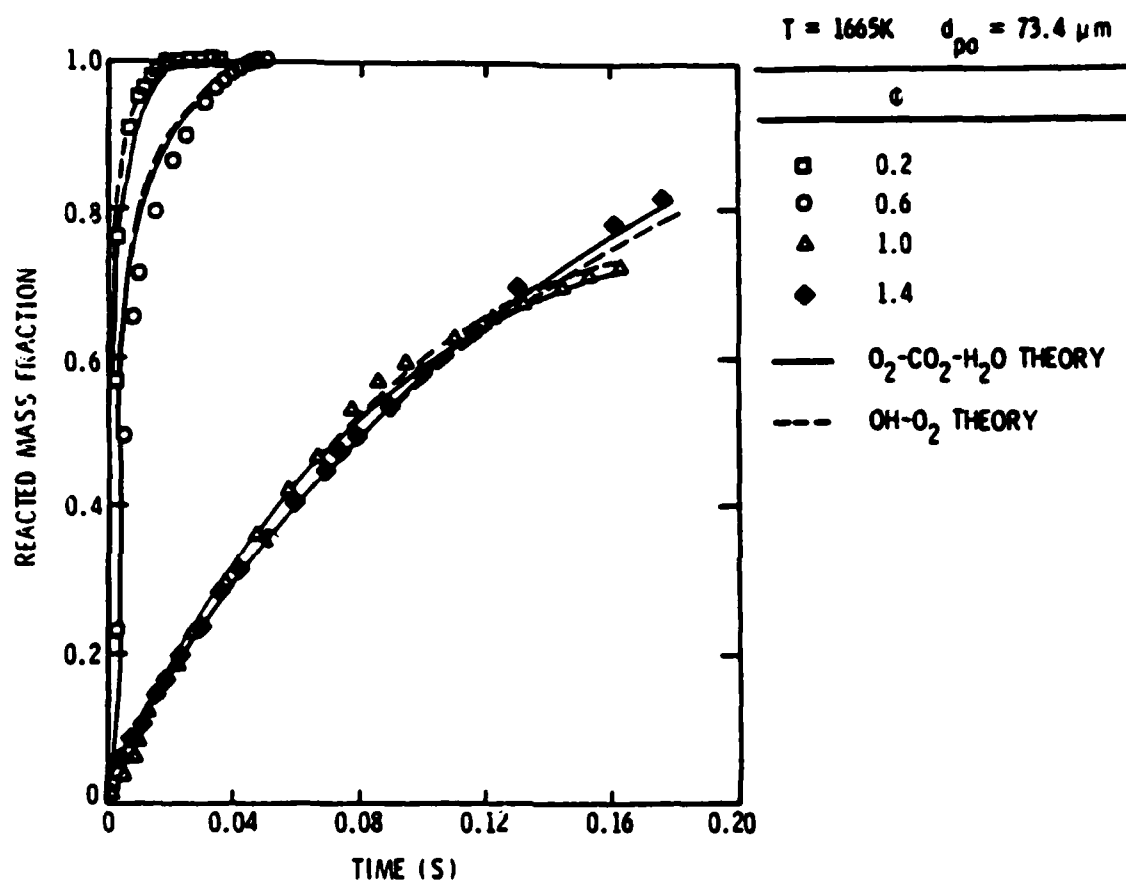


Figure 41. Effect of ambient equivalence ratio on the variation of reacted mass fraction with time.  $T_f = 1665 K$ ,  $d_{po} = 73.4 \mu m$ ,  $d_u = 300 nm$ .



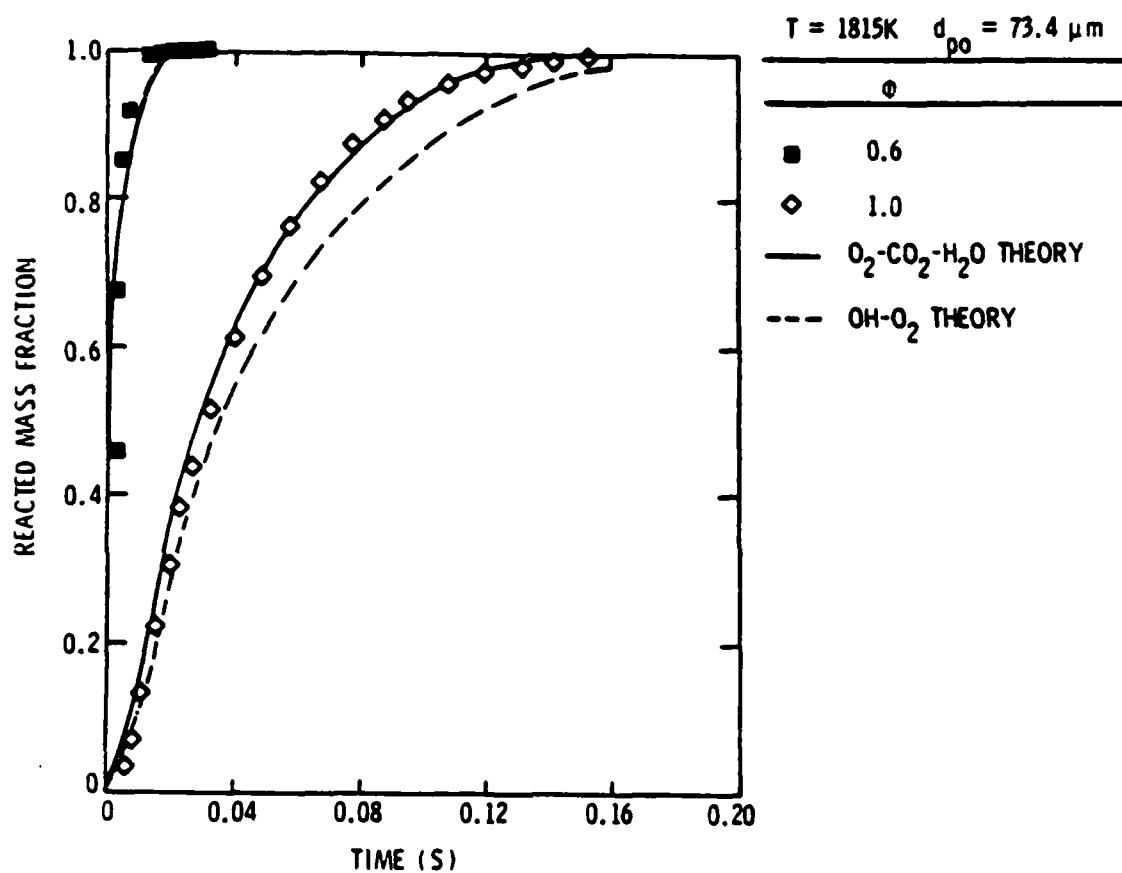


Figure 42. Effect of ambient equivalence ratio on the variation of reacted mass fraction with time.  $T_f = 1815 \text{ K}$ ,  $d_{po} = 73.4 \mu\text{m}$ ,  $d_u = 300 \text{ nm}$ .

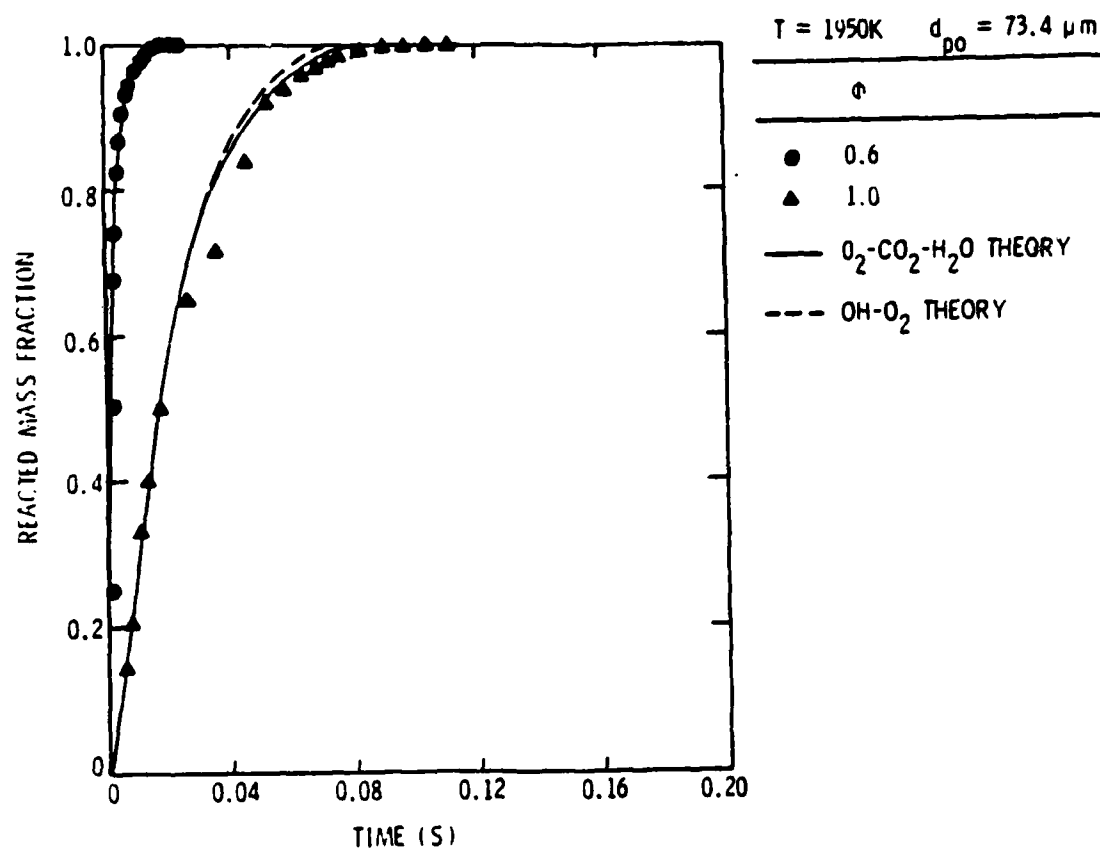


Figure 43. Effect of ambient equivalence ratio on the rate of reacted mass fraction with time.  
 $d_{po} = 73.4 \mu m$ ,  $d_u = 300 nm$ .

AD-A121 889

COMBUSTION OF AGGLOMERATES FORMED BY CARBON SLURRY  
FUELS(U) PENNSYLVANIA STATE UNIV UNIVERSITY PARK DEPT  
OF MECHANICAL EN. G A SZEKELY ET AL. SEP 82

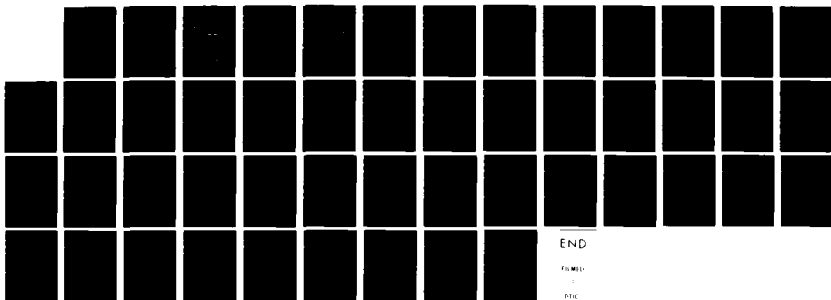
2/2

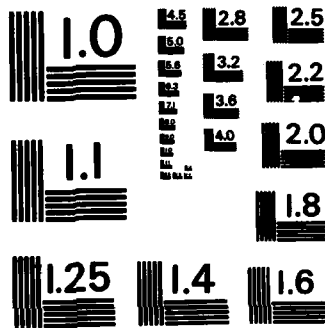
UNCLASSIFIED

AFWAL-TR-82-2085 F33615-81-K-2039

F/G 21/2

NL





MICROCOPY RESOLUTION TEST CHART  
NATIONAL BUREAU OF STANDARDS-1963-A

The effect of initial agglomerate size on residence times required for carbon reaction is illustrated in Fig. 44, for  $\phi = 1$  and flame temperatures of 1683 and 1952 K. As noted earlier, residence times for reaction are proportional to  $d_{po}^{-1}$  to  $d_{po}^{-2}$  for the low Reynolds numbers considered during present tests. Residence time requirements are nearly proportional to  $d_{po}$  as the process approaches reaction-control. This condition is represented by the test results at 1683 K in Fig. 44. Therefore, improved atomization, yielding smaller initial agglomerate diameters, is one of the most effective methods for improving combustion efficiency.

#### 4.2 Agglomerates of Carbon-Black Blends

##### 4.2.1 Appearance

Blends of carbon-blacks having different ultimate carbon particle sizes are likely for formulations of practical slurry fuels, in order to obtain acceptable rheological and stability properties. The final phase of the present investigation involved a brief examination of the combustion properties of blends. Work was limited to testing and analysis of a single bimodal blend consisting of carbon-blacks having ultimate carbon particle sizes of 70 and 300 nm, with equal mass loading of each size.

The appearance of agglomerates from the bimodal blend was similar to the monodisperse carbon-black formulations considered during this study. The main difference was at the start of reaction, where the bimodal agglomerates were somewhat smoother than the monodisperse agglomerates. This follows from the capability of the smaller particles to fit in the space between the large particles in the blend.

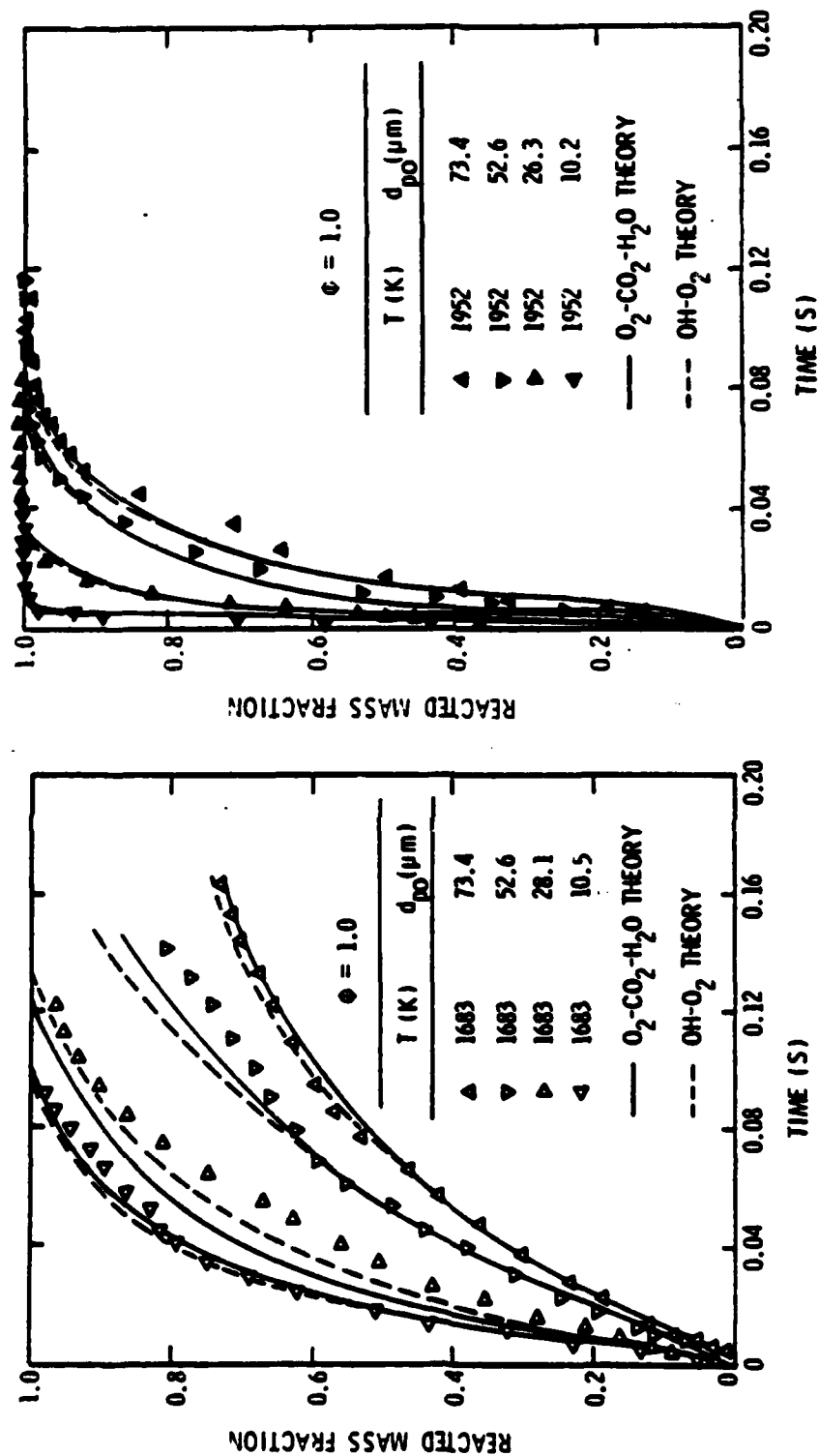


Figure 44. Effect of initial particle diameter on the variation of reacted mass fraction with time.  $\phi = 1$ ,  $d_u = 300$  nm.

#### 4.2.2 Empirical Parameters

Data obtained for the bimodal blends are summarized in Appendix A. The initial density of bimodal agglomerates was roughly 16% higher than the monodisperse agglomerates-- $2108 \text{ kg/m}^3$  as opposed to  $1820 \text{ kg/m}^3$ . This is expected from solid-state theory, since the smaller particles help to fill in the voids between the larger particles.

The variation of bimodal agglomerate density as a function of extent of reaction is illustrated in Fig. 45 for the three flame conditions tested. The empirical fit developed for monodisperse agglomerates, Eq. (1), is also shown on the figure for comparison. The variation in density with extent of reaction is relatively independent of flame conditions. The density of the bimodal agglomerate varied in the same manner as for the monodisperse agglomerates, aside from the different initial value of density. This yields the following expression for the density of the bimodal agglomerate

$$\rho_p = 2108 (1 - \epsilon)^{0.6} \quad (25)$$

These results imply similar behavior for the development of the pore structure for both monodisperse and bimodal agglomerates. The pore layer has a characteristic thickness less than 25% of the particle radius for  $\epsilon < 75\%$ , but penetrates to the center of the agglomerate during the latter stages of reaction.

The pore structure of the bimodal agglomerate enhances convective transport, however, the effect was less pronounced than for monodisperse agglomerates. The transport-enhancement factors for the bimodal agglomerate are illustrated in Fig. 46, along with the correlations found for present tests with monodisperse agglomerates and the earlier findings for large

$\phi$	$T_f(K)$	$d_{p0}(nm)$
○	0.6	1663
●	0.6	1953
△	1.0	1683
		73.4

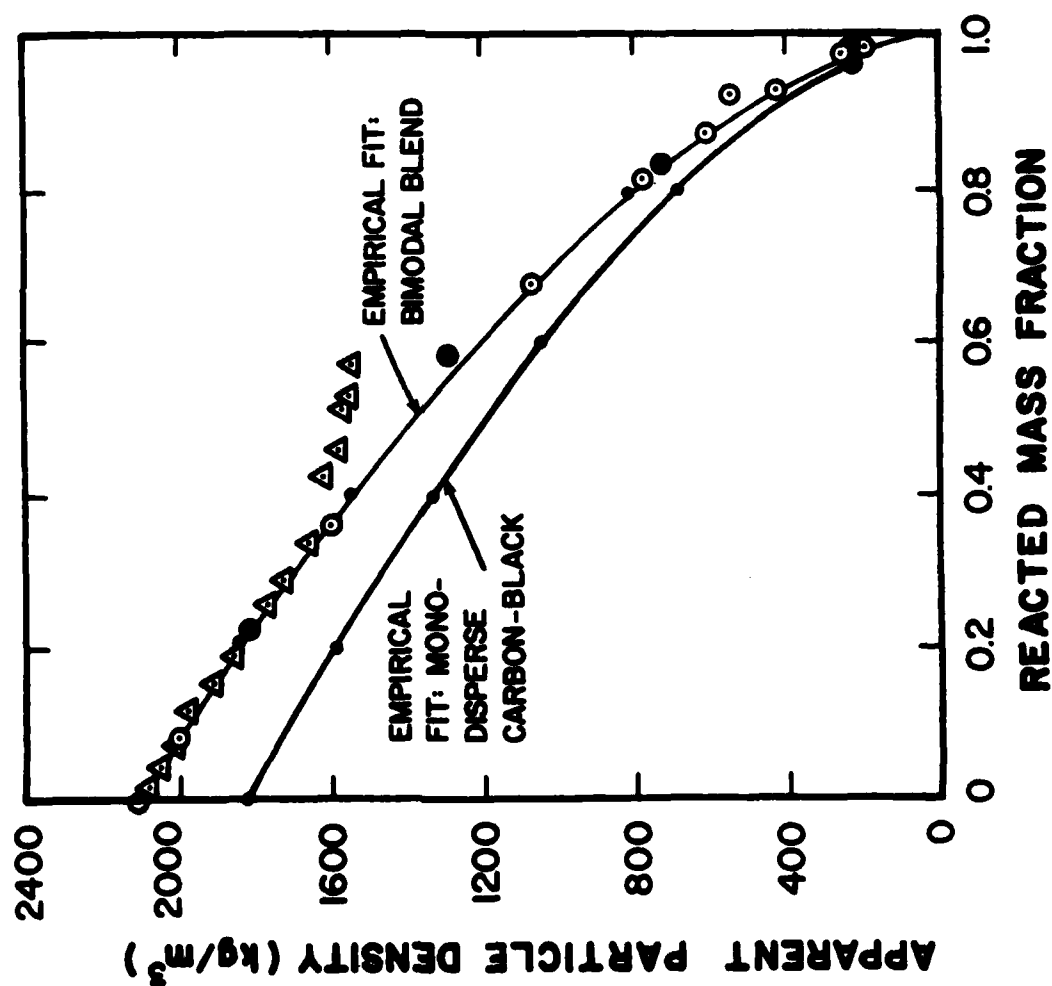
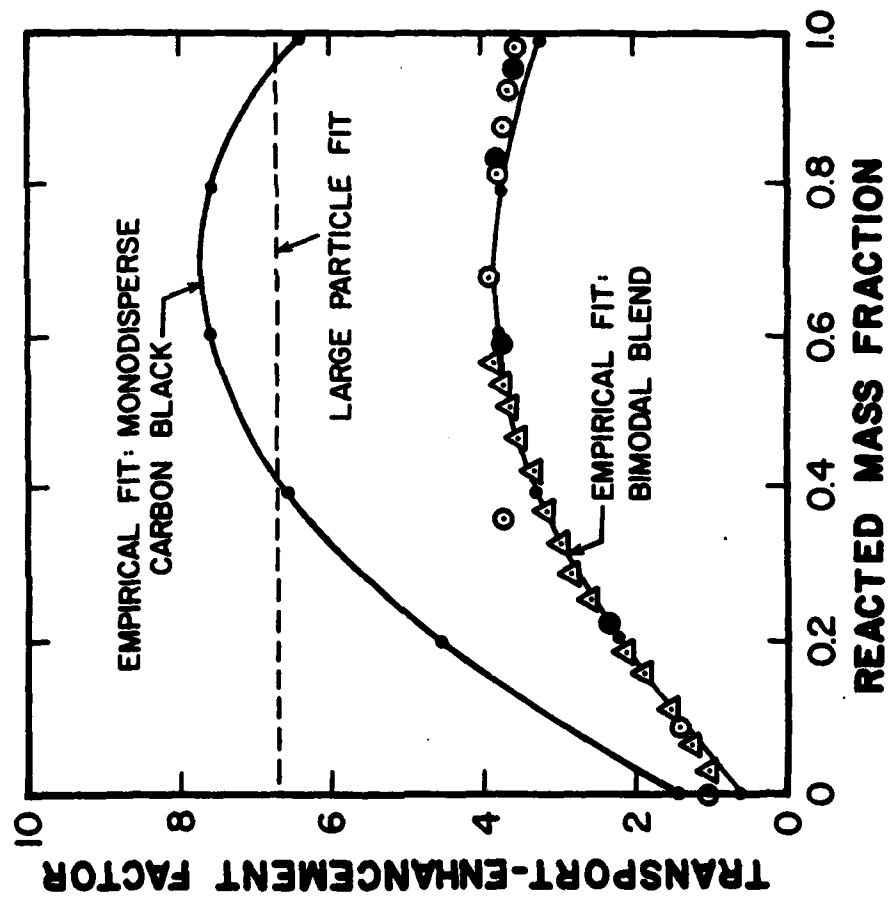


Figure 45. Apparent particle density as a function of reacted mass fraction for the bimodal agglomerate.





$\phi$	$T_f(K)$	$d_{p0}(\mu m)$
○	0.6	1663
●	0.6	1953
△	1.0	1683
△	1.0	1683

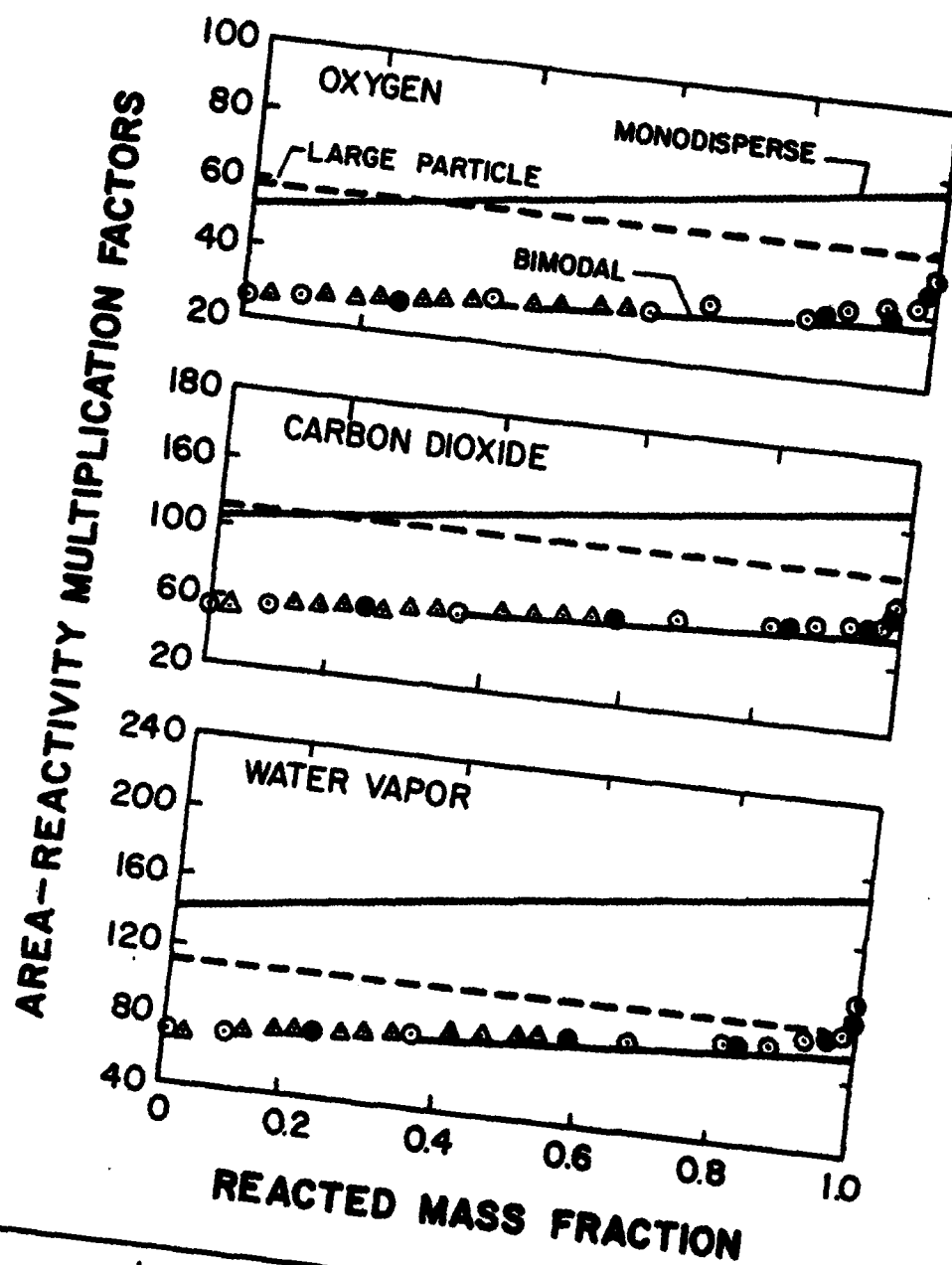
Figure 46. Transport-enhancement factor as a function of reacted mass fraction for the bimodal agglomerate.

monodisperse agglomerates [6,7]. The blends behave qualitatively the same as the monodisperse agglomerates. The value of  $\zeta$  was nearly unity at the start of the process. As the pores develop, however,  $\zeta$  increases reaching a maximum near  $\epsilon = 0.75$ . The reduction of  $\zeta$  in the latter stages of the process corresponds to the region when the pore layer has reached the center of the agglomerate. The variation of  $\zeta$  with  $\epsilon$  is essentially independent of flame conditions.

The main difference in  $\zeta$  between bimodal and monodisperse agglomerates is that maximum values of  $\zeta$  are 50% lower for bimodal agglomerates. It appears that the smaller particles in the bimodal agglomerate tend to inhibit the development of pores. Therefore, the gas is less able to percolate through the particle, i.e., the small particles tend to clog the void space between the larger particles.

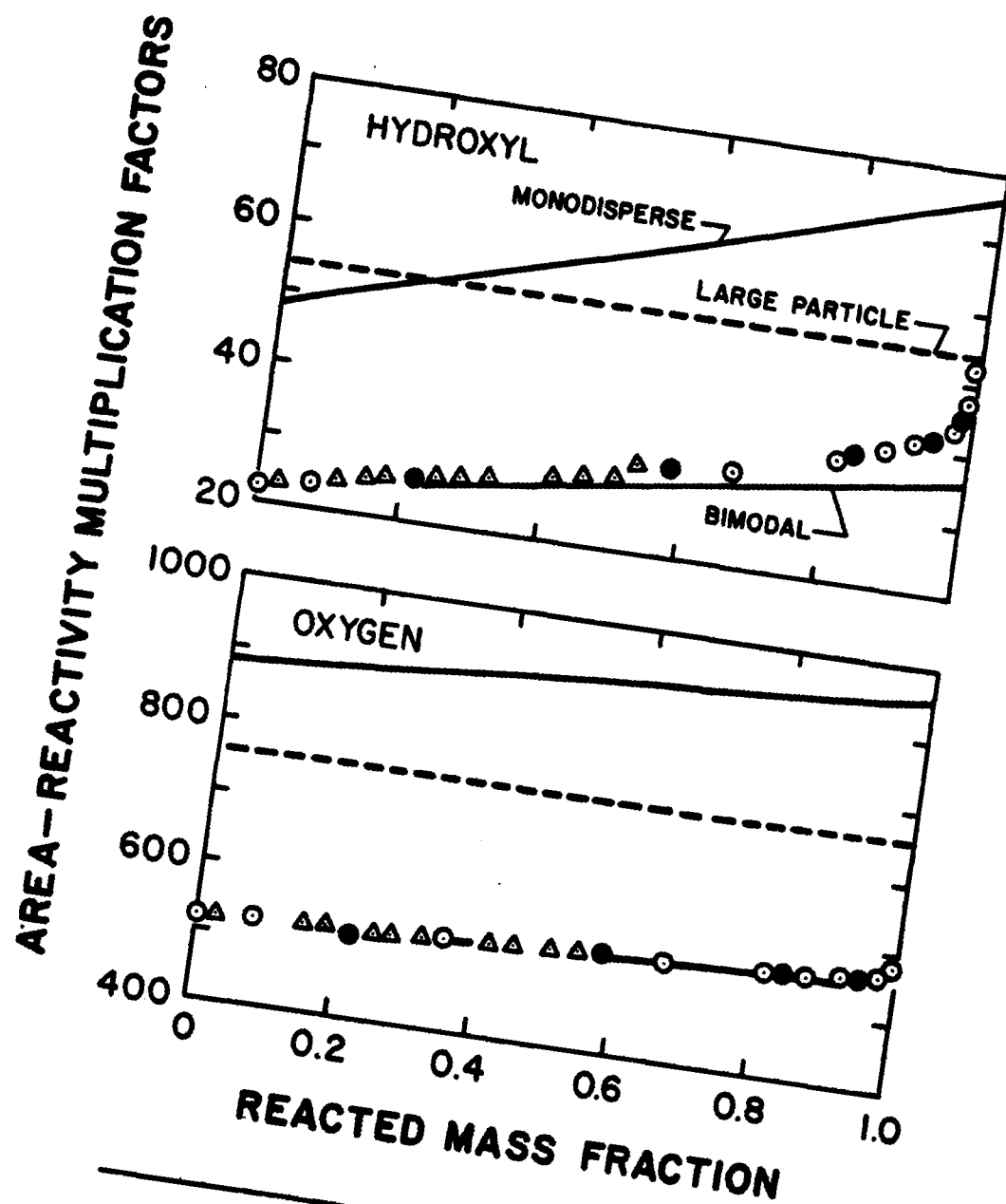
Area/reactivity multiplication factors for the  $O_2$ - $CO_2$ - $H_2O$  reaction mechanism are illustrated in Fig. 47. Results for bimodal agglomerates as well as correlations for the monodisperse agglomerates are shown on the figure. The  $a_1$  are relatively independent of flame conditions and tend to increase somewhat with increasing  $\epsilon$ . The values of the  $a_1$  for the bimodal agglomerates, however, are roughly 50% of the values found for monodisperse agglomerates. Consistent with the lower value of  $\zeta$ , the presence of the small particles appears to impede the development (or extent) of pores, so that less active surface area is available for reaction.

The  $a_1$  for the  $OH$ - $O_2$  reaction mechanism are illustrated in Fig. 48 for the bimodal blends along with the values found for monodisperse agglomerates. As before, the  $a_1$  are independent of flame conditions and tend to increase as  $\epsilon$  increases and the pore layer develops. The  $a_1$  for the bimodal blend are also roughly half the values for monodisperse agglomerates.



	$\phi$	$T_f$ (T)	$d_{p0}$ ( $\mu\text{m}$ )
○	0.6	1663	73.4
●	0.6	1953	73.4
△	1.0	1683	73.4

Figure 47. Area/reactivity multiplication factors for the  $\text{O}_2\text{-CO}_2\text{-H}_2\text{O}$  reaction mechanism for the bimodal agglomerate.



	$\phi$	$T_f$ (K)	$d_{po}$ ( $\mu m$ )
○	0.6	1663	73.5
●	0.6	1953	73.5
△	1.0	1683	73.5

Figure 48. Area/reactivity multiplication factors for the OH-O<sub>2</sub> reaction mechanism for the bimodal agglomerate.

The empirical parameters for the bimodal blends were correlated as functions of  $\epsilon$  and  $d_{po}$ , since effects of flame conditions were small. These correlations are summarized in Table 5. The present data were limited to a single initial agglomerate diameter. Therefore, the effect of  $d_{po}$  has arbitrarily been assumed to be the same as for the monodisperse agglomerates. In addition to the correlations, constant average values of the empirical parameters are listed in Table 5--representative of conditions where  $\epsilon > 0.2$ . The average values found for the monodisperse agglomerates are also summarized in the table for comparison. As noted earlier, empirical parameters for the bimodal blend are roughly 50% as large as the values for monodisperse agglomerates.

#### 4.2.3 Life Histories

The burning rate results for the bimodal agglomerates were similar to the findings for monodisperse agglomerates. Use of the empirical parameters summarized in Table 5 yielded good agreement between predictions and measurements. The use of the constant average values of the parameters resulted in only a slight loss in the accuracy of the predictions.

Particle-life histories for the bimodal agglomerate are illustrated in Figs. 49-51. The variation of particle mass and diameter, normalized by their initial values, and the particle temperature, normalized by the flame temperature, are plotted as a function of time for  $d_{po} = 73.5 \mu\text{m}$ . Predictions of these quantities, for both reaction mechanisms, are also shown on the figures.

Similar to the earlier results, the comparison between predictions and measurements in Figs. 49-51 is reasonably good. Aside from predicting

Table 5. Summary of Agglomerate Structure Parameters (Bimodal Blend)<sup>a</sup>

Factor	Bimodal Agglomerate <sup>b</sup>		Monodisperse Agglomerate <sup>b</sup>	
	Correlation ( $d_p$ in $\mu\text{m}$ )	Mean Value	Correlation ( $d_p$ in $\mu\text{m}$ )	Mean Value
$\rho_p$ ( $\text{kg}/\text{m}^3$ )	2108 $(1 - \epsilon)^{0.6}$	--	--	--
$\zeta$	$1.23 - 0.00858 d_{po} + 9.2 \epsilon - 6.6 \epsilon^2$	3.9		7.5
Neoh et al. Mechanism:				
$a_{OH}$	$39.7 - 0.234 d_{po} + 14.3 \epsilon$	44.4		82.5
$a_{O_2}$	$541.4 - 0.307 d_{po} + 39.6 \epsilon$	566.3		963.0
Extended Libby and Blake Mechanism:				
$a_{O_2}$	$41.3 - 0.206 d_{po} + 11.9 \epsilon$	44.8		82.9
$a_{CO_2}$	$77.4 - 0.290 d_{po} + 22.1 \epsilon$	87.1		156.8
$a_{H_2O}$	$108.5 - 0.513 d_{po} + 25.2 \epsilon$	113.2		205.7

<sup>a</sup> Blend of 70 and 300 nm carbon blacks described in Table 1, 50% each by mass.

<sup>b</sup> Present study, 0-75  $\mu\text{m}$  diameter free particles, particle Reynolds numbers of 0-0.35.

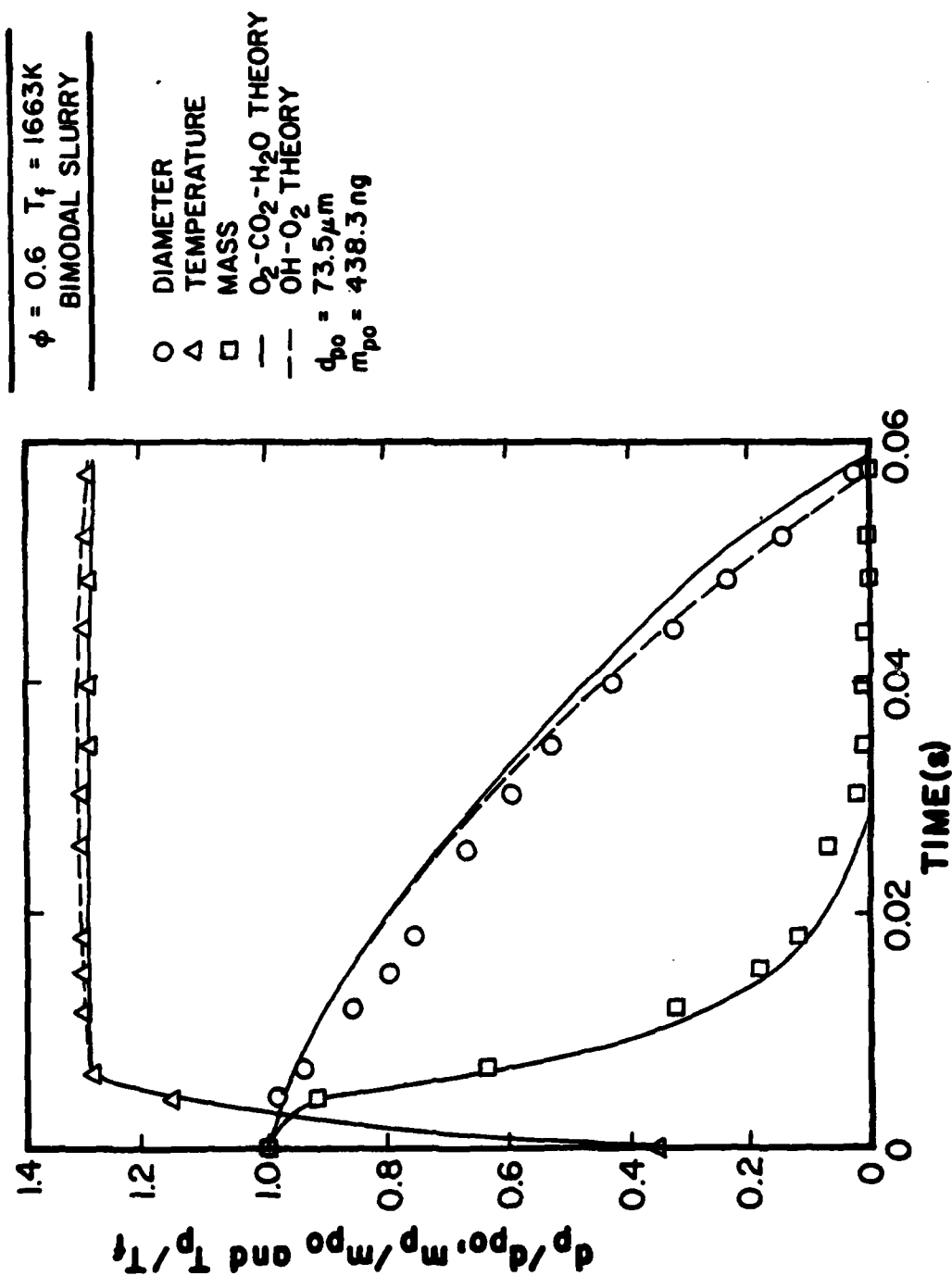


Figure 49. Particle-life history for  $\phi = 0.6$ ,  $T_f = 1663\text{K}$  and  $d_{po} = 73.5\mu\text{m}$  for the bimodal agglomerate.

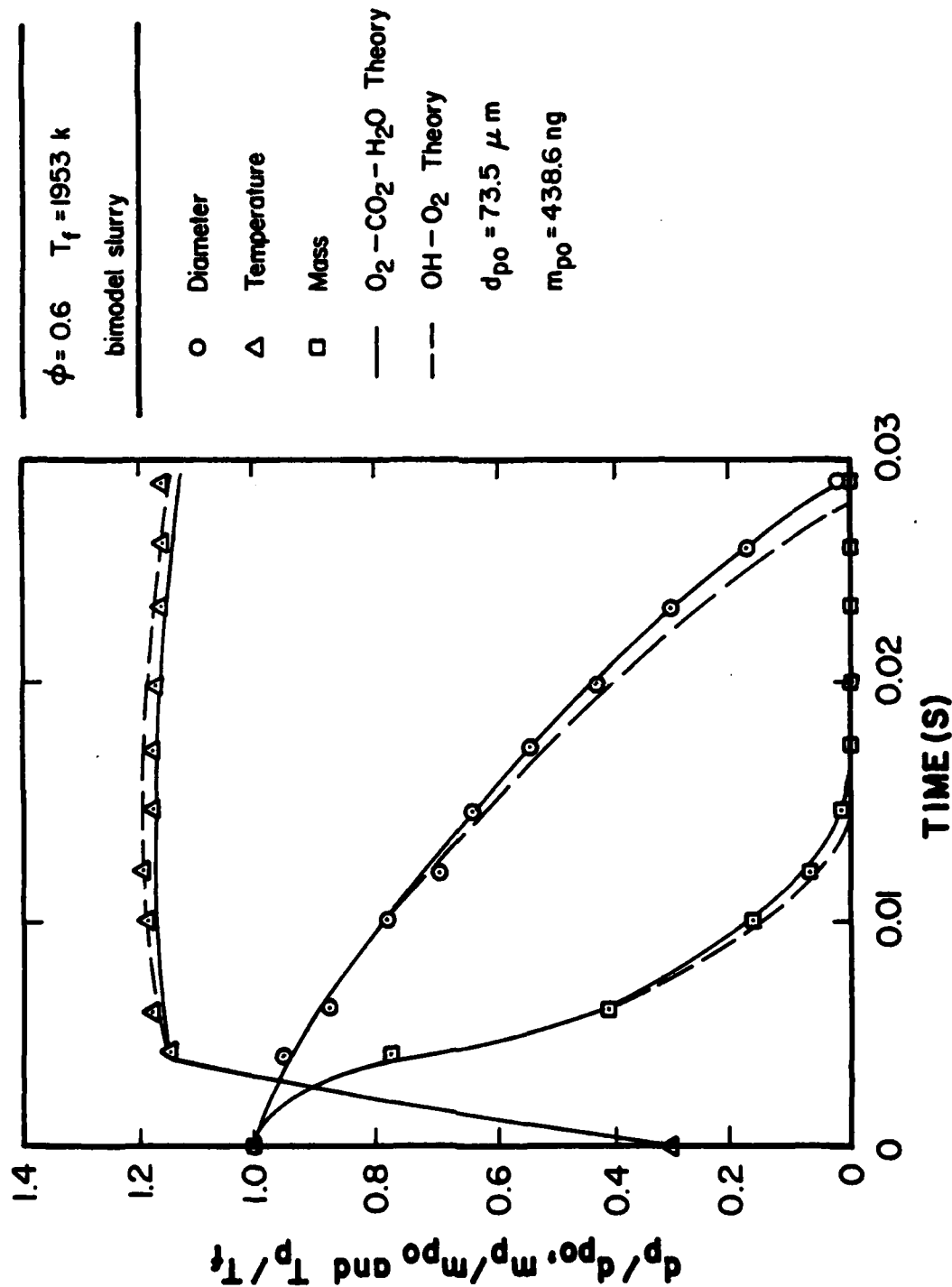


Figure 50. Particle-life history for  $\phi = 0.6$ ,  $T_f = 1953$  K and  $d_{p0} = 73.5 \mu m$  for the bimodal agglomerate.



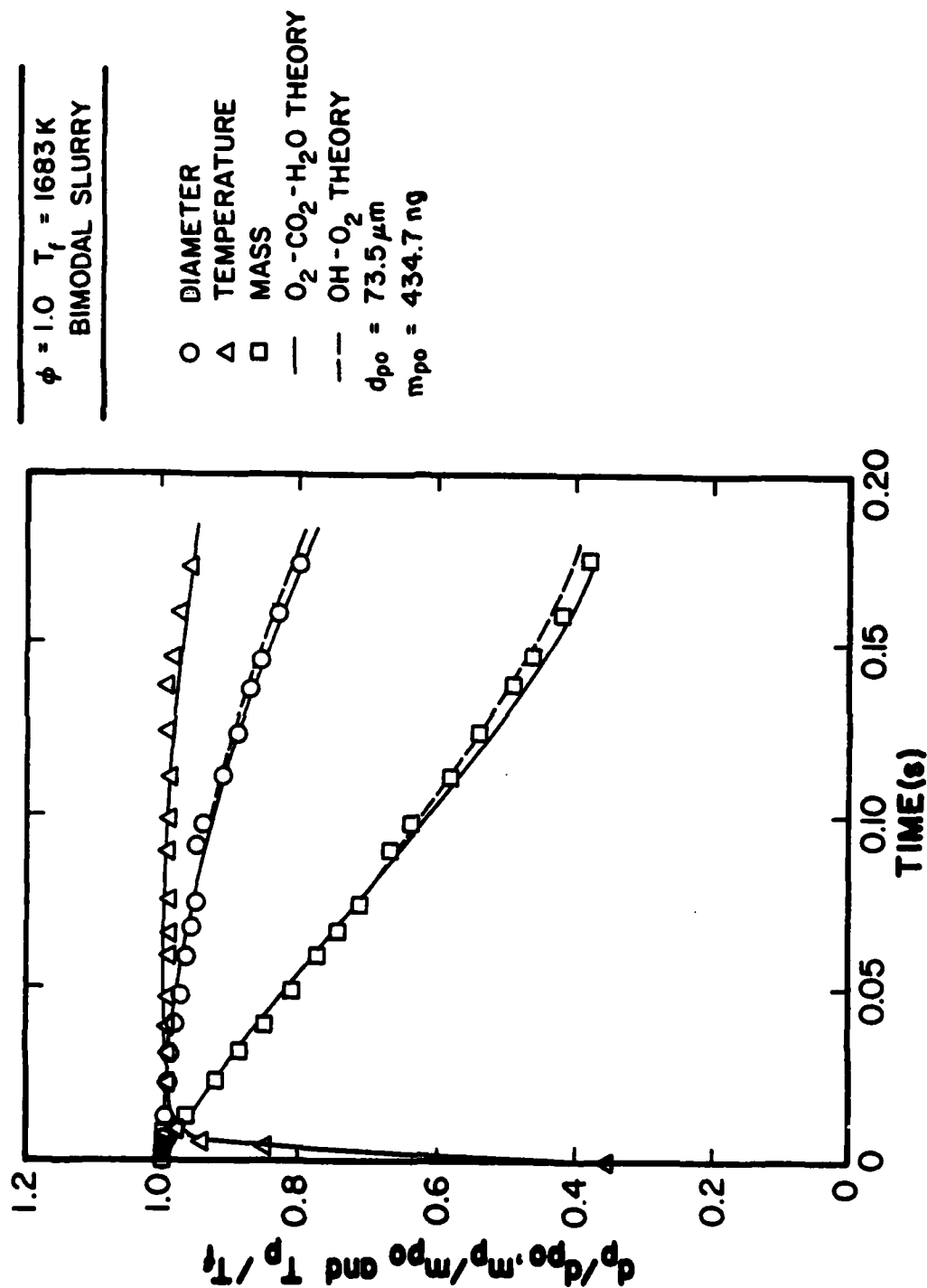


Figure 51. Particle-life history for  $\phi = 1.0$ ,  $T_f = 1683$  K and  $73.5 \mu m$  for the bimodal agglomerate.

burning rates reasonably well, which is expected, the analysis yields good predictions of particle heat-up and maximum temperature levels.

The reduced values of  $\zeta$  and the  $a_1$  for the bimodal agglomerates result in somewhat longer residence times for reaction. Times required to react 60 and 90% of the initial particle mass are summarized in Table 6 for monodisperse agglomerates having  $d_u = 70$  and 300 nm and the bimodal agglomerate employing these constituents. The greatest increase in residence time is observed for the near kinetic-control condition, where  $t_{60\%}$  is nearly 50% longer for the blend than for the monodisperse agglomerates.

The effect of blending is more complex near diffusion-control conditions. The value of  $t_{60\%}$  is 50% longer for the blend, but, the blend seems to catch-up during the latter stages of the process and  $t_{90\%}$  is only 10-20% longer for the blend. Comparing the particle-life histories for the cases in Table 6 provides a clue for this behavior. The agglomerate diameter decreases more slowly for the blend, so that the particle is larger near the end of the process. This compensates for the lower value of  $\zeta$  by providing more apparent surface area.

These results indicate that residence time requirements are somewhat insensitive to changes in  $\zeta$  and the  $a_1$ --except for effects of  $a_1$  near kinetic-controlled conditions. This insensitivity is due to the relative complexity of the reaction mechanism, so that changes in any one parameter tend to be compensated by other aspects of the process.

While the residence times for the bimodal blend are somewhat longer than the monodisperse agglomerates, for a given initial agglomerate size, it should also be recalled that the initial density of the blended agglomerate is 16% greater. This implies that agglomerates of blends will

Table 6. Effect of Blending on Agglomerate Combustion Times<sup>a</sup>

$d_u$ (nm)	$t_{60\%}$ (ms) <sup>b</sup>	$t_{90\%}$ (ms) <sup>b</sup>	Figure No.
$\phi = 0.6$ , $T_f = 1663$ K, mixed condition:			
300	10.0	27.3 (19.4) <sup>c</sup>	20
70	9.1	18.2	34
300/70 (50% each)	12.1	26.0 (20) <sup>c</sup>	49
$\phi = 0.6$ , $T_f = 1953$ K, near diffusion-control:			
300	4.5	10.0	22
70	4.7	9.1	36
300/70 (50% each)	7.0	11.4	50
$\phi = 1.0$ , $T_f = 1683$ K, near kinetic-control:			
300	105	--	23
70	92	--	38
300/70 (50% each)	165	--	51

<sup>a</sup> $d_{po} = 73.5 \mu\text{m}$

<sup>b</sup>Measured times for 60 and 90% consumption of initial agglomerate mass.

<sup>c</sup>Predicted value in parenthesis.

generally be smaller than those of monodisperse carbon blacks, for a given slurry drop mass. Since smaller particles have shorter residence time requirements, this compensates for the somewhat longer residence time requirements of blends. Furthermore, if use of blends improves atomization properties of the slurries, smaller drop sizes could easily yield shorter residence time requirements for blends.

## 5. Conclusions

The present model provided a good correlation of agglomerate reaction rates and life histories using either the Neoh et al. [18] or extended Libby and Blake [17] carbon reaction mechanisms. Combining present and earlier [6,7] results, the test range includes: initial agglomerate diameters of 10-1000  $\mu\text{m}$ , agglomerate Reynolds numbers of 0-200, flame equivalence ratios of 0.2-1.4, C/H ratios (mass basis) of 2.25-3.10 and flame temperatures of 779-1953 K at atmospheric pressure. This agreement is encouraging, removing earlier uncertainties concerning effects of particle size as well as flame temperature and C/H ratio [6,7]. Furthermore, present findings support the conceptually simple carbon reaction mechanism of Neoh et al. [18] at high fuel equivalence ratios.

A shrinking sphere model was used in the analysis which incorporates empirical factors to treat effects of pores on density, enhancement of convective transport, and effective surface area for chemical reactions. The present area/reactivity multiplication factors can also incorporate effects of catalyst [6,7]. The empirical factors were relatively independent of particle size and flame conditions. Particle density decreased monotonically with increasing extent of reaction. Convection enhancement was initially relatively small, but increased as the pore structure developed which allowed the flow to penetrate the porous surface.

Effects of ultimate carbon particle size of the carbon-black, as well as a limited study of effects of blending carbon blacks was also considered. Reducing the ultimate carbon particle size from 300 to 70 nm resulted in slightly higher burning rates, yielding reductions in residence times for particle reaction on the order of 10-20%—depending on flame conditions.

Only a bimodal blend of carbon black having ultimate carbon particle sizes of 70 and 300 nm (50% by weight of each) was considered. This blend had an initial agglomerate density that was 16% higher than the monodisperse agglomerates. Residence times needed to react given fractions of the carbon mass for the blend were longer than for monodisperse agglomerates having the same initial diameter. Residence time increases ranged from 10-20% at diffusion-controlled conditions to 50% at kinetic-controlled conditions. The increased mass of carbon to be reacted in the blend accounts for a portion of this increase. The effect of smaller particles filling void spaces between larger particles, thus inhibiting the development of pores, is probably also a factor contributing to increased residence time requirements for blends. These effects also caused changes in the empirical parameters found for the blends. Transport enhancement and area/reactivity multiplication factors for blends were roughly 50% of the values found for monodisperse agglomerates, indicating some suppression of pore development for blends.

The present results indicate that carbon-black formulation affects agglomerate combustion properties. Use of carbon-blacks having smaller ultimate carbon particle sizes tends to reduce residence time requirements. Blends require somewhat longer residence times for reaction than

monodisperse agglomerates of their constituents--for the same initial agglomerate size. These effects were not large, however, particularly at flame conditions where agglomerate reaction rates were high. Therefore, if blending yields improved atomization properties, the production of smaller drops could easily result in shorter residence time requirements for slurry blends during combustor operation.

Present findings were limited to a single bimodal blend. In order to establish the combustion properties of blends, other ultimate carbon particle sizes and variations in the proportions of each size should be considered. It should also be noted that residence times found here are for fixed ambient conditions, while agglomerates in practical combustors will experience a range of conditions during their lifetimes. The present analysis provides a means of estimating effects of variations in ambient conditions--at least over the range of conditions where it has been evaluated. In particular, evaluation thus far has been limited to atmospheric pressure; therefore, capabilities for predicting effects of pressure are uncertain.

## Appendix A

### Summary of Data

#### A.1 Particle Environment<sup>A</sup>

##### Gas Temperature and Composition, $\phi = 0.2$

x (mm)	T (K)	Mole Fraction						
		O <sub>2</sub>	CO <sub>2</sub>	CO	H <sub>2</sub> O	N <sub>2</sub>	H <sub>2</sub>	OH
10	1667	0.5314	0.0664	--	0.1328	0.2691	--	0.0004
20	1668	0.5314	0.0664	--	0.1328	0.2691	--	0.0004
30	1667	0.5314	0.0664	--	0.1328	0.2691	--	0.0004
40	1667	0.5314	0.0664	--	0.1328	0.2691	--	0.0004
50	1667	0.5314	0.0664	--	0.1328	0.2691	--	0.0004

##### Gas Temperature and Composition, $\phi = 0.6$

x (mm)	T (K)	Mole Fraction						
		O <sub>2</sub>	CO <sub>2</sub>	CO	H <sub>2</sub> O	N <sub>2</sub>	H <sub>2</sub>	OH
5	1662	0.0860	0.0637	--	0.1293	0.7208	--	0.0002
10	1663	0.0858	0.0640	--	0.1291	0.7208	--	0.0003
20	1663	0.0858	0.0644	--	0.1291	0.7208	--	0.0003
30	1664	0.0858	0.0644	--	0.1291	0.7208	--	0.0003
40	1663	0.0858	0.0644	--	0.1291	0.7208	--	0.0003
50	1664	0.0858	0.0644	--	0.1291	0.7208	--	0.0003

<sup>A</sup>OH mole fraction was obtained from CEC-72 equilibrium calculation.  
H<sub>2</sub>O mole fraction was obtained from H and O element balances.

Gas Temperature and Composition,  $\phi = 0.6$

x (mm)	T (K)	Mole Fraction						
		O <sub>2</sub>	CO <sub>2</sub>	CO	H <sub>2</sub> O	N <sub>2</sub>	H <sub>2</sub>	OH
10	1810	0.0973	0.0730	0.0001	0.1458	0.6832	--	0.0007
20	1814	0.0973	0.0730	0.0001	0.1458	0.6832	--	0.0007
30	1815	0.0973	0.0730	0.0001	0.1458	0.6832	--	0.0007
40	1814	0.0973	0.0730	0.0001	0.1458	0.6832	--	0.0007
50	1814	0.0973	0.0730	0.0001	0.1458	0.6832	--	0.0007

Gas Temperature and Composition,  $\phi = 0.6$

x (mm)	T (K)	Mole Fraction						
		O <sub>2</sub>	CO <sub>2</sub>	CO	H <sub>2</sub> O	N <sub>2</sub>	H <sub>2</sub>	OH
10	1952	0.1096	0.0822	0.0002	0.1639	0.6425	0.0001	0.0017
20	1954	0.1095	0.0821	0.0002	0.1641	0.6425	0.0001	0.0017
30	1953	0.1096	0.0822	0.0002	0.1639	0.6425	0.0001	0.0017
40	1953	0.1096	0.0822	0.0002	0.1639	0.6425	0.0001	0.0017
50	1953	0.1095	0.0822	0.0002	0.1640	0.6425	0.0001	0.0017



Gas Temperature and Composition,  $\phi = 1.0$

x (mm)	T (K)	Mole Fraction						
		O <sub>2</sub>	CO <sub>2</sub>	CO	H <sub>2</sub> O	N <sub>2</sub>	H <sub>2</sub>	OH
5	1683	0.0002	0.0645	0.0003	0.1295	0.8054	0.0002	0.0001
10	1683	0.0002	0.0645	0.0003	0.1294	0.8054	0.0002	0.0001
20	1684	0.0002	0.0645	0.0003	0.1294	0.8054	0.0002	0.0001
30	1683	0.0002	0.0645	0.0003	0.1295	0.8054	0.0002	0.0001
40	1683	0.0002	0.0645	0.0003	0.1295	0.8054	0.0002	0.0001
50	1683	0.0002	0.0645	0.0003	0.1295	0.8054	0.0002	0.0001
60	1683	0.0002	0.0645	0.0003	0.1295	0.8054	0.0002	0.0001
70	1681	0.0002	0.0645	0.0003	0.1295	0.8054	0.0002	0.0001
80	1678	0.0002	0.0646	0.0003	0.1295	0.8054	0.0002	0.0001
90	1675	0.0002	0.0646	0.0002	0.1295	0.8054	0.0002	0.0001
100	1668	0.0002	0.0646	0.0002	0.1295	0.8054	0.0002	0.0001
110	1665	0.0002	0.0646	0.0002	0.1295	0.8054	0.0002	0.0001
120	1661	0.0002	0.0646	0.0002	0.1295	0.8054	0.0001	0.0001
130	1657	0.0002	0.0646	0.0002	0.1295	0.8054	0.0001	0.0001
140	1648	0.0002	0.0646	0.0002	0.1295	0.8054	0.0001	0.0001
150	1640	0.0001	0.0646	0.0002	0.1295	0.8055	0.0001	0.0001
160	1625	0.0001	0.0646	0.0002	0.1295	0.8055	0.0001	0.0
170	1606	0.0001	0.0647	0.0001	0.1295	0.8055	0.0001	0.0
180	1597	0.0001	0.0647	0.0001	0.1295	0.8055	0.0001	0.0
190	1578	0.0001	0.0647	0.0001	0.1296	0.8055	0.0001	0.0
200	1564	0.0001	0.0647	0.0001	0.1296	0.8055	0.0001	0.0

Gas Temperature and Composition,  $\phi = 1.0$

x (mm)	T (K)	Mole Fraction						
		O <sub>2</sub>	CO <sub>2</sub>	CO	H <sub>2</sub> O	N <sub>2</sub>	H <sub>2</sub>	OH
10	1816	0.0005	0.0722	0.0008	0.1455	0.7805	0.0004	0.0002
20	1819	0.0005	0.0722	0.0008	0.1455	0.7805	0.0004	0.0002
30	1819	0.0005	0.0722	0.0008	0.1455	0.7805	0.0004	0.0002
40	1820	0.0005	0.0722	0.0008	0.1455	0.7805	0.0004	0.0002
50	1819	0.0005	0.0722	0.0008	0.1455	0.7805	0.0004	0.0002
60	1819	0.0005	0.0722	0.0008	0.1455	0.7805	0.0004	0.0002
70	1817	0.0005	0.0722	0.0008	0.1455	0.7805	0.0004	0.0002
80	1817	0.0005	0.0722	0.0008	0.1455	0.7805	0.0004	0.0002
90	1815	0.0005	0.0722	0.0008	0.1455	0.7805	0.0004	0.0002
100	1812	0.0005	0.0722	0.0008	0.1455	0.7805	0.0004	0.0002
110	1809	0.0005	0.0722	0.0007	0.1456	0.7806	0.0004	0.0002
120	1805	0.0005	0.0723	0.0007	0.1455	0.7806	0.0004	0.0002
130	1801	0.0005	0.0723	0.0007	0.1455	0.7806	0.0004	0.0002
140	1793	0.0005	0.0723	0.0006	0.1456	0.7806	0.0003	0.0002
150	1785	0.0009	0.0724	0.0006	0.1456	0.7806	0.0003	0.0002
160	1773	0.0004	0.0724	0.0006	0.1457	0.7806	0.0003	0.0001
170	1754	0.0004	0.0725	0.0005	0.1456	0.7807	0.0003	0.0001
180	1742	0.0003	0.0725	0.0004	0.1458	0.7807	0.0003	0.0001
190	1730	0.0003	0.0726	0.0004	0.1457	0.7808	0.0002	0.0001
200	1718	0.0003	0.0726	0.0004	0.1457	0.7808	0.0002	0.0001

Gas Temperature and Composition,  $\phi = 1.0$

x (mm)	T (K)	Mole Fraction						
		O <sub>2</sub>	CO <sub>2</sub>	CO	H <sub>2</sub> O	N <sub>2</sub>	H <sub>2</sub>	OH
10	1949	0.0013	0.0806	0.0019	0.1641	0.7509	0.0009	0.0006
20	1952	0.0013	0.0806	0.0020	0.1641	0.7509	0.0009	0.0006
30	1953	0.0013	0.0806	0.0020	0.1641	0.7509	0.0009	0.0006
40	1952	0.0013	0.0806	0.0020	0.1641	0.7509	0.0009	0.0006
50	1952	0.0013	0.0806	0.0020	0.1641	0.7509	0.0009	0.0006
60	1951	0.0013	0.0806	0.0019	0.1642	0.7509	0.0009	0.0006
70	1950	0.0013	0.0806	0.0019	0.1642	0.7509	0.0009	0.0006
80	1948	0.0013	0.0806	0.0019	0.1642	0.7509	0.0009	0.0006
90	1946	0.0012	0.0806	0.0019	0.1644	0.7509	0.0009	0.0005
100	1944	0.0012	0.0807	0.0019	0.1643	0.7509	0.0009	0.0005
110	1940	0.0012	0.0807	0.0018	0.1643	0.7510	0.0009	0.0005
120	1935	0.0012	0.0808	0.0018	0.1643	0.7510	0.0008	0.0005
130	1930	0.0011	0.0808	0.0017	0.1644	0.7510	0.0009	0.0005
140	1924	0.0011	0.0809	0.0016	0.1644	0.7511	0.0008	0.0005
150	1913	0.0010	0.0810	0.0015	0.1745	0.7511	0.0007	0.0004
160	1901	0.0010	0.0811	0.0014	0.1645	0.7512	0.0007	0.0004
170	1891	0.0009	0.0812	0.0013	0.1645	0.7512	0.0007	0.0004
180	1879	0.0008	0.0813	0.0012	0.1647	0.0006	0.0006	0.0003
190	1860	0.0008	0.0814	0.0011	0.1647	0.7514	0.0006	0.0003
200	1851	0.0007	0.815	0.0010	0.1648	0.7614	0.0006	0.0003

Gas Temperature and Composition,  $\phi = 1.4$

x (mm)	T (K)	Mole Fraction						OH
		O <sub>2</sub>	CO <sub>2</sub>	CO	H <sub>2</sub> O	N <sub>2</sub>	H <sub>2</sub>	
5	1622	--	0.0421	0.0534	0.1432	0.7092	0.0542	--
10	1624	--	0.0427	0.0540	0.1412	0.7092	0.0563	--
20	1625	--	0.0428	0.0542	0.1409	0.7092	0.0566	--
30	1625	--	0.0428	0.0543	0.1408	0.7092	0.0566	--
40	1624	--	0.0427	0.0542	0.1409	0.7092	0.0566	--
50	1624	--	0.0427	0.0541	0.1410	0.7092	0.0566	--
60	1624	--	0.0428	0.0541	0.1410	0.7092	0.0567	--
70	1621	--	0.0428	0.0541	0.1410	0.7092	0.0566	--
80	1620	--	0.0429	0.0541	0.1408	0.7092	0.0566	--
90	1618	--	0.0430	0.0541	0.1407	0.7092	0.0567	--
100	1612	--	0.0430	0.0540	0.1407	0.7092	0.0568	--
110	1609	--	0.0430	0.0540	0.1406	0.7092	0.0569	--
120	1604	--	0.0431	0.0538	0.1406	0.7092	0.0569	--
130	1601	--	0.0432	0.0537	0.1405	0.7092	0.0571	--
140	1594	--	0.0434	0.0536	0.1403	0.7092	0.0572	--
150	1589	--	0.0435	0.0535	0.1402	0.7092	0.0573	--
160	1570	--	0.0439	0.0532	0.1397	0.7092	0.0577	--
170	1557	--	0.0442	0.0529	0.1394	0.7092	0.0580	--
180	1543	--	0.0444	0.0525	0.1393	0.7092	0.0583	--
190	1522	--	0.0449	0.0520	0.1388	0.7092	0.0588	--
200	1507	--	0.0450	0.0519	0.1387	0.7092	0.0589	--

# A.2 Agglomerates of Monodisperse Particles, $d_u = 300 \text{ nm}$

Particle-Life History,  $\phi = 0.2$ ,  $T_f \approx 1667 \text{ K}$

x (mm)	$d_p$ ( $\mu\text{m}$ )	$m_p$ (ng)	$T_p$ (K)	Reacted Mass Fraction	Apparent Density ( $\text{kg/m}^3$ )	$u_p$ (m/s)	$u_{\infty}$ with Particles Present (m/s)	$u_{\infty}$ without Particles Present (m/s)
0.0	73.4	377.3	604	0.0	1822.2	0.349	0.623	1.478
0.6	73.2	368.5	1267	0.023	1794.3	0.467	0.749	1.494
2.5	66.0	169.6	1451	0.550	1126.7	0.504	0.842	1.510
3.9	60.8	91.7	1559	0.757	779.2	0.526	0.940	1.526
6.0	53.5	35.1	1574	0.907	437.8	0.601	1.038	1.543
7.5	48.7	17.4	1589	0.954	287.7	0.673	1.135	1.559
9.6	42.2	5.95	1597	0.984	151.2	0.723	1.233	1.575
12.9	35.0	1.456	1606	0.996	64.9	0.830	1.323	1.614
13.4	31.1	0.599	1614	0.998	38.0	0.994	1.412	1.654
16.0	24.1	0.089	1617	1.000	12.1	1.049	1.503	1.693
18.1	18.6	0.0133	1619	1.000	3.9	1.132	1.595	1.733
20.2	13.6	0.00123	1625	1.000	0.9	1.242	1.686	1.772
21.9	10.2	0.000144	1630	1.000	0.3	1.407	1.779	1.825
24.2	6.3	0.0000042	1633	1.000	0.03	1.555	1.861	1.877
26.1	3.6	0.000001	1645	1.000	0.041	1.739	1.924	1.930
27.9	1.2	0.0	1657	1.000	0.0	1.972	1.976	1.983

Particle-Life History,  $\phi = 0.6$ ,  $T_f = 1663$  K

x (nm)	$d_p$ ( $\mu\text{m}$ )	$m_p$ (ng)	$T_p$ (K)	Reacted Mass Fraction	Apparent Density ( $\text{kg/m}^3$ )	$u_p$ (m/s)	$u_{\infty}$ with Particles Present (m/s)	$u_{\infty}$ without Particles Present (m/s)
0.0	73.4	377.5	595	0.0	1823.2	0.439	0.613	1.513
2.6	70.6	293.3	2067	0.223	1591.8	0.476	0.707	1.521
3.8	67.6	193.3	2075	0.488	1195.1	0.479	0.839	1.557
5.9	62.2	131.2	2087	0.652	1041.3	0.483	0.942	1.563
7.5	59.0	96.3	2095	0.745	895.5	0.492	1.053	1.597
9.5	54.2	62.5	2100	0.834	749.7	0.501	1.172	1.631
11.8	48.9	37.0	2112	0.902	604.3	0.521	1.253	1.664
13.3	44.7	19.5	2120	0.948	416.7	0.539	1.342	1.697
15.9	38.7	11.4	2112	0.970	375.6	0.551	1.421	1.731
18.2	33.0	6.03	2133	0.984	320.5	0.581	1.497	1.765
19.9	29.5	3.64	2134	0.990	270.8	0.597	1.573	1.799
20.6	26.9	2.34	2145	0.994	229.6	0.657	1.684	1.832
21.7	23.9	1.55	2141	0.996	216.8	0.685	1.762	1.864
23.4	19.8	0.752	2132	0.998	185.0	0.782	1.821	1.887
24.1	17.6	0.333	2139	0.9991	116.7	0.811	1.871	1.903
26.1	12.4	0.0059	2128	0.99998	5.91	0.932	1.918	1.925
27.6	7.65	$2 \times 10^{-6}$	2126	1.0	0.0085	0.949	1.943	1.949
29.0	4.01	0.0	2110	1.0	0.0	1.007	1.960	1.963
29.5	1.62	0.0	2051	1.0	0.0	1.974	1.975	1.979

Particle-Life History,  $\phi = 0.6$ ,  $T_f = 1814$  K

x (mm)	d <sub>p</sub> ( $\mu$ m)	m <sub>p</sub> (ng)	T <sub>p</sub> (K)	Reacted Mass Fraction	Apparent Density (kg/m <sup>3</sup> )	u <sub>p</sub> (m/s)	u <sub>∞</sub> with Particles Present (m/s)	u <sub>∞</sub> without Particles Present (m/s)
0.0	73.4	377.1	601	0.000	1821.3	0.298	0.404	1.521
2.2	69.2	211.5	2166	0.439	1219.0	0.637	0.753	1.536
3.3	65.9	128.6	2174	0.659	858.2	0.711	0.842	1.550
4.7	61.9	68.6	2182	0.818	552.4	0.777	1.132	1.565
5.5	59.7	47.8	2187	0.873	429.0	0.797	1.195	1.579
7.6	52.6	13.4	2193	0.969	175.9	0.822	1.258	1.594
9.6	46.2	3.68	2195	0.990	71.3	0.839	1.321	1.608
11.7	39.8	0.827	2197	0.998	25.1	0.852	1.384	1.623
13.2	35.5	0.266	2199	0.999	11.4	1.001	1.467	1.663
16.1	27.4	0.0198	2202	1.000	1.8	1.025	1.551	1.705
18.3	21.3	0.00160	2205	1.0	0.316	1.199	1.634	1.743
20.1	16.8	0.00015	2210	1.0	0.0604	1.387	1.721	1.784
21.3	13.9	0.000023	2213	1.0	0.0164	1.442	1.814	1.857
23.2	9.1	0.0000005	2208	1.0	0.00126	1.489	1.884	1.929
24.1	6.9	0.0000003	2174	1.0	0.0	1.544	1.967	2.002
26.2	2.3	0.0000001	2127	1.0	0.0	1.902	2.052	2.074
27.1	0.4	0.0	2012	1.0	0.0	2.131	2.139	2.147

Particle-Life History,  $\phi = 0.6$ ,  $T_f \approx 1953$  K

x (nm)	d <sub>p</sub> ( $\mu$ m)	m <sub>p</sub> (ng)	T <sub>p</sub> (K)	Reacted Mass Fraction	Apparent Density (kg/m <sup>3</sup> )	u <sub>p</sub> (m/s)	u <sub>∞</sub> with Particles Present (m/s)	u <sub>∞</sub> without Particles Present (m/s)
0.0	73.4	377.1	603	0.0	1821.3	0.259	0.352	1.464
0.7	72.8	288.6	1828	0.235	1428.6	0.462	0.729	1.501
1.5	69.6	195.5	2233	0.482	1107.4	0.551	0.814	1.518
2.4	65.4	125.5	2246	0.667	856.9	0.632	0.924	1.534
3.4	61.4	98.0	2255	0.740	808.6	0.707	0.977	1.551
4.2	58.2	73.6	2264	0.805	713.0	0.764	1.023	1.568
5.0	55.1	56.2	2272	0.851	641.6	0.782	1.124	1.582
6.0	51.4	40.3	2281	0.893	566.8	0.807	1.246	1.596
7.0	47.8	28.6	2286	0.924	500.1	0.887	1.332	1.610
8.0	44.4	21.7	2289	0.942	473.5	0.913	1.417	1.625
9.0	41.0	15.3	2291	0.959	424.0	0.951	1.502	1.639
10.0	37.8	11.2	2290	0.970	396.0	1.072	1.587	1.653
12.0	31.6	6.01	2289	0.984	363.2	1.115	1.638	1.691
14.0	25.7	3.06	2288	0.992	344.3	1.312	1.689	1.728
16.0	20.0	1.31	2287	0.997	312.7	1.348	1.729	1.753
18.0	14.6	0.475	2276	0.999	291.5	1.645	1.759	1.778
20.0	9.3	0.0191	2231	1.000	45.4	1.702	1.827	1.853
22.0	4.1	0.00016	2195	1.000	4.4	1.883	2.111	2.111
24.0	0.9	0.0	2122	1.000	0.0	2.213	2.416	2.419



Particle-Life History,  $\phi = 1.0$ ,  $T_f \approx 1683$  K

x (mm)	$d_p$ ( $\mu\text{m}$ )	$m_p$ (ng)	$T_p$ (K)	Reacted Mass Fraction	Apparent density ( $\text{kg}/\text{m}^3$ )	$u_p$ (m/s)	$u_{\infty}$ with Particles Present (m/s)	$u_{\infty}$ without Particles Present (m/s)
0.0	73.4	377.1	608	0.000	1821.3	0.439	0.527	1.487
1.9	73.4	373.8	1515	0.0087	1805.3	0.583	0.721	1.508
2.7	73.3	366.2	1601	0.0289	1775.9	0.614	0.854	1.529
4.3	73.2	357.4	1645	0.522	1740.3	0.665	0.984	1.548
5.6	73.0	344.2	1656	0.872	1689.8	0.702	1.111	1.572
8.1	72.8	331.0	1660	0.122	1638.5	0.765	1.196	1.592
15.7	72.1	307.5	1661	0.185	1566.9	0.904	1.281	1.690
21.0	71.7	289.5	1660	0.232	1500.0	0.904	1.368	1.799
30.3	71.1	265.3	1661	0.296	1409.7	1.068	1.459	1.901
41.4	70.3	241.2	1661	0.360	1325.9	1.147	1.538	1.970
52.8	69.6	219.4	1661	0.418	1242.8	1.204	1.621	2.051
63.4	68.9	202.7	1661	0.462	1183.6	1.244	1.678	2.129
77.4	68.2	177.2	1660	0.530	1066.9	1.283	1.750	2.209
88.8	67.5	162.3	1661	0.570	1007.9	1.307	1.818	2.288
100.4	66.8	153.0	1661	0.594	980.3	1.343	1.895	2.364
121.1	65.6	140.1	1661	0.628	947.8	1.408	1.952	2.413
138.7	64.6	130.0	1660	0.655	921.0	1.417	2.018	2.460
154.2	63.7	123.2	1661	0.673	910.3	1.429	2.083	2.508
170.9	62.8	113.5	1660	0.699	875.2	1.521	2.148	2.563
184.3	62.1	109.1	1658	0.711	870.1	1.552	2.214	2.613
200.4	61.3	103.1	1651	0.727	854.8	1.558	2.232	2.658

Particle-Life History,  $\psi = 1.0$ ,  $T_f \approx 1683$  K

x (mm)	d <sub>p</sub> ( $\mu$ m)	m <sub>p</sub> (ng)	T <sub>p</sub> (K)	Reacted Mass Fraction	Apparent Density (kg/m <sup>3</sup> )	u <sub>p</sub> (m/s)	u <sub>∞</sub> with Particles Present (m/s)	u <sub>∞</sub> without Particles Present (m/s)
0.0	52.6	138.4	603	0.000	1816.3	0.464	0.578	1.489
1.8	52.6	137.1	1630	0.0094	1799.2	0.675	0.759	1.501
3.1	52.4	134.0	1665	0.0318	1778.7	0.752	0.942	1.534
4.1	52.3	128.8	1667	0.0694	1719.5	0.806	0.997	1.546
5.7	52.2	123.8	1667	0.105	1662.3	0.873	1.143	1.574
8.3	51.9	119.6	1667	0.136	1633.9	0.968	1.250	1.599
15.1	51.5	111.7	1668	0.193	1561.8	1.131	1.358	1.682
20.7	51.1	104.4	1667	0.246	1494.3	1.221	1.463	1.782
30.2	50.5	95.3	1667	0.311	1413.3	1.324	1.575	1.894
41.9	49.9	86.2	1668	0.377	1325.0	1.400	1.678	1.982
51.7	49.4	77.6	1667	0.439	1229.4	1.442	1.750	2.043
63.7	48.7	71.0	1666	0.487	1174.0	1.475	1.825	2.128
74.5	48.2	61.9	1667	0.553	1055.7	1.495	1.901	2.178
86.1	47.6	56.5	1668	0.592	1000.5	1.509	1.992	2.257
100.9	46.8	52.1	1668	0.624	970.7	1.521	2.054	2.369
118.7	45.9	47.6	1668	0.656	940.1	1.530	2.130	2.407
135.6	45.1	44.1	1667	0.681	918.1	1.542	2.207	2.452
151.2	44.3	39.7	1667	0.713	872.1	1.557	2.282	2.499
168.9	43.4	35.4	1666	0.744	827.1	1.584	2.354	2.532
183.2	42.6	31.5	1664	0.772	778.2	1.597	2.402	2.606
199.1	41.8	26.5	1662	0.809	693.0	1.602	2.427	2.654

Particle-Life History,  $\phi = 1.0$ ,  $T_f \approx 1683$  K

x (mm)	d <sub>p</sub> ( $\mu$ m)	m <sub>p</sub> (ng)	T <sub>p</sub> (K)	Reacted Mass Fraction	Apparent Density (kg/m <sup>3</sup> )	u <sub>p</sub> (m/s)	u <sub>∞</sub> with Particles Present (m/s)	u <sub>∞</sub> without Particles Present (m/s)
0.0	28.7	22.5	600	0.000	1817.8	0.562	0.592	1.485
1.8	28.6	22.1	1670	0.0178	1804.2	0.952	1.154	1.501
3.2	28.5	21.8	1674	0.0311	1789.6	1.096	1.212	1.518
4.1	28.4	20.5	1674	0.0889	1709.2	1.168	1.347	1.542
5.7	28.3	19.7	1674	0.124	1660.0	1.263	1.479	1.568
8.3	28.1	18.8	1675	0.164	1618.2	1.372	1.521	1.598
15.1	27.8	17.7	1674	0.213	1573.4	1.523	1.632	1.682
20.8	27.5	16.2	1675	0.280	1487.7	1.581	1.652	1.797
30.2	27.0	14.6	1675	0.351	1416.7	1.622	1.684	1.900
38.0	26.6	12.9	1675	0.427	1309.0	1.636	1.705	1.949
49.3	26.0	11.2	1675	0.502	1217.0	1.642	1.800	2.026
61.2	25.4	10.0	1675	0.556	1165.5	1.651	1.893	2.113
74.5	24.8	8.42	1676	0.626	1054.3	1.663	1.987	2.181
86.1	24.2	7.44	1675	0.669	1002.6	1.675	2.079	2.254
100.9	23.5	5.71	1675	0.746	840.3	1.684	2.173	2.332
118.7	22.7	4.21	1676	0.813	687.4	1.697	2.266	2.394
135.6	21.9	3.11	1676	0.862	565.5	1.703	2.359	2.497
151.2	21.2	2.21	1676	0.902	443.0	1.711	2.449	2.486
168.7	20.4	1.58	1677	0.930	355.4	1.719	2.482	2.551
183.3	19.7	1.10	1677	0.951	274.8	1.727	2.506	2.601
199.7	19.0	0.80	1677	0.964	222.8	1.735	2.531	2.656

Particle-Life History,  $\phi = 1.0$ ,  $T_f \approx 1683$  K

x (mm)	d <sub>p</sub> ( $\mu$ m)	m <sub>p</sub> (ng)	T <sub>p</sub> (K)	Reacted Mass Fraction	Apparent Density (kg/m <sup>3</sup> )	u <sub>p</sub> (m/s)	u <sub>∞</sub> with Particles Present (m/s)	u <sub>∞</sub> without Particles Present (m/s)
0.0	10.5	1.10	602	0.000	1814.8	0.601	0.942	1.487
1.8	10.4	1.04	1680	0.0545	1765.8	1.387	1.487	1.502
3.2	10.3	1.01	1680	0.0818	1765.3	1.428	1.499	1.516
4.1	10.3	0.983	1680	0.106	1718.1	1.487	1.529	1.542
5.7	10.2	0.954	1680	0.133	1716.9	1.516	1.551	1.576
6.5	10.1	0.899	1680	0.183	1666.5	1.542	1.583	1.597
8.3	10.0	0.847	1680	0.230	1617.7	1.639	1.661	1.682
15.1	9.7	0.748	1680	0.320	1565.3	1.758	1.783	1.792
20.8	9.4	0.621	1680	0.435	1427.9	1.868	1.887	1.901
30.2	9.0	0.540	1681	0.509	1414.7	1.941	1.958	1.965
41.0	8.6	0.416	1680	0.622	1249.1	2.014	2.024	2.031
51.3	8.3	0.343	1680	0.688	1145.7	2.027	2.032	2.040
61.2	7.9	0.278	1680	0.747	1076.9	2.101	2.109	2.113
74.5	7.6	0.227	1680	0.794	987.6	2.200	2.208	2.211
86.1	7.4	0.205	1680	0.814	966.2	2.258	2.265	2.269
100.7	7.2	0.187	1681	0.830	956.9	2.361	2.368	2.370
118.7	6.9	0.153	1680	0.861	889.5	2.398	2.404	2.407
136.7	6.7	0.117	1680	0.894	743.0	2.444	2.448	2.452
151.0	6.6	0.0932	1681	0.915	619.1	2.480	2.484	2.489
168.4	6.3	0.0640	1681	0.942	488.8	2.543	2.548	2.551
184.1	6.1	0.0377	1681	0.966	317.2	2.597	2.608	2.611
199.8	5.9	0.0223	1681	0.980	207.4	2.614	2.643	2.654

Particle-Life History,  $\phi = 1.0$ ,  $T_f \approx 1819$  K

x (mm)	$d_p$ ( $\mu\text{m}$ )	$m_p$ (ng)	$T_p$ (K)	Reacted Mass Fraction	Apparent Density ( $\text{kg}/\text{m}^3$ )	$u_p$ (m/s)	$u_{\infty}$ with Particles Present (m/s)	$u_{\infty}$ without Particles Present (m/s)
0.0	73.4	377.4	606	0.000	1822.7	0.299	0.413	1.513
1.9	73.2	365.5	1717	0.032	1779.7	0.479	0.767	1.533
3.0	72.9	350.8	1763	0.070	1729.3	0.533	0.851	1.553
4.4	72.4	327.7	1768	0.132	1649.2	0.589	1.097	1.572
7.5	71.6	293.1	1768	0.223	1525.0	0.687	1.185	1.594
10.6	70.8	261.7	1769	0.307	1408.3	0.765	1.274	1.612
13.7	70.0	233.8	1769	0.380	1301.8	0.829	1.363	1.677
17.1	69.3	211.7	1769	0.439	1214.8	0.889	1.451	1.748
22.4	68.3	182.6	1770	0.516	1094.6	0.962	1.539	1.814
30.3	66.8	146.8	1771	0.611	940.6	1.051	1.663	1.920
39.7	65.2	115.3	1771	0.694	794.5	1.128	1.783	2.030
50.2	63.5	88.7	1772	0.765	661.6	1.193	1.912	2.134
62.1	61.7	66.8	1773	0.823	543.2	1.249	2.036	2.211
75.6	59.7	47.5	1774	0.874	426.4	1.297	2.092	2.285
89.3	57.8	34.3	1775	0.909	339.2	1.495	2.160	2.360
100.4	56.3	26.4	1775	0.930	282.5	1.542	2.226	2.432
120.7	53.8	16.9	1776	0.955	207.3	1.632	2.292	2.467
139.2	51.6	11.4	1777	0.970	158.5	1.700	2.359	2.507
161.3	49.1	6.74	1778	0.982	108.7	1.741	2.427	2.548
180.4	47.0	4.37	1775	0.988	80.4	1.860	2.494	2.591
200.2	45.1	2.88	1771	0.992	60.0	2.183	2.549	2.625

Particle-Life History,  $\phi = 1.0$ ,  $T_f \approx 1952$  K

x (mm)	d <sub>p</sub> ( $\mu$ m)	m <sub>p</sub> (ng)	T <sub>p</sub> (K)	Reacted Mass Fraction	Apparent Density (kg/m <sup>3</sup> )	u <sub>p</sub> (m/s)	u <sub>∞</sub> with Particles Present (m/s)	u <sub>∞</sub> without Particles Present (m/s)
0.0	73.4	376.9	599	0.0	1820.3	0.260	0.304	1.543
1.9	72.7	323.2	1848	0.142	1606.5	0.45	0.561	1.567
2.6	72.2	300.6	1855	0.202	1525.4	0.487	0.784	1.582
4.4	71.0	252.9	1857	0.329	1349.5	0.564	0.997	1.618
5.7	70.2	227.1	1858	0.397	1253.7	0.611	1.142	1.645
8.2	68.8	189.0	1859	0.499	1108.4	0.687	1.232	1.665
15.8	65.1	133.2	1862	0.647	922.1	0.858	1.396	1.812
24.2	61.7	108.2	1865	0.713	879.8	0.986	1.560	1.971
35.8	58.0	60.7	1867	0.839	594.2	1.351	1.726	2.129
47.2	55.1	31.5	1870	0.916	359.6	1.682	1.889	2.285
58.3	52.8	24.3	1872	0.936	315.3	2.082	2.212	2.435
70.1	48.4	16.8	1873	0.955	283.0	2.291	2.378	2.547
80.0	47.0	13.4	1874	0.964	246.5	2.441	2.512	2.682
90.2	44.8	9.27	1874	0.975	196.9	2.651	2.721	2.814
100.2	42.6	6.38	1874	0.983	157.6	2.757	2.801	2.927
120.4	39.6	3.69	1873	0.990	113.5	2.861	2.887	2.940
140.3	36.0	1.82	1870	0.995	74.5	2.864	2.892	2.956
159.1	33.8	1.13	1868	0.997	55.9	2.868	2.903	2.973
180.7	30.8	0.59	1865	0.998	38.6	2.869	2.922	2.989
200.3	29.4	0.39	1861	0.999	29.3	2.870	2.954	3.001

Particle-Life History,  $\phi = 1.0$ ,  $T_f \approx 1952$  K

x (mm)	d <sub>p</sub> ( $\mu$ m)	m <sub>p</sub> (ng)	T <sub>p</sub> (K)	Reacted Mass Fraction	Apparent Density (kg/m <sup>3</sup> )	u <sub>p</sub> (m/s)	u with Particles Present (m/s)	u without Particles Present (m/s)
0.0	52.6	138.7	604	0.000	1820.2	0.381	0.462	1.549
1.8	51.9	117.0	1875	0.156	1598.4	0.607	0.704	1.561
2.6	51.4	103.6	1877	0.253	1457.0	0.661	0.821	1.591
4.4	50.4	89.6	1878	0.354	1336.7	0.760	1.004	1.617
5.7	49.7	79.1	1879	0.430	1230.6	0.822	1.157	1.647
8.1	48.6	65.2	1880	0.530	1084.8	0.915	1.264	1.661
15.7	45.4	45.3	1883	0.673	924.6	1.121	1.759	1.808
23.1	42.7	32.0	1887	0.769	785.0	1.249	1.857	1.963
35.9	38.5	19.2	1891	0.862	642.6	1.372	1.953	2.132
47.1	35.9	11.5	1895	0.917	474.7	1.487	2.055	2.281
58.3	34.1	6.7	1897	0.952	322.7	1.597	2.151	2.435
69.9	31.3	2.87	1898	0.979	178.8	1.721	2.249	2.539
80.4	29.5	1.84	1899	0.987	136.9	1.834	2.320	2.687
90.4	27.4	1.03	1900	0.993	95.6	1.947	2.391	2.818
100.3	25.2	0.57	1899	0.996	68.0	2.060	2.464	2.928
120.1	21.6	0.175	1899	0.999	33.2	2.173	2.538	2.936
140.7	18.1	0.047	1894	1.000	15.1	2.285	2.612	2.961
159.9	15.8	0.0169	1890	1.000	8.2	2.398	2.681	2.977
179.8	13.7	0.0058	1882	1.000	4.3	2.511	2.755	2.981
200.5	12.1	0.0023	1841	1.000	2.5	2.624	2.826	2.998

Particle-Life History,  $\phi = 1.0$ ,  $T_f \approx 1952$  K

x (mm)	d <sub>p</sub> ( $\mu$ m)	m <sub>p</sub> (ng)	T <sub>p</sub> (K)	Reacted Mass Fraction	Apparent Density (kg/m <sup>3</sup> )	u <sub>p</sub> (m/s)	u <sub>∞</sub> with Particles Present (m/s)	u <sub>∞</sub> without Particles Present (m/s)
0.0	26.3	17.3	597	0.000	1816.3	0.486	0.521	1.549
1.8	25.3	11.0	1913	0.364	1297.3	0.949	1.124	1.561
2.6	24.9	9.4	1913	0.457	1162.9	1.044	1.231	1.592
4.4	24.1	8.7	1914	0.497	1187.1	1.208	1.300	1.618
5.7	23.6	8.0	1915	0.538	1162.4	1.293	1.379	1.645
8.2	22.6	6.3	1917	0.636	1042.4	1.408	1.451	1.665
10.4	21.7	5.0	1918	0.711	934.5	1.478	1.526	1.707
15.4	19.8	3.1	1924	0.821	762.7	1.542	1.598	1.803
23.1	17.3	1.5	1926	0.913	553.3	1.698	1.714	1.963
35.8	14.4	0.53	1927	0.969	339.0	1.812	1.836	2.129
47.2	12.6	0.12	1929	0.993	114.6	1.901	1.959	2.282
58.1	11.6	0.034	1931	0.998	41.6	2.013	2.081	2.431
70.4	9.5	0.0089	1932	0.999	19.8	2.145	2.203	2.549
80.0	8.7	0.0042	1934	1.000	12.2	2.267	2.323	2.682
90.4	7.6	0.0017	1935	1.000	7.4	2.390	2.445	2.811
100.1	6.6	0.00072	1936	1.000	4.8	2.512	2.567	2.926
120.1	5.0	0.00031	1938	1.000	4.7	2.634	2.687	2.938
139.5	3.9	0.000092	1937	1.000	3.0	2.756	2.809	2.949
160.1	2.6	0.000024	1930	1.000	2.6	2.881	2.928	2.978
180.4	1.6	0.000004	1911	1.000	1.9	2.887	2.937	2.989
200.1	1.1	0.000001	1872	1.000	1.4	2.889	2.952	3.000



Particle-Life History,  $\phi = 1.0$ ,  $T_f \approx 1952$  K

x (mm)	d <sub>p</sub> ( $\mu$ m)	m <sub>p</sub> (ng)	T <sub>p</sub> (K)	Reacted Mass Fraction	Apparent Density (kg/m <sup>3</sup> )	u <sub>p</sub> (m/s)	u <sub>∞</sub> with Particles Present (m/s)	u <sub>∞</sub> without Particles Present (m/s)
0.0	10.2	1.01	598	0.000	1817.7	0.517	0.834	1.543
1.8	9.3	0.56	1940	0.446	1329.7	1.518	1.534	1.561
2.4	9.0	0.42	1940	0.584	1100.3	1.583	1.586	1.588
4.4	8.4	0.30	1940	0.703	966.7	1.607	1.612	1.618
5.7	7.7	0.11	1941	0.891	460.2	1.642	1.643	1.645
8.2	6.8	0.07	1941	0.931	425.2	1.663	1.664	1.665
10.3	6.2	0.02	1942	0.980	160.3	1.201	1.204	1.705
15.8	4.9	0.007	1943	0.993	113.6	1.804	1.808	1.812
23.2	3.8	0.002	1946	0.998	69.6	1.951	1.961	1.965
36.2	2.6	0.005	1997	1.000	54.3	2.131	2.135	2.138
47.1	1.8	0.000002	1949	1.000	0.7	2.278	2.280	2.283
58.4	1.4	0.000001	1951	1.000	0.7	2.431	2.434	2.437
70.2	1.0	0.0	1950	1.000	0.0	2.542	2.545	2.549
80.0	0.61	0.0	1947	1.000	0.0	2.679	2.680	2.682
90.1	0.41	0.0	1945	1.000	0.0	2.809	2.809	2.819
99.9	0.24	0.0	1942	1.000	0.0	2.879	2.922	2.924
120.1	0.06	0.0	1932	1.000	0.0	2.883	2.936	2.938

Particle-Life History,  $\phi = 1.4$ ,  $T_f \approx 1624$  K

x (mm)	$d_p$ ( $\mu\text{m}$ )	$m_p$ (ng)	$T_p$ (K)	Reacted Mass Fraction	Apparent Density ( $\text{kg}/\text{m}^3$ )	$u_p$ (m/s)	$u_{\infty}$ with Particles Present (m/s)	$u_{\infty}$ without Particles Present (m/s)
0.0	73.4	376.9	592	0.000	1820.3	0.365	0.601	1.527
1.1	72.9	354.2	1613	0.060	1746.1	0.469	0.752	1.551
3.0	72.7	342.7	1627	0.091	1703.4	0.551	0.881	1.576
4.9	72.6	337.9	1627	0.103	1686.5	0.616	0.979	1.598
7.9	72.3	323.7	1627	0.141	1635.8	0.702	1.042	1.627
10.0	72.1	315.6	1627	0.163	1608.2	0.752	1.133	1.647
13.9	71.8	302.5	1627	0.197	1560.8	0.826	1.224	1.727
18.7	71.5	289.9	1628	0.231	1514.7	0.900	1.314	1.815
25.2	71.1	269.6	1629	0.285	1432.6	0.978	1.405	1.901
31.1	70.7	259.1	1626	0.313	1400.3	1.034	1.496	1.988
40.7	70.3	244.4	1627	0.352	1343.5	1.105	1.566	2.071
51.1	69.7	224.8	1627	0.404	1267.9	1.160	1.631	2.110
62.2	69.2	208.7	1628	0.446	1202.8	1.206	1.702	2.156
68.5	68.9	199.6	1630	0.470	1165.5	1.227	1.774	2.203
75.2	68.6	191.8	1631	0.491	1134.7	1.245	1.845	2.243
87.4	68.0	176.7	1632	0.531	1073.3	1.262	1.912	2.319
100.1	67.3	158.9	1634	0.578	995.6	1.281	1.984	2.385
121.2	66.3	137.4	1636	0.635	900.4	1.293	2.054	2.457
140.3	65.2	115.4	1637	0.694	795.2	1.299	2.123	2.538
179.7	63.1	83.7	1630	0.778	636.3	1.310	2.198	2.618
200.4	62.0	69.9	1627	0.815	560.1	1.315	2.263	2.691

A.3 Agglomerates of Monodisperse Particles,  $d_u = 150 \text{ nm}$

Particle-Life History,  $\phi = 0.6$ ,  $T_f = 1663 \text{ K}$

$x$ (mm)	$d_p$ ( $\mu\text{m}$ )	$m_p$ (ng)	$T_p$ (K)	$u_p$ (m/s)	$t$ (s)
0.0	73.5	385.4	602	0.439	0.0
2.0	71.9	325.5	2016	0.581	0.0038
3.1	69.0	240.7	2059	0.623	0.0057
4.4	65.8	168.8	2063	0.683	0.0077
7.3	61.1	120.5	2081	0.712	0.0119
10.2	56.6	74.6	2087	0.724	0.0158
13.1	51.1	43.2	2096	0.746	0.0198
16.3	46.1	26.6	2103	0.773	0.024
18.6	41.8	10.8	2114	0.792	0.027
22.5	35.5	6.4	2120	0.809	0.032
25.9	29.7	3.7	2142	0.851	0.036
27.7	25.9	1.9	2147	0.872	0.038
29.4	22.3	1.1	2138	0.885	0.040
32.1	17.1	0.3	2140	0.892	0.043
33.9	12.3	0.006	2136	0.899	0.045
35.7	7.9	0.0	2109	0.942	0.047
37.6	3.1	0.0	2062	0.984	0.049

Particle-Life History,  $\phi = 0.6$ ,  $T_f = 1953 \text{ K}$

$x$ (mm)	$d_p$ ( $\mu\text{m}$ )	$m_p$ (ng)	$T_p$ (K)	$u_p$ (m/s)	$t$ (s)
0.0	73.4	383.5	604	0.259	0.0
1.5	68.9	238.4	2205	0.565	0.0036
2.4	65.1	155.1	2221	0.679	0.0050
3.3	61.5	102.0	2234	0.802	0.0062
4.0	59.4	78.8	2241	0.885	0.0069
5.3	55.3	54.6	2257	0.942	0.0083
7.3	49.3	30.4	2271	1.051	0.0103
9.5	44.0	18.8	2284	1.079	0.0124
11.7	38.1	9.8	2287	1.114	0.0144
12.6	33.7	5.4	2288	1.159	0.0152
14.1	27.9	3.1	2289	1.194	0.0165
15.8	23.2	1.2	2288	1.243	0.0179
17.7	17.8	0.4	2289	1.287	0.0194
20.5	10.4	0.003	2287	1.310	0.0215
21.4	5.5	0.0	2285	1.337	0.0223
32.7	2.1	0.0	2280	1.354	0.0232

Particle-Life History,  $\phi = 1$ ,  $T_f = 1683$  K

x (mm)	d <sub>p</sub> ( $\mu$ m)	m <sub>p</sub> (ng)	T <sub>p</sub> (K)	u <sub>p</sub> (m/s)	t (s)
0.0	73.5	389.2	605	0.438	0.0
1.9	73.4	388.3	1517	0.584	0.0040
2.8	73.4	385.7	1604	0.616	0.0051
4.3	73.2	378.3	1645	0.661	0.0075
5.9	73.0	369.8	1652	0.714	0.0098
8.0	72.7	359.8	1654	0.767	0.013
15.2	71.9	330.6	1654	0.913	0.021
21.5	71.3	309.8	1655	1.009	0.027
30.4	70.5	285.3	1655	1.113	0.036
41.5	69.6	259.7	1656	1.210	0.046
52.2	68.9	238.6	1657	1.281	0.054
63.5	68.1	219.2	1657	1.338	0.063
75.4	67.3	201.1	1658	1.385	0.071
89.3	66.6	186.8	1657	1.396	0.081
107.5	65.3	168.9	1660	1.407	0.094
130.1	63.9	154.7	1661	1.422	0.110
146.2	62.8	144.1	1659	1.485	0.121
165.8	61.9	133.8	1658	1.523	0.134
182.7	60.7	130.7	1655	1.548	0.145
202.4	59.8	119.8	1640	1.550	0.158

A.4 Agglomerates of Monodisperse Particles  $d_u = 70 \text{ nm}$

Particle-Life History,  $\phi = 0.6$ ,  $T_f = 1663 \text{ K}$

$x$ (mm)	$d_p$ ( $\mu\text{m}$ )	$m_p$ (ng)	$T_p$ (K)	$u_p$ (m/s)	$t$ (s)
0.0	73.5	397.7	607	0.435	0.0
2.0	71.7	331.7	1998	0.581	0.0038
3.2	68.6	235.8	2033	0.628	0.0058
4.4	65.4	166.1	2044	0.687	0.0077
7.6	59.2	102.0	2057	0.721	0.012
10.5	54.5	60.3	2069	0.732	0.016
12.8	49.2	29.7	2084	0.763	0.019
16.7	43.4	13.9	2092	0.789	0.024
19.1	39.4	8.4	2101	0.802	0.027
23.2	32.6	5.6	2109	0.837	0.032
26.7	36.7	2.5	2118	0.871	0.036
30.2	19.1	0.7	2138	0.888	0.040
33.9	12.3	0.006	2126	0.912	0.044
37.6	6.9	0.0	2098	0.997	0.048
39.7	2.4	0.0	2079	1.073	0.050

Particle-Life History,  $\phi = 0.6$ ,  $T_f = 1953$  K

x (mm)	d <sub>p</sub> ( $\mu$ m)	m <sub>p</sub> (ng)	T <sub>p</sub> (K)	u <sub>p</sub> (m/s)	t (s)
0.0	73.5	404.3	610	0.256	0.0
1.5	68.7	246.8	2174	0.565	0.0037
2.4	64.6	155.4	2191	0.686	0.0050
3.0	62.5	121.4	2198	0.757	0.0057
4.1	59.5	75.5	2211	0.772	0.0071
5.2	55.6	51.9	2223	0.789	0.0085
6.2	49.7	31.3	2229	0.801	0.0098
7.3	48.1	23.6	2236	0.854	0.0115
8.5	41.5	9.43	2242	0.982	0.0128
10.1	35.2	4.42	2257	0.931	0.0145
11.3	30.8	3.14	2259	0.967	0.0158
12.4	26.6	2.47	2261	1.012	0.0170
14.3	19.6	0.52	2262	1.087	0.0187
16.7	1.03	0.004	2262	1.124	0.0209
18.0	5.7	0.0	2260	1.177	0.0221
19.6	1.8	0.0	2158	1.207	0.0234

Particle-Life History,  $\phi = 1.0$ ,  $T_f = 1683 \text{ K}$

$x$ (mm)	$d_p$ ( $\mu\text{m}$ )	$m_p$ (ng)	$T_p$ (K)	$u_p$ (m/s)	$t$ (s)
0.0	73.4	402.1	609	0.441	0.0
1.9	73.4	401.0	1516	0.583	0.0037
2.8	73.3	397.4	1605	0.617	0.0052
4.2	73.2	388.9	1640	0.664	0.0074
6.1	72.9	377.0	1647	0.720	0.0101
8.2	72.5	364.5	1648	0.775	0.0129
15.8	71.6	328.8	1648	0.929	0.0218
21.3	70.9	307.5	1650	1.015	0.0275
30.5	69.8	278.1	1650	1.126	0.0360
41.8	68.9	248.3	1650	1.228	0.0456
53.0	68.0	223.8	1651	1.302	0.0544
64.2	67.1	202.4	1651	1.361	0.0628
68.9	66.7	194.2	1652	1.382	0.0662
79.8	65.2	184.9	1654	1.393	0.0741
91.9	63.9	168.8	1655	1.402	0.0827
105.5	63.1	160.6	1654	1.427	0.0924
122.5	61.6	140.7	1651	1.473	0.104
158.0	60.3	130.4	1650	1.493	0.128
171.5	57.4	107.6	1647	1.510	0.137
192.8	56.1	92.5	1641	1.539	0.151
215.2	55.8	81.3	1632	1.547	0.168



**A.5 Agglomerates of a Particle Blend,  $d_u = 70$  and  $300$  nm (50% each by mass)**

**Particle-Life History,  $\phi = 0.6$ ,  $T_f = 1663$  K**

$x$ (mm)	$d_p$ ( $\mu\text{m}$ )	$T_p$ (K)	$u_p$ (m/s)	$m_p$ (ng)	$t$ (s)
0.0	73.5	602	0.439	438.0	0.0
2.0	72.7	1914	0.569	402.3	0.004
3.9	69.3	2139	0.623	281.9	0.007
7.2	63.3	2161	0.749	142.2	0.012
10.0	58.9	2173	0.881	82.8	0.015
12.2	55.7	2181	0.966	54.7	0.018
19.1	49.0	2183	0.992	33.7	0.025
24.1	43.6	2180	1.017	11.2	0.030
28.2	38.8	2177	1.032	5.2	0.034
33.4	31.6	2172	1.054	3.1	0.039
38.7	24.1	2179	1.079	1.9	0.044
43.2	17.2	2178	1.093	0.4	0.048
47.5	10.8	2182	1.102	0.0	0.052
53.4	1.9	2176	1.274	0.0	0.057

Particle-Life History,  $\phi = 0.6$ ,  $T_f = 1953 \text{ K}$

$x$ (mm)	$d_p$ ( $\mu\text{m}$ )	$T_p$ (K)	$u_p$ (m/s)	$m_p$ (ng)	$t$ (s)
0.0	73.5	605	0.438	438.6	0.0
2.0	71.1	2260	0.674	341.6	0.004
4.0	65.4	2308	0.820	183.0	0.006
7.1	57.8	2332	1.076	72.7	0.010
10.1	51.6	2351	1.126	31.0	0.012
12.3	47.5	2329	1.247	13.3	0.015
16.2	40.1	2332	1.322	7.2	0.018
18.8	31.2	2325	1.361	3.1	0.020
24.3	22.3	2321	1.387	1.8	0.024
27.0	12.9	2319	1.403	0.6	0.026
31.4	2.1	2320	1.441	0.0	0.029

Particle-Life History,  $\phi = 1.0$ ,  $T_f = 1683$  K

x (mm)	d <sub>p</sub> ( $\mu$ m)	m <sub>p</sub> (ng)	T <sub>p</sub> (K)	u <sub>p</sub> (m/s)	t (s)
0.0	73.3	434.7	609	0.442	0.0
1.8	73.3	434.5	1441	0.565	0.0035
2.9	73.3	433.3	1584	0.604	0.0053
4.2	73.2	430.3	1643	0.641	0.0074
6.3	73.1	424.2	1664	0.695	0.0106
7.9	73.0	419.5	1667	0.731	0.0129
15.5	72.5	400.5	1668	0.863	0.022
22.6	72.1	385.4	1668	0.954	0.030
31.9	71.7	368.3	1667	1.045	0.039
41.4	71.3	352.9	1668	1.117	0.048
52.7	70.8	336.5	1668	1.181	0.058
63.2	70.4	322.4	1668	1.229	0.067
73.0	70.0	310.5	1669	1.265	0.075
91.4	69.4	289.7	1668	1.317	0.089
104.2	69.0	276.6	1669	1.345	0.098
139.9	66.6	252.1	1668	1.402	0.124
158.2	65.7	233.9	1661	1.409	0.137
169.4	63.5	213.0	1657	1.419	0.145
187.8	62.7	201.7	1649	1.431	0.158
207.6	60.8	182.6	1633	1.454	0.173

### References

1. G. W. Burdette, H. R. Lander and J. R. McCoy, "High Energy Density Fuels for Cruise Missiles," AIAA Paper No. 78-267 (1978).
2. T. W. Bruce, H. C. Mongia, R. S. Stearns, L. W. Hall and G. M. Faeth, "Formulation Properties and Combustion of Carbon-Slurry Fuels," Proceedings of Sixteenth JANNAF Combustion Meeting, CPIA Publication No. 308, pp. 679-717, December 1979.
3. T. W. Bruce and H. Mongia, "Compound Cycle Turbofan Engine Task IX: Carbon-Slurry Fuel Combustion Evaluation Program," Technical Report AFWAL-TR-80-2035, March 1980.
4. G. A. Szekely, Jr. and G. M. Faeth, "An Investigation of Slurry Fuel Combustion," Final Report to AiResearch Manufacturing Company of Arizona, Department of Mechanical Engineering, The Pennsylvania State University, November 1979.
5. R. H. Salvesen, "Carbon Slurry Fuels for Volume Limited Missiles," Technical Report AFAPL-TR-79-2122, November 1979.
6. G. A. Szekely and G. M. Faeth, "An Investigation of Slurry Fuel Combustion," Technical Report AFWAL-TR-80-2125, January 1981.
7. G. A. Szekely, Jr. and G. M. Faeth, "Combustion Properties of Carbon Slurry Drops," AIAA J., Vol. 20, pp. 422-429, 1982.
8. G. A. Szekely, Jr. and G. M. Faeth, "Effects of Envelope Flames on Drop Gasification Rates in Turbulent Diffusion Flames," Combustion and Flame, in press.
9. G. A. Szekely, Jr. and G. M. Faeth, "Reaction of Carbon Black Slurry Agglomerates in Combustion Gases," Nineteenth Symposium (International) on Combustion, The Combustion Institute, Pittsburgh, in press.
10. G. A. Szekely, Jr., "Experimental Evaluation of a Carbon Slurry Droplet Combustion Model," Ph.D. Thesis, The Pennsylvania State University, University Park, PA, 1982.
11. M. Lavid and L. A. Ruth, "The Combustion of Carbon Slurry Fuel--Experimental Results," Paper No. 6, Fall Technical Meeting--Eastern Section of the Combustion Institute, Princeton, NJ, October 1980.
12. C. K. Law, H. K. Law and C. H. Lee, "Combustion Characteristics of Droplets of Coal/Oil and Coal/Oil/Water Mixtures," Energy, Vol 37, pp. 329-339, 1980.
13. K. Miyasaka and C. K. Law, "Combustion and Agglomeration of Coal-Oil Mixtures in Furnace Environments," Comb. Sci. and Tech., Vol. 24, pp. 71-82, 1980.

# REFERENCES (Concluded)

14. A. J. Shearer, H. Tamura and G. M. Faeth, "Evaluation of a Locally Homogeneous Flow Model of Spray Evaporation," J. of Energy, Vol. 3, pp. 271-278, Sept.-Oct. 1979.
15. C-P. Mao, G. A. Szekely, Jr. and G. M. Faeth, "Evaluation of a Locally Homogeneous Flow Model of Spray Combustion," J. of Energy, Vol. 4, No. 2 pp. 78-87, 1980.
16. C-P. Mao, Y. Wakamatsu and G. M. Faeth, "A Simplified Model of High Pressure Spray Combustion," Eighteenth Symposium (International) on Combustion, The Combustion Institute, Pittsburgh, PA, pp. 337-347, 1981.
17. P. A. Libby and T. R. Blake, "Burning Carbon Particles in the Presence of Water Vapor," Combustion and Flame, Vol. 41, pp. 123-147, 1981.
18. K. G. Neoh, J. B. Howard and A. F. Sarofim, "Soot Oxidation in Flames," Particulate Carbon Formation During Combustion, D. C. Siegla and G. W. Smith, ed., Plenum Press, New York, pp. 261-282, 1981.
19. M. Glass and I. M. Kennedy, "An Improved Seeding Method for High Temperature Laser-Doppler Velocimetry," Combustion and Flame, Vol. 29, pp. 333-335, 1977.
20. W. E. Kaskan, "The Dependence of Flame Temperature on Mass Burning Velocity," Sixth Symposium (International) on Combustion, Williams and Wilkins, New Haven, pp. 134-143, 1956.
21. S. Gordon and B. J. McBride, Computer Program for Calculation of Complex Chemical Equilibrium Compositions, Rocket Performance, Incident and Reflected Shocks, and Chapman-Jouget Detonations, NASA SP-273, 1971.
22. J. J. Sangiovanni and A. S. Kesten, "Effect of Droplet Interaction on Ignition in Monodisperse Droplet Streams," Sixteenth Symposium (International) on Combustion, The Combustion Institute, Pittsburgh, PA, pp. 577-592, 1977.
23. G. M. Faeth, "Current Status of Droplet and Liquid Combustion," Prog. Energy Combust. Sci., Vol. 3, No. 4, pp. 191-224, 1977.
24. J. Nagle and R. F. Strickland-Constable, "Oxidation of Carbon Between 1000-2000°C," Proc. Fifth Carbon Conf., Vol. 1, pp. 154-164, 1962.
25. C. Park and J. P. Appleton, "Shock-Tube Measurements of Soot Oxidation Rates," Combustion and Flame, Vol. 20, No. 3, pp. 369-379, 1973.
26. J. F. Johnstone, C. Y. Chen and D. S. Scott, "Kinetics of the Steam-Carbon Reaction in Porous Graphite Tubes," Ind. Engr. Chem., Vol. 44, No. 7, pp. 1564-1569, 1952.